Exploiting the potential of 3D borehole seismic data for high-resolution imaging and velocity estimation, a full wavefield approach

El Marhfoul, B.

DOI
10.4233/uuid:70db51fd-8a61-4074-8c84-3520854e51f8

Publication date
2023

Document Version
Final published version

Citation (APA)
El Marhfoul, B. (2023). *Exploiting the potential of 3D borehole seismic data for high-resolution imaging and velocity estimation, a full wavefield approach*. [Dissertation (TU Delft), Delft University of Technology]. https://doi.org/10.4233/uuid:70db51fd-8a61-4074-8c84-3520854e51f8

Important note
To cite this publication, please use the final published version (if applicable).
Please check the document version above.

Exploiting the potential of 3D borehole seismic data for high-resolution imaging and velocity estimation, a full wavefield approach

PROEFSCHRIFT

ter verkrijging van de graad van doctor
aan de Technische Universiteit Delft,
op gezag van de Rector Magnificus prof.dr.ir. T.H.J.J. van der Hagen,
voorzitter van het College voor Promoties,
in het openbaar te verdedigen
op maandag 22 mei 2023 om 17:30 uur

door

Bouchaib EL MARHFOUL

Ingenieur in de Technische Natuurkunde,
Technische Universiteit Delft, Nederland
geboren te Casablanca, Marokko

Dit proefschrift is goedgekeurd door de promotoren.

Samenstelling promotiecommissie:

Rector Magnificus,	voorzitter
Dr.ir. D.J. Verschuur,	Technische Universiteit Delft, promotor
Prof.dr.ir. E.C. Slob,	Technische Universiteit Delft, promotor

Onafhankelijke leden:

Prof.dr.ir. C.P.A. Wapenaar,	Technische Universiteit Delft
Prof.dr. G. Bertotti,	Technische Universiteit Delft
Prof.dr. G.T. Schuster,	The University of Utah
Dr. P.M. Zwartjes,	Aramco Overseas B.V. Delft
Dr. J. Owusu,	Independent consultant

ISBN 978-94-6384-447-5

SUPPORT
The research for this thesis was financially supported by the DELPHI consortium.

Typesetting system: LaTeX.

Printed in The Netherlands by Gildeprint.

Contents

Summary

Geophysics is a branch of physics that is mainly concerned about understanding and describing the physical behaviour and activities of the earth's geological system. Usually, seismic data is acquired at the surface and the corresponding signals go through a sequence of preprocessing steps to filter out the noise and enhance the quality of the measurements. These measurements are then transformed into a so-called reflectivity image (snapshot in time) of the subsurface via the deployment of the so called migration algorithms. Extensive studies and great effort is usually made to determine a suitable acquisition geometry design for optimal illumination of every imaging grid point in the subsurface in the studied area. However, within the geoenergy industry it has always been an undisputed believe that improved and better results can be obtained only if more data is acquired with denser sampling at both the source's and receiver's side. This "linear" way of thinking is also consistent with the conceptual assumptions of most current migration algorithms.

The challenge is of course to achieve the same, or maybe even better, results with less data. This is in accordance with the currently ongoing energy transition, which is forcing the geophysical scientific community to shift their focus from the acquisition and processing of large and expensive surface seismic surveys toward optimized management, in terms of data acquisition, processing and production, of the existing hydrocarbon-based reservoirs. Especially datasets with sparse acquisition geometry like 3D Ocean Bottom Node (OBN) and 3D Borehole Seismic Data (BSD) surveys, where we have measurements at a limited number of sensors along the ocean bottom or in the borehole but usually with dense sources sampling at the surface, can greatly benefit from such a development.

3D borehole geophysics, which is the main subject of this thesis, has for a long time been an underdeveloped and, therefore, an unappreciated component within most geophysical organisations. This is mainly because accurate results are usually obtained only in the immediate vicinity of the borehole and

their quality decays rapidly in the lateral extent. However, and especially in the marine case, 3D BSD surveys are rich in higher-order scatterings that can have significant added value when combined with unconventional and non-linear inversion-imaging algorithms like Full Wavefield Migration (FWM) and Joint Migration Inversion (JMI). Furthermore, in combination with modern measurements techniques (like Distributed Acoustic Sensing (DAS) technology), continuous and permanent monitoring of existing and new reservoirs – whether hydrocarbon-based or geothermal – can easily be realised.

In this thesis the recently developed inversion-imaging algorithms FWM and JMI are extended to the 3D case and further engineered to properly handle the special acquisition geometry of 3D BSD surveys and exploit the full potential of the total wavefield available in 3D borehole seismic data. First, a more complete and comprehensive derivation of the involved gradients, for the reflectivity image and velocity model update, is presented. This makes the combination of one-way tomography of the direct wavefield with reflection tomography of the other energy modes (primary reflections, higher-order scatterings of the up- and down-going wavefield) a straightforward process. Then, an effective strategy of the application of the 3D JMI algorithm to 3D BSD is developed and, with the presented examples, it will be demonstrated that, for instance, the standard and conventional separation of the up- and down-going wavefield of 3D BSD becomes an obsolete process. Along the same lines, we will show that integration of surface seismic data and 3D BSD, or even multi 3D BSD surveys, in one inversion process produces more accurate and geologically consistent solutions. Next, the capability of the 3D FWM algorithm together with 3D BSD surveys for solid reservoir monitoring will be demonstrated. After that the challenges of the current acoustic implementation of the FWM JMI algorithms will be discussed, especially the effect of the mode converted waves on the velocity model gradient. Finally, some suggestions are made for further enhancement of the JMI algorithm, particularly at the side of the migration velocities update. This can be achieved by the combination of complementary and effective objective-functions, which makes the JMI algorithm more robust especially in the case of geological environment with high velocity contrast.

Samenvatting

Geofysica is een tak van de natuurkunde die zich voornamelijk bezighoudt met het begrijpen en beschrijven van het fysische gedrag en de activiteiten van het geologische systeem van de aarde. Meestal wordt seismische data aan de oppervlakte verzameld en de bijbehorende signalen gaan door een reeks van preprocessing stappen om de ruis te filteren en de kwaliteit van de metingen te verbeteren. Deze metingen worden vervolgens omgezet in een reflectiviteitsbeeld (momentopname) van de ondergrond via de inzet van de zogenaamde migratie-algoritmes. Uitgebreide analyses worden meestal gedaan om een geschikte acquisitiegeometrieontwerp te bepalen voor optimale belichting van elke beeldrasterpunt in de ondergrond van het betrokken gebied. Binnen de geo-energie-industrie is het echter altijd een onbetwiste overtuiging geweest dat verbeterde resultaten alleen kunnen worden verkregen als er meer data wordt geschoten met een dichtere bemonstering aan zowel de bron- als de ontvangerzijde. Deze "lineaire" manier van denken komt ook overeen met de conceptuele aannames van de meeste huidige migratie-algoritmes.

De uitdaging is natuurlijk om met minder data dezelfde, of misschien zelfs betere, resultaten te behalen. Dit past goed binnen de gedachtegang van de momenteel aan de gang zijnde energietransitie, die de geofysische wetenschappelijke gemeenschap dwingt on hun focus te verleggen van de verwerving en verwerking van grote en dure seismische oppervlakte-onderzoeken naar geoptimaliseerd beheer, in termen van data-acquisitie, verwerking en productie, van de bestaande op koolwaterstoffen gebaseerde reservoirs. Vooral datasets met sparse acquisitiegeometrie zoals 3D Ocean Bottom Node (OBN) en 3D Borehole Seismic Data (BSD), waarbij we meting hebben op een beperkt aantal sensoren langs de zeebodem of in de boorput maar meestal met toch dichte bronnen bemonstering aan de oppervalk, zullen baat hebben bij een dergelijke ontwikkeling.

3D boorput geofysica, het onderwerp van dit proefschrift, is lange tijd een onderontwikkeld en daarom ook niet gewaardeerd onderdeel geweest binnen de meeste geofysische organisaties. Dit komt vooral door het feit dat tot

nu toe nauwkeurige resultaten worden behaald alleen in de directe nabijheid van de boorput en de kwaliteit snel achteruitgaat in de laterale richting. Echter, en vooral in het maritieme geval, is 3D BSD rijk aan verstrooiingen van hoger orde die een significante toegevoegde waarde kunnen hebben mits onconventionele en niet-lineair algoritmes voor inversiebeeldvorming, zoals Full Wavefield Migration (FWM) en Joint Migration Inversion (JMI) worden gebruikt. Bovendien kan, in combinatie met moderne meettechnieken (zoals Distributed Acoustic Sensing (DAS)-technologie), een continue en permanente monitoring van bestaande en nieuwe reservoirs - op basis van koolwaterstoffen of geothermie - eenvoudig worden gerealiseerd.

In dit proefschrift worden de recent ontwikkelde inversiebeeldvorming algoritmes FWM en JMI uitgebreid naar de 3D-case en verder ontwikkeld om de speciale acquisitie geometrie van 3D BSD goed aan te kunnen en het volledige potentieel van het totale golfveld dat beschikbaar is in 3D boorput seismische data te benutten. Eerst wordt een meer complete en uitgebreide afleiding van de betrokken gradiënten voor de update van het reflectiviteitsbeeld en het snelheidsmodel gepresenteerd. Dit maakt de combinatie van eenrichtingstomografie van het directe golfveld met reflectietomografie van de andere energiemodi (primaire reflecties, verstrooiing van hogere orde van het op- en neergaande golfveld) een eenvoudig proces. Vervolgens wordt een effectieve strategie voor de toepassing van het 3D JMI-algoritme op 3D BSD ontwikkeld en met de gepresenteerde voorbeelden zal worden aangetoond dat bijvoorbeeld de standaard en conventionele scheiding van het op- en neergaande golfveld van 3D BSD wordt een achterhaald proces. Langs dezelfde lijnen zullen we laten zien dat de integratie van seismische oppervlaktegegevens en 3D BSD, of zelfs meerdere 3D BSD sets, in één inversieproces veel meer nauwkeurigere en geologisch consistente oplossingen oplevert. Vervolgens zal worden gedemonstreerd hoe het 3D FWM-algoritme samen met 3D BSD kan worden ingezet als een solide instrument voor het monitoren van reservoirs. Daarna zullen de uitdagingen van de huidige akoestische implementatie van de FWM JMI-algoritmes worden besproken, met name het effect van de modus-geconverteerde golven op de snelheidsmodelgradiënt. Ten slotte worden enkele suggesties gedaan voor verdere verbetering van het JMI-algoritme, met name aan de kant van de update van de migratiesnelheden. Dit kan worden bereikt door de combinatie van complementaire en effectieve doelfuncties, waardoor het JMI-algoritme robuuster wordt, vooral in het geval van een geologische omgeving met een hoog snelheidscontrast.

1 Introduction

The history of scientific progress shows that big steps forward are achieved only when existing scientific concepts are drastically changed. Take for example the paradigm shift from the concepts of classical to quantum mechanics where we encounter phenomena that are beyond our wildest imagination. Usually, scientist invent theories based on observations and models with predefined assumptions in order to explain and understand the behaviour of physical systems around us. Those theories, and consequently their outcomes, are just as good and accurate as the adopted assumptions. Therefore, abandoning model assumptions and relying more on physical observations should lead to new insights and advanced scientific concepts that can be beneficial for society and mankind.

Geophysics is a branch of science that is concerned about understanding and describing the physical behaviour and activities of the earth's geological system. Within the geo-energy industry, it is utilized to explore and produce fields of natural resources to answer the world's energy demand. Since the invention of the steam machine, all industries worldwide have been depending on fossil fuels to provide them with the required energy for their production processes. However, the currently ongoing energy transition is forcing the business-decisions makers and consequently the geophysical scientific community to shift their focus from the acquisition and processing of large and

expensive surface seismic surveys toward optimized management, in terms of data acquisition, processing and production, of the existing hydrocarbon-based reservoirs. In addition, the injection of the industrial produced CO_2 into the deep geological formation and the H_2 subsurface storage are relatively new industrial solutions that require steering and guiding to ensure their safety and sustainability. It is envisioned that continuous monitoring of producing reservoirs – whether hydrocarbon-based fuel or even geothermal – and also of storage basins will be a standard practice in the future. Figure 1.1 shows an illustration of how this concept can be realized, especially with the permanent placement of a measurements-cable, for a example a Distributed Acoustic Sensing (DAS) cable, in the borehole and active sources at the surface. The challenge that is imposing itself is to maximize the reliability and accuracy of the description of the earth's geological system given the limited and reduced amount of the acquired seismic data. This may sound contradictory to what we are used to, nevertheless it can be achieved by better understanding of the physical characteristics and content of the measured signals combined with the deployment of unconventional inversion-imaging algorithms.

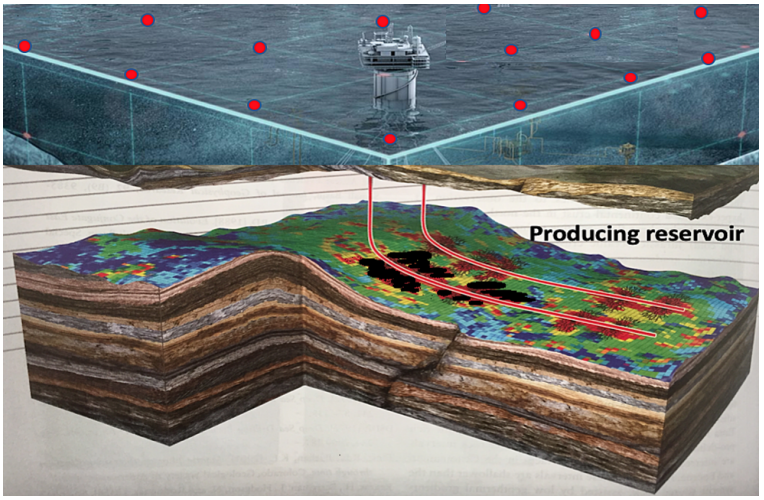

Figure 1.1: Continuous monitoring of a producing reservoir by the deployment of measurements-cable in the borehole, like a DAS cable, and active sources at the surface as indicated by the red dots. Note that this will not cause any production disruption.

In this chapter we will first present a brief introduction of seismic imaging

in general and borehole seismic technology in particular with its current role within the geophysical community, then a comparison between linear (conventional) and nonlinear (unconventional) imaging algorithms will be discussed with the main focus on the case of borehole seismic data. Note that extensive examples will be showed and discussed in more details in the next chapters. Finally, the objectives and an outline of the content of this thesis will be stated and discussed.

1.1 The seismic method

1.1.1 The sound of the underground

Within the scientific community, the process of transforming measured signals along a certain surface into a snapshot of the state of a certain physical system at a particular moment in time is called imaging. In particular, seismic imaging (Claerbout, 1985; Stolt and Weglein, 1985), also known as migration, is concerned about mapping the structure of the subsurface by utilizing sound waves that are emitted into the subsurface and get scattered by contrasts in acoustic impedance toward the registration surface, or the

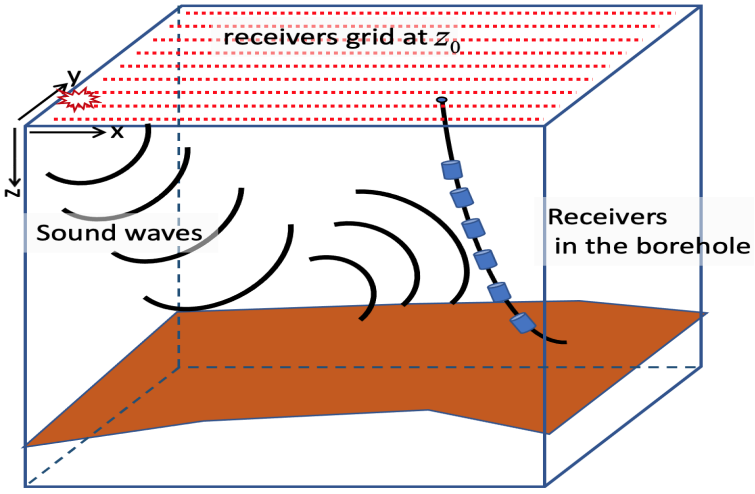

Figure 1.2: Schematic illustration of sound waves emitted into the subsurface by an active source (red star) and reflected back to the recording sensors at the surface or in the borehole. Note that in passive seismic we can disregard the active sources and register the seismic responses of the so-called passive sources in the subsurface.

recording tool in the case of borehole seismic, to be recorded by arrays of sensors called receivers. Figure 1.2 shows a schematic illustration of this concept. In a similar way echo scans in medical imaging or sonar scans in marine applications are obtained based on the interaction of sound waves with the studied objects. Note that it is also possible to image the subsurface by registering the seismic response of the so-called passive sources in the subsurface without the deployment of active sources (Pavlis, 2003; Wason et al., 2004; Berkhout and Verschuur, 2011).

Since its introduction, the seismic method had applications mainly oriented toward the exploration, production and development of hydrocarbon-based reservoirs. However, nowadays the seismic method is utilized even beyond the oil and gas industry like the exploration and production of geothermal-energy basins, where accurate characterization of the subsurface geophysical properties and the delineation of complex fault systems play an essential role (Gao et al., 2021). In addition, seismic data could also be utilized for the determination of the elasticity modulus and stiffness of the shallow near surface for the purpose of the installation of wind turbines. Recently, there have been even developments to integrate wind turbines in the seismic method and use them as non-destructive seismic sources for permanent monitoring of the subsurface (Ruigrok et al., 2020).

The above-mentioned applications and other non-industrial practices indicate the crucial contribution of seismic imaging to produce reliable estimates of the reflectivity image, together with the corresponding medium parameters, for better understanding and continuous monitoring of the subsurface. Preferably, this should be achieved by minimum investments in terms of data acquirement and preprocessing, which requires more advanced and integrated inversion-imaging algorithms.

1.1.2 Borehole seismic technology

Borehole-related seismic data, with its broader frequency-bandwidth and relatively enhanced signal to noise ratio compared to surface seismic data, can have significant added value at the stage of reservoir development and can provide us with high-resolution images (Hardage, 1985; House et al., 2008) in the area around the borehole. This is mainly due to the position of the receivers close to the reservoir yielding a shorter travel path, and hence, less amplitude loss, especially at the high-frequencies range (Li et al., 2015). The latter is amplified by the fact that in an onshore situation the unconsolidated near surface is traversed only once. Therefore, borehole seismic data-

acquisition design is certainly an innovative technology that keeps evolving and getting more practical especially when combined with modern measurement's techniques like DAS technology (Martuganova et al., 2021). The latter will enable us to acquire borehole seismic data without causing any production disruption, which has always been considered as an undesired incidental.

There are various acquisition geometry designs for borehole-related seismic data. In principle, depending on the intended objectives and the well trajectory the right acquisition geometry configuration can be designed (Oristaglio, 1985). Nevertheless, within the geophysical community, borehole-related seismic data is always referred to as Vertical Seismic Profiling (VSP), which suggests that the receivers are placed in a vertical borehole. However, in reality we encounter all kinds of geometries like deviated wells or even horizontal ones. Therefore, especially for the 3D case, we propose to use a more appropriate and general name like 3D Borehole Seismic Data (BSD) surveys in stead of 3D VSP. The most common and well-known borehole acquisition geometries within the geophysical community can be summarized as follows:

- Zero-offset VSP is an acquisition design where only one active source is deployed at the surface, as close as possible to the well location, and a tool of detectors is placed in the borehole. This data set is usually utilized among other to define accurate time-to-depth conversions for surface seismic images, determine primary reflectors, identify internal multiples generators and also accurately analyzing seismic attenuation (Tak et al., 2013; Matsushima et al., 2015).

- Walk-above VSP is similar to zero-offset VSP but with a deviated well trajectory, which means that for every receiver in the borehole an active source is deployed that has the same lateral location as the receiver (Shafiq and Apisampinvong, 2013). With this design the assumption of the source and being vertically aligned with the receivers is fulfilled, which results in accurate and high-resolution results.

- Walk-around VSP is another acquisition design where a number of active sources is placed in a circular configuration around the well and a tool of detectors is placed in the borehole. This particular acquisition geometry is usually utilized among other for azimuthal anisotropy analysis for better understanding of the fracture orientation around the borehole (Al Dulaijan et al., 2012).

- Walk-away VSP is similar to 2D surface seismic, however in this case the receivers are located in the borehole and an array of active sources is placed along a 2D line at the surface with quite a lateral extent to both sides of the well. This acquisition geometry is usually used for high-resolution imaging purposes and the delineation of complex structures in the area close to the borehole (Smidt et al., 1998; Soni and Verschuur, 2014).
- 3D BSD, which is the main subject of this thesis, has active sources evenly distributed at the surface, whether along an $2D$ areal regular grid or according to a spiral configuration, which is a common practice for the marine situation (House et al., 2008; Al Bannagi et al., 2018).

1.2 Linear seismic imaging methods

Conventionally, seismic imaging can be seen as an open-loop process where measurements, together with a propagation velocity model, are input into an imaging algorithm to produce a reflectivity image of the subsurface as a one-step process. The resolution and the reliability of the seismic image depends on the quality of the measurements and the applied imaging algorithm. In general, most imaging algorithms are based on the assumption that the measured seismic response is only a linear function of the subsurface reflectivity, meaning that it contains primary reflections only. Therefore, the seismic data is always preprocessed accordingly in order to suppress all higher-order scatterings (multiple reflections) to fulfil this linearity assumption.

1.2.1 Higher-order scatterings suppression

The higher-order scatterings can be divided into two major categories namely; surface-related multiples and internal multiples. Over the past decades, several algorithms have been developed to estimate the higher-order scatterings in the seismic data. For example for the surface-related multiples estimation we have the convolution based algorithms like Surface-Related Multiple Elimination (SRME) (Verschuur, 1991; Verschuur et al., 1992; Berkhout and Verschuur, 1997) and algorithms based on the inverse scattering series method (Weglein et al., 1997). For the internal multiples, we see also similar algorithms like Internal Multiples Elimination (IME) (Berkhout and Verschuur, 1999; Verschuur and Berkhout, 2000; Alai and Verschuur, 2006) and attenuation of internal multiples via inverse scattering series (Araujo et al., 1994). However, the bottleneck of these approaches is the adaptive subtrac-

tion that in some cases harms the primary reflections as well. Furthermore, inversion-based algorithms like EPSI (Estimation of Primaries and multiples by Sparse Inversion) van Groenestijn and Verschuur (2008) can circumvent the adaptive subtraction issues and produce even better estimates of the primary responses en their corresponding multiples.

All the above-mentioned techniques require densely and regularly sampled seismic data, especially in the 3D case where we need datasets like Wide Azimuth (WAZ) 3D surface seismic to obtain successful results (Aaron et al., 2008; Smith et al., 2011). However, in the case of datasets with sparse acquisition geometry, like sparse 3D surface seismic, 3D Ocean Bottom Node (OBN) data and 3D BSD surveys, the higher-order scatterings estimation and elimination algorithms will most likely fail.

1.2.2 Structural imaging

Once the higher-order scatterings are suppressed, the seismic data is then usually input into a one-step imaging algorithm, together with a migration velocity model, to produce a reflectivity image of the subsurface. Within the geophysical community, this process is referred to as pre-stack time/depth migration. There are various imaging methods that can be utilized (Claerbout, 1976; Robein, 2003, 2010) depending on the complexity of the studied area, however the main imaging techniques are based on the principles of the following algorithms:

- Kirchhoff migration (Schneider, 1978) is a widely utilized migration method especially in simple geological scenarios, like flat-layered and gently dipping geological models. It is a robust and computational efficient imaging method. The main feature of this method is that the travel times of the migration operator are calculated via ray tracing method, by solving for the Eikonal equation, and then the measured seismic data is summed along those travel times curves.

- Wave Equation Migration (WEM) methods (Stolt, 1978; Berkhout, 1982), like the Phase Shift Plus Interpolation (PSPI) algorithm (Gazdag and Sguazzero, 1984), are imaging techniques based on the one-way wave equation, where the source wavefield is forward propagated and the measured wavefield is backward propagated into the subsurface then an imaging condition is applied to produce the reflectivity image. The main assumption is that the wavefields are propagating through the subsurface in the up- and down-direction only. They are usually deployed in cases with more complex geological structures that require

more accurate migration operators. They can handle lateral velocity variations, steep events and complex structures in more accurate way compared to Kirchhoff migration techniques.

- Reverse Time Migration (RTM) (Baysal et al., 1983; Biondi and Shan, 2002) is an imaging technique that also forward propagate the source wavefield and backward propagate the measured data but in time in stead of depth and also based on the two-way wave equation. This means that RTM does not have dip-limitations or a preferred propagation direction, which produces better images especially in areas with very complex structures like salt domes. However, it is a computationally expensive algorithm and might suffer from artifacts.
- Least-Squares Migration (LSM) can be seen as the first inversion-imaging algorithm that shifted the seismic imaging process from a one step process to a feed-back loop structure (Nemeth et al., 1999). The estimated reflectivity image at every iteration is utilized in a so-called demigration algorithm to model the seismic data, which is then subtracted from the observed seismic measurements and the residual is fed to the imaging algorithm. The demigration algorithm is a forward modelling scheme based on the so-called Born approximation (Born and Wolf, 1980; Keys and Weglein, 1983). This means that only primary reflections will be modelled and the higher-order scatterings are neglected.

1.2.3 Migration velocity model building

The right migration operators are essential and crucial elements of every seismic imaging scheme. Therefore, great effort is usually spent in the building of an accurate migration velocity model. Conventionally, there are two main methods to construct and update the migration velocities:

- Normal move-out (NMO) velocity analysis is a traditional technique utilized in simple geological environments to determine stacking velocities, which maximizes the flatness of the seismic reflected events available in the Common Midpoint (CMP) gathers. This is done by constructing semblance panels for a number of CMP gathers at specific locations, where the NMO velocities are picked (Taner and Koehler, 1969). Based on empirical equations, these NMO velocities can be converted to interval velocities, which then can be input into a migration algorithm.
- Migration velocity analysis (MVA) is a more sophisticated technique

that aims at minimizing the residual move-outs and thereby maximizing the flatness of seismic events in the Common Image Point (CIP) gathers, which describe the angle-dependent reflection coefficient at every subsurface grid point (Kosloff et al., 1996; Biondi and Symes, 2004). This technique is based on the idea that the CIP gathers should be as flat as possible if the right velocity model is used and as long as residual move-outs (curved events) are observed in the CIP gathers, the velocity model should be updated accordingly.

- Full Waveform Inversion (FWI) (Tarantola, 1984) is an inversion tomography scheme that aims at updating the migration velocity model by minimizing the residual between the observed diving waves and the modelled ones based on the least-squares principles. The full waveform (phase and amplitude) of the diving waves is modelled using finite difference algorithm and is matched to the seismic data. Conventional FWI algorithms are sensitive to the starting velocity model and the presence of low frequencies in the seismic data (see e.g. Virieux and Operto, 2009). This is because of the strong non-linearity aspect of this inverse problem.

1.3 Non-Linear seismic imaging methods

As mentioned in the previous section all methods for the estimation and suppression of the higher-order scatterings do not produce accurate results in the case of datasets with sparse acquisition geometry. Therefore, over the past decade the focus has been shifted from the estimation and elimination toward the explanation and utilization of the higher-order scatterings (e.g. Whitmore et al., 2010; Verschuur and Berkhout, 2011; Lu et al., 2011; Zhang and Schuster, 2014). In fact it turned out that the multiples are a valuable source of extra information that might not even be available in the primaries (Davydenko and Verschuur, 2013, 2015; Soni and Verschuur, 2014), especially in the case of 3D BSD surveys, as will be demonstrated in this thesis (El Marhfoul and Verschuur, 2015). Figure 1.3a shows the primary upgoing wavefield that is usually utilized in conventional 3D BSD imaging, where reflectivity images can be produced only in the immediate vicinity of the borehole. Figure 1.3b shows the extended energy modes (higher-order scatterings) available in the 3D BSD data, which can be exploited to enhance the reflectivity image beyond the results of the primary-reflections imaging. This can be accomplished via the deployment of innovative data driven and non-linear inversion-imaging algorithms like Full Wavefield Migration (FWM)

and Joint Migration Inversion (JMI) (Berkhout (2014b); Berkhout (2014c)), which can handle the higher-order scatterings such that the multiples and primaries will complement and reinforce each other. Among the promising technologies that are being developed within the geophysical community we mention the followings:

- Full Wavefield Migration (FWM), which is also the subject of this thesis, is an inversion-imaging algorithm that aims at imaging and modelling the full wavefield –including multiple scattering– available in the seismic data (Berkhout, 2014b). This done via a least-squares mechanism, where the forward modelled data is continuously compared to the observed measurements and the reflectivity image is then updated accordingly until the residue has reached a minimum. In this way the resolution of the reflectivity image is enhanced and the crosstalk is removed.

- Marchenko Imaging is a recently developed promising algorithm, where both surface-related and internal multiples are automatically included in the imaging process (Behura et al., 2012; Slob et al., 2014; Wapenaar et al., 2014). It aims at including the effect of higher-order scatterings in the Green's functions to creating redatumed reflection responses with virtual sources and receivers in the subsurface. These responses contain accurate multiple's information of the inhomogeneous subsurface and can be utilized to obtain an image of the subsurface where the effect of the higher-order scatterings is suppressed. However, Marchenko algorithm requires regular and dense sampling at the sources and receivers side, which means that its application to 3D BSD surveys will be very challenging.

- Joint Migration Inversion (JMI) is a non-linear inversion scheme where the seismic data is parametrized in terms of subsurface reflectivity and propagation operators (Berkhout, 2014c). It can also be seen as an extension of the FWM algorithm to include the update of the migration velocities as well. This is accomplished via the principles of reflection tomography, where reflected seismic events are matched with the forward modelled data in terms of both dynamics (amplitude) and kinematics (phase). Note that in the case of 3D BSD surveys, where the seismic data also contains measured direct wavefields, one-way tomography is combined with two-way reflection tomography in one integrated JMI scheme. This will be demonstrated in this thesis.

- Reflection Full waveform Inversion (RFWI) is a recently developed ex-

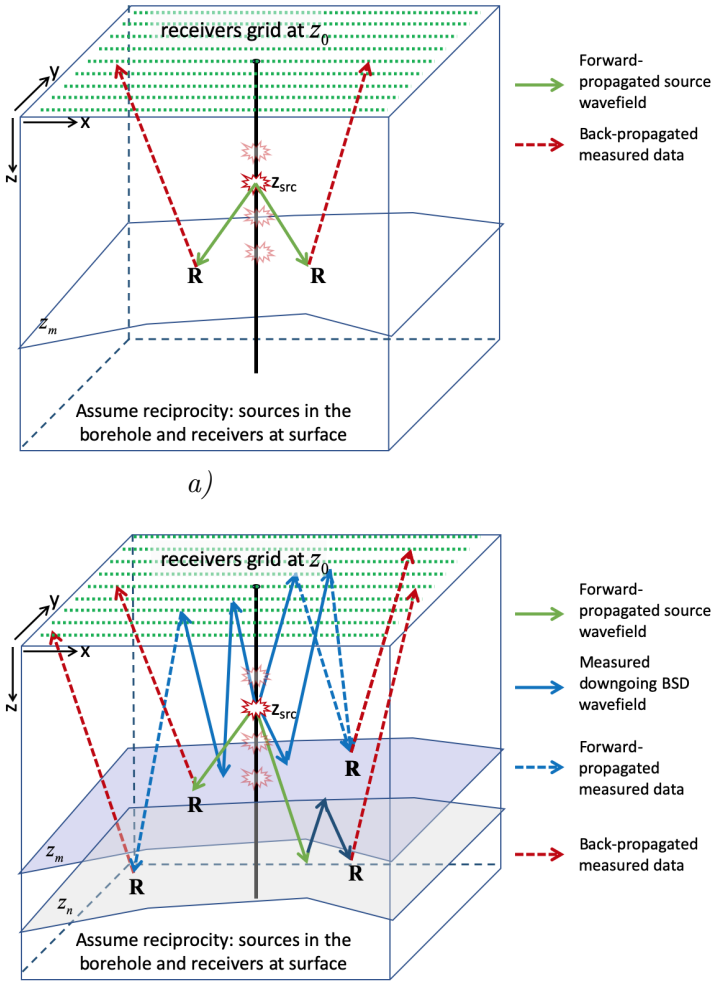

Figure 1.3: Schematic presentation of the different wavefields available in the 3D borehole seismic data. Usually reciprocity is assumed during the imaging phase, which means that the sources are in the borehole and the receivers are at the surface. a) The primary upgoing wavefield, which is traditionally utilized in conventional 3D BSD imaging. b) The full wavefield, including the downgoing wavefield, which is used in the FWM/JMI nonlinear inversion-imaging process. Note the complexity together with the additional energy modes of the wavefield in picture b).

tension of the traditional FWI by including the reflected events, available in the seismic data, in the inversion process (e.g. Sun et al., 2016, 2017; Irabor and Warner, 2016). This technology is aiming at circumventing issues like the requirement of long offset datasets in traditional FWI and also being trapped in a local minimum usually because of the absence of low frequencies in the seismic data and the poor starting velocity models, especially when combined with advanced objective functions Warner and Guasch (2016).

1.4 Thesis objectives

The primary objective of this thesis is to unlock the full potential of the 3D borehole seismic data such that it can be used as a tool for high-resolution imaging and monitoring of the subsurface together with the capability of updating the corresponding migration velocity model. This is realized by further engineering of the recently developed inversion-imaging algorithms Full Wavefield Migration (FWM) and Joint Migration Inversion (JMI) (Berkhout (2014b); Berkhout (2014c)) to properly handle and exploit the full wavefield available in the 3D borehole seismic data. The principal subjects that are addressed during the course of this work, which form also the main focus of this thesis can be listed as follows:

- Deployment of the full wavefield measured in 3D BSD surveys in the FWM inversion-imaging process to maximize the reliability and accuracy of the description of the earth's geological system.
- Development of an effective and practical strategy to update the migration velocity model despite the non-uniform fold distribution of 3D BSD surveys.
- Integration of seismic measurements from different surveys, like surface seismic and 3D BSD or multi-well 3D BSD, in one inversion-imaging process.
- Assessment of 3D BSD surveys as a tool for high-resolution reservoir monitoring.
- Investigation of the current challenges of the FWM and JMI algorithms in the case of datasets with elastic effects.
- Enhancement of the robustness of the JMI algorithm by the deployment of a cross-correlation based, instead of a residue-driven, objective function during the migration velocities update process.

1.5 Thesis unique contributions

The accelerated energy transition together with the new geophysical imaging and monitoring applications are forcing the geophysical scientific community to rethink the existing methodologies and strategies. The challenge is to retrieve more information about the earth's geological system with less measurements, which means limiting the acquisition geometry and costs. Therefore, we demonstrate how reliable estimates of the subsurface parameters can be achieved based on datasets with sparse acquisition geometry like 3D BSD and 3D OBN surveys. Moreover, integration of different seismic measurements, like surface seismic with BSD and also multi-well datasets, in one inversion-imaging scheme is a crucial step for increasing the integrity and reliability of our seismic solutions. The unique and new contributions of this dissertation can be listed as follows:

- 3D demonstration of the benefits and capabilities of full wavefield inversion-imaging algorithms, like FWM and JMI, to enhance the subsurface illumination by the deployment of higher-order scattering, especially in the case of datasets with sparse acquisition geometry.
- 3D demonstration that despite the sparse acquisition geometry of 3D BSD adequate estimates of the migration velocities can be achieved by combination of one-way with two-way tomography, with appropriate constraints, in one JMI process that utilizes simultaneously the measured directed wavefield and the full reflected wavefield.
- Providing a comprehensive and more complete, than what is often found in the literature, derivation of the involved gradients for the reflectivity image and velocity model update.
- Successful demonstration of the application of the developed 3D JMI algorithm on 3D field BSD acquired in a shallow water environment.
- Producing reliable 3D subsurface common image point (CIP) gathers based on the full wavefield of 3D BSD.
- A conclusive demonstration of the effects of the mode converted waves on the velocity model update and the reflectivity image when the current acoustic implementation of the FWM and JMI algorithms is utilized.

1.6 Thesis overview

Chapter 2

In this chapter, the Full wavefield Modelling (FWMod) algorithm will be discussed and explained. It can be seen as the backbone of the FWM and JMI algorithms, where the seismic data can be simulated including the higher-order scatterings. A major advantage of the FWMod algorithm compared to other modelling techniques, like the finite difference method, is the capability to include or exclude different energy modes of the seismic data in the forward modelling scheme. Note that this can be very convenient in some geological scenarios like shallow water-bottom environments, where only the multiples have a chance to properly describe and image the shallow near surface. The primary reflections (if there is any) should be excluded in that case from the inversion-imaging process otherwise they will block the convergence, because of inconsistency between the modelled data and the observed measurements.

Chapter 3

In this chapter, we will discuss the 3D FWM and JMI algorithms with an extensive derivation of the gradients for the reflectivity-image and velocity-model updates. Moreover, the velocity model gradient is complemented by the one-way tomography of the direct wavefield, which is always available in 3D BSD surveys. In addition the flexibility of implementing additional wave-phenomena effects like anisotropy and frequency-dependent amplitude attenuation in the migration operator is pointed out.

Chapter 4

In this chapter, we will demonstrate how the full potential of 3D BSD surveys, despite the sparse acquisition geometry, can be exploited based on the FWM and JMI algorithms. It turned out that, for instance, the downgoing wavefield, which is usually removed in conventional 3D BSD imaging, can produce results as good as the total upgoing wavefield. Moreover the significant added value of surface-related multiples will be demonstrated also for other datasets with sparse acquisition geometries like some 3D surface seismic surveys. We will demonstrate that the 3D FWM and JMI algorithms are able to provide reliable estimates of both the migration velocity and reflectivity model. This is mainly because the multiple scattering is improving the subsurface illumination and reinforcing the primary energy during the

inversion process.

Chapter 5

In this chapter, we will demonstrate the added value of the integration of different datasets in one inversion-imaging process. This will be shown via the simultaneous deployment of 3D BSD with surface seismic data and multi-well 3D BSD datasets in one FWM/JMI process. Note that in the case of 3D borehole data reciprocity is used, which means that the sources and receivers positions are exchanged, hence 3D buried-shot records are obtained and borehole seismic data becomes a regular 3D shot record with the source position in the subsurface. As long as for every particular dataset the adequate source wavelet or wavefield is deployed, an integrated solution for the reflectivity image and the migration velocity model will be obtained that exhibits the high-resolution characteristic of the 3D BSD and the areal consistency of the 3D surface seismic.

Chapter 6

In this chapter, the capability of the FWM algorithm to retrieve the time-lapse image using 3D BSD measurements is successfully demonstrated. Within the FWM framework, it is relatively straightforward to simultaneously invert the full wavefield including all high-order scattering from both up- and downgoing wavefields available in the 3D BSD measurements. The 3D data example presented in this chapter shows that 3D BSD surveys in combination with the FWM inversion-imaging algorithm can indeed provide reliable solutions and extend over quite an offset range to provide high-resolution information that will be of great added value for reservoir characterization and monitoring.

Chapter 7

In this chapter, the capability of the FWM algorithm in imaging and delineating steep events like salt flanks in a complex geological environment, based on 3D borehole data, will be demonstrated and emphasized. Also, the angle-dependent mode of the FWM algorithm to produce CIP gathers is demonstrated. we will demonstrate that in the case of 3D BSD measurements, the higher-order scattering have significant added value in providing additional reflection angles in areas beyond the coverage of the primary reflections.

In addition, the effect of strong converted waves, in the case of elastic datasets and based on the acoustic implementation of the FWM and JMI algorithms, on the reflectivity and velocity gradient will be demonstrated. It is expected that taking the converted waves into account in the the FWMod engine and utilize them as well in the FWM and JMI algorithm will resolve the noticed issues.

Chapter 8

In this chapter, the general conclusions of this thesis are presented together with recommendations for further research. Moreover, some preliminary results are presented regarding the comparison of different objective functions of the JMI algorithm in the case of migration velocity models with high-velocity contrast like geological environment with salt structures.

2

Full Wavefield Modelling

The purpose of seismic imaging is the determination of the subsurface reflectivity based on seismic measurements and a background propagation velocity model. Usually, those measurements are acquired at the surface or in a borehole and are related to the pressure or particle velocity of the wavefields that are propagating in the subsurface. These wavefields are influenced by the angle-dependent reflection coefficients of the boundaries in the subsurface. This raises the need for algorithms to predict and model the wavefield at every position in the subsurface based on certain input parameters. The most common way to determine a description of the wavefield, propagating in the subsurface, is by solving the two-way differential wave equation, which requires knowledge about the detailed velocity and density distribution (Virieux, 1986). Another method to model the subsurface wavefields is via Full Wavefield Modelling (FWMod), which is based on a two-way integral formulation of the scattered energy at every grid point in the subsurface (Berkhout, 2014a). The FWMod algorithm has as input parameters the angle-dependent reflection coefficients at every grid point and a smooth background velocity model. This parametrization in terms of angle-dependent reflectivity and smooth propagation operators offers a more suitable and consistent manner to move back and forward between the data space and the model-parameters space, especially when utilized in an inversion scheme, in order to optimize the reflectivity image and the propagation velocity model. In this

chapter, we consider only the acoustic case, although the angle-dependent reflection coefficient can be related to the elastic situation.

2.1 The integral formulation of the pressure wavefield

The Kirchoff and Rayleigh integrals are the main components in the wavefield extrapolation algorithms (Berkhout, 1982; Gisolf and Verschuur, 2010). Depending on the configuration of sources and receivers, wavefields can be predicted and extrapolated forward or backward in time and space. The Rayleigh II integral allows us to predict the the wavefield $P(x_A, y_A, z_A, \omega)$ from measurements at a different depth level z assuming that all sources that have created the wavefield $P(x, y, z, \omega)$ are located at larger depth values than the integration boundary z and point A is located at smaller depth values ($z_A < z$) in a homogeneous medium:

$$P(x_A, y_A, z_A, \omega) = 2 \int_{-\infty}^{\infty} \int_{-\infty}^{\infty} \frac{\partial G(\vec{r}_A; \vec{r}, \omega)}{\partial z} P(x, y, z, \omega) dx dy, \tag{2.1}$$

where $G(\vec{r}_A; \vec{r}, \omega)$ represents the Green's function of a point source at position $\vec{r_A}$ and measured at depth level z and is defined as follows:

$$G(\vec{r}_A; \vec{r}, \omega) = \frac{e^{-ik\sqrt{(x-x_A)^2+(y-y_A)^2+(z-z_A)^2}}}{4\pi\sqrt{(x-x_A)^2+(y-y_A)^2+(z-z_A)^2}}. \tag{2.2}$$

When carried out for all points along depth level z_A, this integral can be written as a spatial convolution process for forward extrapolation from the plane z to the plane z_A:

$$P(x_A, y_A, z_A, \omega) = \int_{-\infty}^{\infty} \int_{-\infty}^{\infty} W(x_A - x, y_A - y, z_A - z, \omega) P(x, y, z, \omega) dx dy, \tag{2.3}$$

with:

$$W(x, y, z_A - z, \omega) = 2 \frac{\partial G(\vec{r}_A; \vec{r}, \omega)}{\partial z}. \tag{2.4}$$

The Rayleigh II convolution integral becomes a simple multiplication in the k_x, k_y domain:

$$\tilde{P}(k_x, k_y, z_A, \omega) = \tilde{W}(k_x, k_y, z_A - z, \omega) \tilde{P}(k_x, k_y, z, \omega), \tag{2.5}$$

with $\tilde{W}(k_x, k_y, z_A - z, \omega)$ the double spatial Fourier transform of the operator $W(x, y, z_A - z, \omega)$. Typically for the case of homogeneous media, we can further simplify this operator into the analytical phase-shift operator in the k_x, k_y domain:

$$\begin{aligned} W(x, y, z_A - z, \omega) &= \frac{(z_A - z)}{2\pi} \frac{(1 + ik\sqrt{x^2 + y^2 + (z_A - z)^2})}{[x^2 + y^2 + (z_A - z)^2]^{\frac{3}{2}}} e^{-ik\sqrt{x^2+y^2+(z_A-z)^2}} \\ &= -\frac{1}{2\pi} \frac{\partial}{\partial z} \left[\frac{e^{-ik\sqrt{x^2+y^2+(z_A-z)^2}}}{\sqrt{x^2 + y^2 + (z_A - z)^2}} \right]. \end{aligned} \tag{2.6}$$

This means that $\tilde{W}(k_x, k_y, z_A - z, \omega)$ can be written as:

$$\begin{aligned} \tilde{W}(k_x, k_y, z_A - z, \omega) &= \int_{-\infty}^{\infty} \int_{-\infty}^{\infty} e^{ik_x x + ik_y y} W(x, y, z_A - z, \omega) dx dy \\ &= e^{-i(z_A - z)\sqrt{\frac{\omega^2}{c^2} - k_x^2 - k_y^2}}. \end{aligned} \tag{2.7}$$

This result is equal to the solution of the one-way wave equation A.20 and is valid for forward propagation of wavefields generated by sources above the plane z, which means that in the plane z there is only energy propagating in the positive z-direction.

$$\frac{\partial \tilde{P}^+}{\partial z} + ik_z \tilde{P}^+ = 0 \quad , \quad with \;\; k_z = \sqrt{\frac{\omega^2}{c^2} - k_x^2 - k_y^2}. \tag{2.8}$$

Based on the previous analysis, we can derive the phase shift operator that can predict wavefields at depth z_A based on measurements at plane z:

$$\tilde{P}^+(k_x, k_y, z_A, \omega) = e^{-i(z_A - z)k_z} \tilde{P}^+(k_x, k_y, z, \omega). \tag{2.9}$$

In the evanescent part of the wavefield where $\frac{\omega^2}{c^2} - k_x^2 - k_y^2 < 0$, the phase shift operator becomes an exponential damping factor and is equal to $e^{-\Delta z |k_z|}$, with $|k_z| = \sqrt{k_x^2 + k_y^2 - \frac{\omega^2}{c^2}}$ and $\Delta z = |z - z_A|$.

2.2 Full wavefield modelling

In the FWMod algorithm the total wavefield measured at the surface is considered to be a superposition of all the scattered wavefields in the subsurface,

forward propagated to the surface (Berkhout, 2014a). Moreover, the integral formulation of the pressure wavefield is used to design a propagation mechanism to bring wavefields from one depth level to another in the subsurface, where we assume smooth lateral inhomogeneity between those two depth levels. Note that the medium can be highly inhomogeneous in the vertical direction.

2.2.1 Discrete notation of wavefields

In principle, the FWMod algorithm can be divided into two major operations, namely scattering and propagation, which are performed recursively in depth. For that purpose, the subsurface is defined on a rectangular and regular grid where the wavefields and their corresponding operators are defined according to the framework of the vector and matrix notation as described by Berkhout (1982). For one-shot experiment and for one frequency component the wavefield at a certain depth level z_m is defined as a column vector $\vec{P}(z_m, \omega)$ where the elements represent values of the wavefield along the two-dimensional grid (x, y) (see also Kinneging et al., 1989):

$$\vec{P}(z_m,\omega) = \begin{bmatrix} P(x_1, y_1, z_m, \omega) \\ P(x_2, y_1, z_m, \omega) \\ \vdots \\ P(x_{N_x}, y_1, z_m, \omega) \\ P(x_1, y_2, z_m, \omega) \\ P(x_2, y_2, z_m, \omega) \\ \vdots \\ P(x_{N_x}, y_2, z_m, \omega) \\ \vdots \\ P(x_1, y_{N_y}, z_m, \omega) \\ P(x_2, y_{N_y}, z_m, \omega) \\ \vdots \\ P(x_{N_x}, y_{N_x}, z_m, \omega) \end{bmatrix}. \tag{2.10}$$

Note that for the 2D case the wavefield column vector reduces to:

$$\vec{P}(z_m,\omega) = \begin{bmatrix} P(x_1, z_m, \omega) \\ P(x_2, z_m, \omega) \\ \vdots \\ P(x_{N_x}, z_m, \omega) \end{bmatrix}. \tag{2.11}$$

For every grid point in the subsurface the angle-dependent reflectivity operator is defined as a two dimensional convolution with length Nh_x and Nh_y, where Nh_x and Nh_y are determined by the subsurface-offset range along the x and y directions. If we consider all grid points of one particular depth level z_m then the angle-dependent reflectivity operator can be represented as a square matrix $\mathbf{R}(z_m)$ having k rows and k columns, with k being the product of N_x and N_y, which are the total number of grid points in the x and y direction respectively:

$$\begin{bmatrix} r_1(x_1,y_1)\dots r_1(x_{N_x},y_1) & r_1(x_1,y_2)\dots r_1(x_{N_x},y_2)\dots r_1(x_1,y_{N_y})\dots r_1(x_{N_x},y_{N_y}) \\ r_2(x_1,y_1)\dots r_2(x_{N_x},y_1) & r_2(x_1,y_2)\dots r_2(x_{N_x},y_2)\dots r_2(x_1,y_{N_x})\dots r_2(x_{N_x},y_{N_y}) \\ \vdots & \\ r_k(x_1,y_1)\dots r_k(x_{N_x},y_1) & r_k(x_1,y_2)\dots r_k(x_{N_x},y_2)\dots r_k(x_1,y_{N_y})\dots r_k(x_{N_x},y_{N_y}) \end{bmatrix} \tag{2.12}$$

Figure 2.1 illustrates the structure of the 3D reflectivity matrix that represents the angle-dependent effects of the reflection coefficient (see also Kinneging et al., 1989). Note that the reflectivity operator $\mathbf{R}(z_m)$ has non-zero elements only within a limited range, in the h_x and h_y directions, around the location of the grid point.

2.2.2 Scattering operators

The reflected wavefield $\vec{P}^-(x,y,z_m,\omega)$ can be described in the space-frequency domain by a two dimensional convolution operation of the incident wavefield $\vec{P}^+(x,y,z_m,\omega)$ and the angle-dependent reflection coefficient $R(h_x,h_y)$.

$$\vec{P}^-(x,y,z_m,\omega) = \int\int \vec{P}^+(x-h_x,y-h_y,z_m,\omega)R(h_x,h_y;x,y)dh_xdh_y, \tag{2.13}$$

where h_x and h_y represent the subsurface offset in the x and y direction respectively. Note that in the case of angle-independent reflection coefficient R, the convolution operation becomes a simple multiplication of the incident wavefield $\vec{P}^+(x,y,z_m,\omega)$ with a single value per grid point (de Bruin, 1992).

Based on the description of the reflectivity matrix in the previous section the convolution process, for all grid points at depth level z_m, is similar to a matrix multiplication of the incident wavefield, as defined in equation 2.10, and the reflectivity matrix from equation 2.12. Moreover, by taking transmission effects as well into account, the total scattered wavefield at every

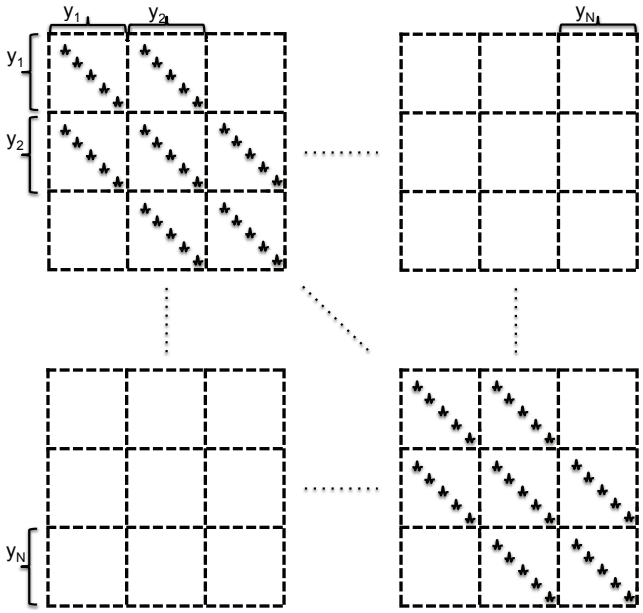

Figure 2.1: Schematic representation of the 3D reflectivity operator $\mathbf{R}(z_m)$ *for a particular depth level* z_m*. The non-zero elements along the diagonals represent the angle-dependent effects of the reflection coefficient.*

grid point in the subsurface can be determined by the wavefields that are approaching that grid point from above and from below together with the reflection and transmission operators. Figure 2.2 shows a schematic representation of the scattered wavefield at every grid point in the subsurface at a certain depth level z_m. The total wavefields that are leaving the grid point in the positive and negative z-directions can be described, according to the boundary conditions, as follows:

$$\vec{Q}^{+}(z_m) = \mathbf{T}^{+}(z_m)\vec{P}^{+}(z_m) + \mathbf{R}^{\cap}(z_m)\vec{P}^{-}(z_m) \tag{2.14a}$$

$$\vec{Q}^{-}(z_m) = \mathbf{T}^{-}(z_m)\vec{P}^{-}(z_m) + \mathbf{R}^{\cup}(z_m)\vec{P}^{+}(z_m), \tag{2.14b}$$

where $\vec{P}^{+}(z_m)$ and $\vec{P}^{-}(z_m)$ are the incident wavefields, in the (x, y) domain and for a single frequency component ω, reaching depth z_m from above and from below, respectively. $\mathbf{R}^{\cup}(z_m)$ and $\mathbf{R}^{\cap}(z_m)$ are the angle-dependent reflectivity matrices from above and below. $\mathbf{T}^{+}(z_m)$ and $\mathbf{T}^{-}(z_m)$ are the angle-dependent transmission matrices from above and below and can be seen as

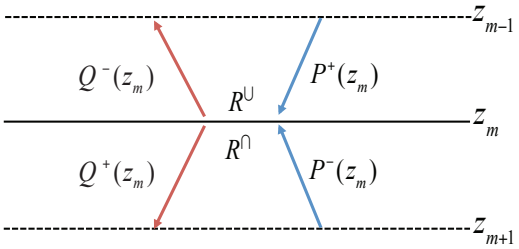

Figure 2.2: Schematic representation of the scattered wavefield at every grid point in the subsurface.

the sum of the unity matrix $\mathbf{I}$ and a small additional term $\delta\mathbf{T}^{\pm}$. In the acoustic case, all reflection effects can be described by one single operator $\mathbf{R}$, because $\mathbf{R}^{\cap}(z_m) = -\mathbf{R}^{\cup}(z_m)$ and $\delta\mathbf{T}^{\pm} = \pm\mathbf{R}$. Therefore, the transmission matrices in equation 2.14 become:

$$\mathbf{T}^{+} = \mathbf{I} + \delta\mathbf{T}^{+} \approx \mathbf{I} + \mathbf{R}^{\cup} = \mathbf{I} + \mathbf{R} \tag{2.15a}$$

$$\mathbf{T}^{-} = \mathbf{I} + \delta\mathbf{T}^{-} \approx \mathbf{I} + \mathbf{R}^{\cap} = \mathbf{I} - \mathbf{R}. \tag{2.15b}$$

Note that for elastic media these relationships are approximately still valid for small reflection/transmission angles.

Substitution of equation 2.15 in equation 2.14 gives the following expressions for the total wavefields $\vec{Q}^{+}(z_m)$ and $\vec{Q}^{-}(z_m)$:

$$\vec{Q}^{+}(z_m) = \vec{P}^{+}(z_m) + \mathbf{R}^{\cup}(z_m)\vec{P}^{+}(z_m) + \mathbf{R}^{\cap}(z_m)\vec{P}^{-}(z_m) = \vec{P}^{+}(z_m) + \delta\vec{S}(z_m) \tag{2.16a}$$

$$\vec{Q}^{-}(z_m) = \vec{P}^{-}(z_m) + \mathbf{R}^{\cup}(z_m)\vec{P}^{+}(z_m) + \mathbf{R}^{\cap}(z_m)\vec{P}^{-}(z_m) = \vec{P}^{-}(z_m) + \delta\vec{S}(z_m), \tag{2.16b}$$

with $\delta\vec{S}(z_m)$ represents the scattered wavefield at every grid point positioned at depth level z_m:

$$\delta\vec{S}(z_m) = \mathbf{R}^{\cup}(z_m)\vec{P}^{+}(z_m) + \mathbf{R}^{\cap}(z_m)\vec{P}^{-}(z_m). \tag{2.17}$$

Notice that even though the angle-dependent reflectivity operator $\mathbf{R}$ is always considered along a horizontally oriented axis the FWMod mechanism remains valid when utilized in an inversion scheme, as will be explained in the next chapter, to simulate seismic data even in the case of dipping reflectors. This

is mainly because the estimation of the angle-dependent reflectivity operator **R**, in the imaging phase, is consistent with its application in the modelling phase. However, for the purpose of interpretation, the angle-dependent reflectivity operator **R** can easily be mapped and transformed into an axis along the reflecting boundary in order to be consistent with the expressions of the angle-dependent reflection coefficient from the Zoeppritz equations. This is achieved based on the the work of Sava and Fomel (2003) and Sava and Vasconcelos (2011) by stretching the subsurface-offset gathers back to time along the depth axis, using the imaging velocity model, and applying a 3D Radon transform. This will convert the subsurface-offset gathers directly from the horizontally-oriented subsurface-offset domain to the reflection-angle domain that is oriented along the subsurface boundaries.

2.2.3 Extrapolation operator and recursive modelling

The total scattered wavefield at depth level z_m is decomposed into a wavefield propagating upward and another one propagating downward. These two wavefields can then easily be extrapolated to the next depth level via the phase shift operator as is derived in section 2.2. The spatial convolution operation from equation 2.3 can be rewritten as follows:

$$\vec{P}^{\pm}(x, y, z_m \pm \Delta z, \omega) = \int\int W(h_x, h_y; x, y, \Delta z, \omega)\vec{P}^{\pm}(x - h_x, y - h_y, z_m, \omega)dh_x dh_y, \quad (2.18)$$

where $W(h_x, h_y; x, y, \Delta z, \omega)$ is the inverse spatial double Fourier-transformed version of the phase shift operator $\tilde{W}(k_x, k_y; x, y, \Delta z, \omega) = e^{-ik_z \Delta z}$. In analogy with the angle-dependent reflectivity operator **R**, as described in the previous section, the convolution operation from equation 2.18 can be replaced by matrix multiplication by constructing the phase shift operator **W** as a square matrix, with the same dimension as the reflectivity operator **R**, where each row representing the Green's function belonging to a particular grid point (x, y) along the depth level $z_m \pm \Delta z$. The underlying assumption here is the smoothly inhomogeneous layer between the two depth levels, every time we extrapolate the wavefield based on the local background velocity at every grid point (x, y) along the depth level $z_m \pm \Delta z$. The total wavefields $\vec{Q}^{+}(z_m)$ and $\vec{Q}^{-}(z_m)$ that are leaving a certain depth level z_m are then extrapolated to the next depth level to obtain the incident wavefields

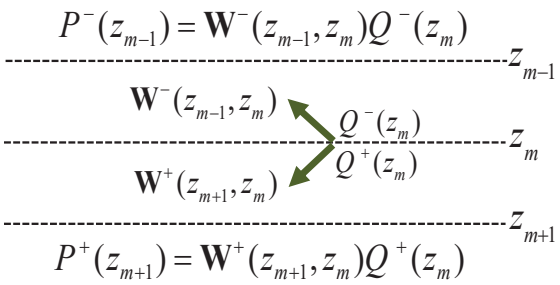

Figure 2.3: Recursive propagation of the scattered wavefields between consecutive depth levels in the subsurface.

$\vec{P}^+(z_{m+1})$ and $\vec{P}^-(z_{m-1})$, as is shown in the following equations:

$$\vec{P}^+(z_{m+1}) = \mathbf{W}^+(z_{m+1}, z_m)\vec{Q}^+(z_m) \tag{2.19a}$$

$$\vec{P}^-(z_{m-1}) = \mathbf{W}^-(z_{m-1}, z_m)\vec{Q}^-(z_m), \tag{2.19b}$$

where the plus and minus sign in $\mathbf{W}^+(z_{m+1}, z_m)$ and $\mathbf{W}^-(z_{m-1}, z_m)$ indicates downward and upward propagation of the wavefields. Note that both propagation operators have the same mathematical definition. Figure 2.3 shows a schematic representation of the recursive construction of the up- and downgoing wavefields in the subsurface. In the FWMod algorithm, we assume that the downgoing wavefield $\vec{P}^+(z_0)$ and the upgoing wavefield $\vec{P}^-(z_N)$ are equal to 0 immediately outside the modelling grid. If we also assume that the scattering operator $\delta\vec{S}$ is known too, we can then, based on equations 2.16 and 2.19 formulate the following modelling scheme for the downgoing wavefield at depth level z_m:

$$
\begin{aligned}
\vec{P}^{+}(z_m) &= \mathbf{W}^{+}(z_m, z_{m-1}) \left[\vec{P}^{+}(z_{m-1}) + \delta\vec{S}(z_{m-1}) \right] \\
&= \mathbf{W}^{+}(z_m, z_{m-1}) \vec{P}^{+}(z_{m-1}) + \mathbf{W}^{+}(z_m, z_{m-1}) \delta\vec{S}(z_{m-1}) \\
&= \mathbf{W}^{+}(z_m, z_{m-1}) \mathbf{W}^{+}(z_{m-1}, z_{m-2}) \left[\vec{P}^{+}(z_{m-2}) + \delta\vec{S}(z_{m-2}) \right] + \\
&\quad \mathbf{W}^{+}(z_m, z_{m-1}) \delta\vec{S}(z_{m-1}) \\
&= \mathbf{W}^{+}(z_m, z_{m-2}) \left[\vec{P}^{+}(z_{m-2}) + \delta\vec{S}(z_{m-2}) \right] + \mathbf{W}^{+}(z_m, z_{m-1}) \delta\vec{S}(z_{m-1}) \\
&= \mathbf{W}^{+}(z_m, z_{m-2}) \vec{P}^{+}(z_{m-2}) + \mathbf{W}^{+}(z_m, z_{m-2}) \delta\vec{S}(z_{m-2}) + \\
&\quad \mathbf{W}^{+}(z_m, z_{m-1}) \delta\vec{S}(z_{m-1}) \\
&= \mathbf{W}^{+}(z_m, z_0) \delta\vec{S}(z_0) + \cdots + \mathbf{W}^{+}(z_m, z_{m-2}) \delta\vec{S}(z_{m-2}) + \\
&\quad \mathbf{W}^{+}(z_m, z_{m-1}) \delta\vec{S}(z_{m-1}).
\end{aligned}
$$

This means that:

$$
\vec{P}^{+}(z_m) = \sum_{n=0}^{m-1} \mathbf{W}^{+}(z_m, z_n) \delta\vec{S}(z_n), \tag{2.20}
$$

where $\mathbf{W}^{+}(z_m, z_n)$ is a cumulative propagation operator that brings the scattered wavefield related to depth level z_n to the depth level z_m, with $n < m$, and which is formulated as follows:

$$
\mathbf{W}^{+}(z_m, z_n) = \mathbf{W}^{+}(z_m, z_{m-1}) \mathbf{W}^{+}(z_{m-1}, z_{m-2}) \times \cdots \times \mathbf{W}^{+}(z_{n+1}, z_n). \tag{2.21}
$$

In a similar manner we can derive the following scheme for the upgoing wavefield at depth level z_m:

$$
\begin{aligned}
\vec{P}^{-}(z_m) &= \mathbf{W}^{-}(z_m, z_{m+1}) \left[\vec{P}^{-}(z_{m+1}) + \delta\vec{S}(z_{m+1}) \right] \\
&= \mathbf{W}^{-}(z_m, z_{m+1}) \vec{P}^{-}(z_{m+1}) + \mathbf{W}^{-}(z_m, z_{m+1}) \delta\vec{S}(z_{m+1}) \\
&= \mathbf{W}^{-}(z_m, z_{m+1}) \mathbf{W}^{-}(z_{m+1}, z_{m+2}) \left[\vec{P}^{-}(z_{m+2}) + \delta\vec{S}(z_{m+2}) \right] + \\
&\quad \mathbf{W}^{-}(z_m, z_{m+1}) \delta\vec{S}(z_{m+1}) \\
&= \mathbf{W}^{-}(z_m, z_{m+2}) \left[\vec{P}^{-}(z_{m+2}) + \delta\vec{S}(z_{m+2}) \right] + \mathbf{W}^{-}(z_m, z_{m+1}) \delta\vec{S}(z_{m+1}) \\
&= \mathbf{W}^{-}(z_m, z_{m+2}) \vec{P}^{-}(z_{m+2}) + \mathbf{W}^{-}(z_m, z_{m+2}) \delta\vec{S}(z_{m+2}) + \\
&\quad \mathbf{W}^{-}(z_m, z_{m+1}) \delta\vec{S}(z_{m+1}) \\
&= \mathbf{W}^{-}(z_m, z_N) \delta\vec{S}(z_N) + \cdots + \mathbf{W}^{-}(z_m, z_{m+2}) \delta\vec{S}(z_{m+2}) + \\
&\quad \mathbf{W}^{-}(z_m, z_{m+1}) \delta\vec{S}(z_{m+1}).
\end{aligned}
$$

This means that:

$$\vec{P}^{-}(z_m) = \sum_{n=m+1}^{N} \mathbf{W}^{-}(z_m, z_n)\delta\vec{S}(z_n), \tag{2.22}$$

where $\mathbf{W}^{-}(z_m, z_n)$ is a cumulative propagation operator that brings the scattered wavefield related to depth level z_n to the depth level z_m, with $n > m$, and is formulated as follows:

$$\mathbf{W}^{-}(z_m, z_n) = \mathbf{W}^{-}(z_m, z_{m+1})\mathbf{W}^{-}(z_{m+1}, z_{m+2}) \times \cdots \times \mathbf{W}^{+}(z_{n-1}, z_n). \tag{2.23}$$

The scattering operator $\delta\vec{S}(z_n)$ depends on the angle-dependent reflectivity operator $\mathbf{R}(z_n)$, the downgoing wavefield $\vec{P}^{+}(z_n)$ and the upgoing wavefield $\vec{P}^{-}(z_n)$ at depth level z_n. These wavefields depend on their turn on the scattering operators from the surrounding depth levels. This means that the FWMod modelling scheme must be performed in an iterative manner where one iteration consists of a downward depth recursion, followed by an upward depth recursion through the modelling grid (Berkhout, 2014a). At every iteration, the donwgoing and upgoing wavefields are updated as well as the scattering operators $\delta\vec{S}(z_n)$ until all orders of scattering are generated. In practice, the amplitude of higher-order scatterings decay very rapidly and usually only a small number of iterations is required to accurately simulate the seismic data. Note that the FWMod modelling scheme is similar and consistent with the approach of the generalized Bremmer series that found its first application in the description and modelling of optical waves (Bremmer, 1951).

2.2.4 Buried sources and BSD acquisition geometry

In the case of a physical experiment with an active source at depth level z_{src}, the downgoing and upgoing wavefields become:

$$\vec{P}^{+}(z_m) = \sum_{n=0}^{m-1} \mathbf{W}^{+}(z_m, z_n)\left[\vec{S}^{+}(z_n) + \delta\vec{S}(z_n)\right], \tag{2.24}$$

$$\vec{P}^{-}(z_m) = \sum_{n=m+1}^{N} \mathbf{W}^{-}(z_m, z_n)\left[\vec{S}^{-}(z_n) + \delta\vec{S}(z_n)\right], \tag{2.25}$$

where $\vec{S}^{+}(z_n)$ and $\vec{S}^{-}(z_n)$ are the components of the physical source field for the downward and upward directions that are equal to zero for all depth levels

except when $z_n = z_{src}$. Based on these formulation we can now describe the upgoing wavefield $\vec{P}^-(z_0)$ measured at the surface z_0 as follows:

$$\vec{P}^-(z_0) = \sum_{n=1}^{N} \mathbf{W}^-(z_0, z_n) \left[\vec{S}^-(z_n) + \delta\vec{S}(z_n) \right], \tag{2.26}$$

where $\mathbf{W}^-(z_0, z_n)$ is a cumulative propagation operator that brings the scattered wavefield at depth level z_n to the surface z_0. Note that in the case of borehole seismic data the sources are in most cases at the surface and the receivers in the borehole. However, during the inversion-imaging process we assume reciprocity and we exchange the sources and receivers positions with each other. In this way, the total number of shots to be processed is determined by the limited number of receivers in the borehole instead of the original number of shots, at the surface, that can be extremely large.

2.2.5 Ghost effects in marine environment

In the case of marine acquisition for 3D surface seismic data, where the sources and receivers are towed at some depth z_{src} and z_{rcv}, the ghost effects can be included by taking into account the ghost operator at the source and receiver side (Berkhout and Blacquière, 2014). This means that the physical source term in equation 2.24 becomes:

$$\vec{S}^+(z_{src}) = \mathbf{\Psi}^+(z_{src})\vec{S}_0(z_{src}), \tag{2.27}$$

where $\vec{S}_0(z_{src})$ describes the ghost-free source directivity and strength, $\mathbf{\Psi}^+(z_{src})$ is the ghost matrix at the source side given by:

$$\mathbf{\Psi}^+(z_{src}) = \left[\mathbf{I} + \mathbf{W}^+(z_{src}, z_0)\mathbf{R}^{\cap}(z_0)\mathbf{W}^-(z_0, z_{src}) \right], \tag{2.28}$$

with $\mathbf{R}^{\cap}(z_0)$ representing the angle dependent reflectivity matrix at the sea surface and $\mathbf{I}$ the unity matrix. In a similar manner we can describe the ghost effect at the detector side and equation 2.25 becomes:

$$\vec{P}^-(z_{rcv}) = \sum_{n=z_{rcv}+1}^{N} \mathbf{D}_0(z_{rcv})\mathbf{\Psi}^-(z_{rcv})\mathbf{W}^-(z_{rcv}, z_n) \left[\vec{S}^-(z_n) + \delta\vec{S}(z_n) \right], \tag{2.29}$$

where $\mathbf{D}_0(z_{rcv})$ is the ghost-free detector matrix and $\mathbf{\Psi}^-(z_{rcv})$ is the ghost matrix at the detector side described as follows:

$$\mathbf{\Psi}^-(z_{rcv}) = \left[\mathbf{I} + \mathbf{W}^+(z_{rcv}, z_0)\mathbf{R}^{\cap}(z_0)\mathbf{W}^-(z_0, z_{rcv}) \right]. \tag{2.30}$$

Note that for 3D borehole data we have to account only for the receivers ghost because we use reciprocity, which means that the sources are in the borehole and the receivers are at the surface at a certain elevation (see also Chapter 1). This description of ghost effects in terms of matrix multiplications, which is independent of the complexity of the subsurface, allows us to design robust deghosting algorithms to enhance the measured seismic data. For a comprehensive description of the deghosting schemes the reader is referred to Berkhout and Blacquière (2014).

2.3 Full wavefield modelling versus finite difference method

In order to demonstrate the full wavefield modelling algorithm, a 3D layered model with a simple 1D profile is constructed as is depicted in figure 2.4. The model consists of three horizontal boundaries with low velocity contrasts but relatively high density contrasts. By ignoring the angle-dependent

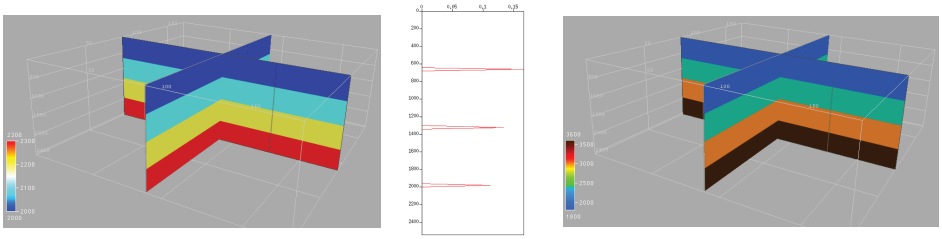

a) b) c)

Figure 2.4: 3D model used to demonstrate the full wavefield algorithm. a) The 3D layered velocity model. b) The reflectivity profile. c) The 3D layered density model.

reflectivity behaviour, the scalar reflectivity profile at depth level z_m can be obtained based on the acoustic impedance ρc according to the following equation:

$$\mathbf{R}(z_m) = \frac{\rho_{z_{m+1}} c_{z_{m+1}} - \rho_{z_m} c_{z_m}}{\rho_{z_{m+1}} c_{z_{m+1}} + \rho_{z_m} c_{z_m}} \cdot \mathbf{I}, \tag{2.31}$$

where ρ_{z_m} is the density and c_{z_m} is the propagation velocity just below depth level z_m and $\rho_{z_{m-1}}$ is the density and $c_{z_{m-1}}$ is the propagation velocity just above depth level z_m. A point source is placed at the center of the model with

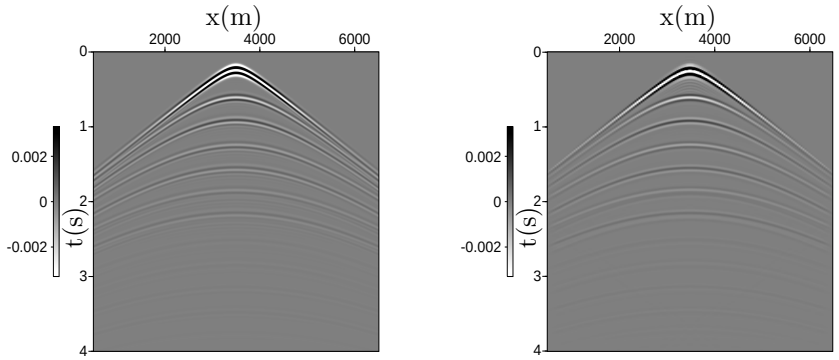

Figure 2.5: Comparison between finite difference modelling and the full wavefield modelling algorithm, where the reflectivity operator $\mathbf{R} = -\mathbf{I}$ *at the surface* $z = 0$*. a) Cross-section from the 3D seismic shot record generated via a 3D finite difference algorithm. b) The same cross-section generated via the full wavefield modelling algorithm.*

$z_{src} = 300m$, which is $200m$ above the first reflector. We have used a Ricker wavelet with peak frequency of $10Hz$ and a dense receiver grid is placed at the surface z_0. Note that this acquisition geometry configuration is similar to the case of having a common receiver gather from a 3D BSD dataset with the receiver positioned at depth $z = 300m$ in the borehole. In the FWMod algorithm the scattering operator at every depth level z_m is determined based on the reflectivity model and the wavefields $\vec{P}^{+}(z_m)$ and $\vec{P}^{-}(z_m)$, which are updated during several downward and subsequent upward depth recursions. The background propagation velocity model is used to extrapolate the scattered data, at every depth level z_m, towards the next depth level. On the other hand, in finite difference modelling the two-way wave equation is solved numerically by discretizing the solution domain and taking linear approximations of the derivatives in the wave equation. Moreover the wavefield at z_0 is equal to zero and therefore the receiver grid is put at the next depth level below z_0. This means that the seismic shot record will include ghost effects at the receivers side, when the free surface boundary condition is used. The effect of the ghost can be taken into account in the FWMod algorithm, however, in this experiment it was excluded and we applied just a phase rotation to match the phase of the FWMod shot record with the finite difference one for the sake of demonstration. The amplitude spectrum will be different of course. Figure 2.5 displays a comparison, of a cross-section from the 3D modelled shot record, between an acoustic finite difference algorithm with a

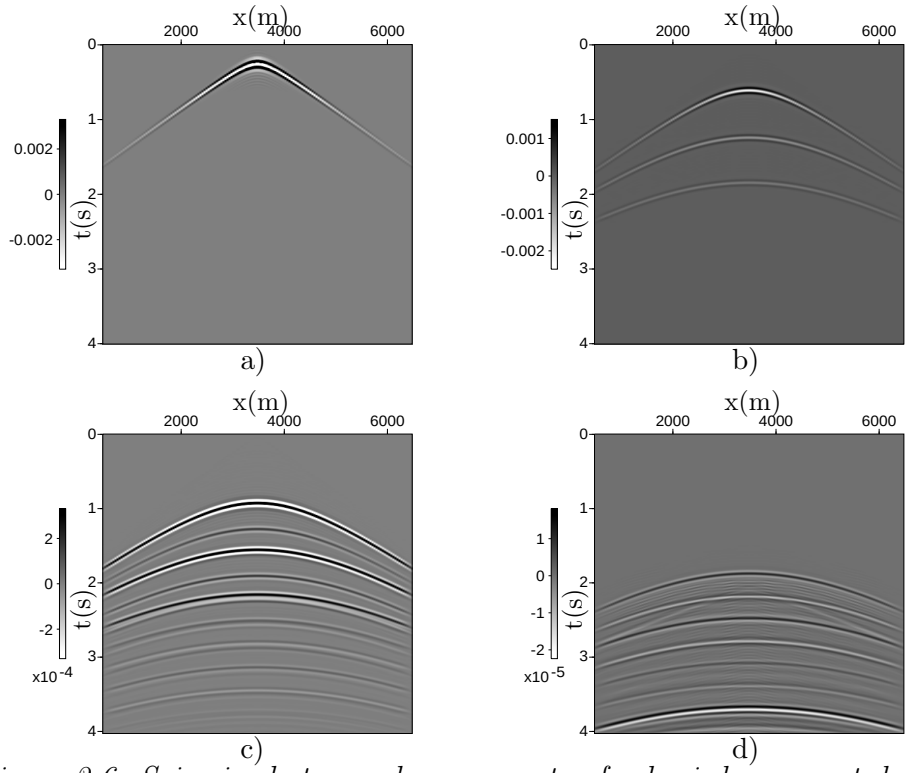

Figure 2.6: Seismic shot record components of a buried source at depth $z_{src} = 300m$, generated in the $1.5D$ model from figure 2.4, using full wavefield modelling algorithm a) The direct wavefield. b) The primary reflections. c) The surface-related multiples. d) The internal multiples. Note that the multiples generated by the direct wavefield are also included; these multiples are usually referred to as 'downgoing wavefield' in the borehole seismic geophysical community.

free surface boundary condition and the FWMod algorithm. The results are consistent with each other in terms of the kinematics of the generated seismic events. The angle-dependent effects are not severe mainly because of the low velocity contrasts and the high density contrast. In the FWMod section, the events are fading away at the edges mainly because of the used taper to damp wraparound effects. A useful feature in the FWMod algorithm is that the order of the multiple scattering depends on the number of performed depth recursions. This enables us to isolate and include or exclude the multiples from the simulated shot record, as is displayed in Figure 2.6.

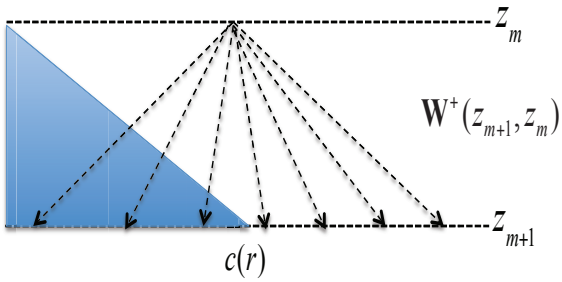

Figure 2.7: Schematic representation of the PSPI propagation operator between consecutive depth levels in the subsurface. The blue triangle represents a dipping layer with high lateral velocity contrast.

2.4 Full wavefield modelling in media with high lateral heterogeneity

The FWMod algorithm uses the phase shift operator to propagate the pressure wavefield between depth levels in the subsurface. The phase shift operator is consistent with the solution of the one-way wave equation, where the underlying assumption is the lateral homogeneity of the propagation velocities in the subsurface. In the case of media with gently varying lateral velocity contrasts, the Phase Shift Plus Interpolation (PSPI) algorithm offers an adequate solution for accurate handling of smooth lateral velocity variations in the subsurface (Gazdag and Sguazzero, 1984). The PSPI algorithm extrapolates the wavefield by using the velocity at every location via an efficient interpolation scheme of extrapolated wavefields based on predefined reference velocities. This means that, when we extrapolate from depth level z_m to z_{m+1}, the wave propagation velocity $c(\vec{r})$ becomes a function of only the lateral position $\vec{r}$ at depth level z_{m+1} of the extrapolated wavefield, see figure 2.7. This will result in erroneous propagation operators in the case of media with high lateral heterogeneity. A more accurate and pragmatic approach would be to extend the PSPI algorithm to take the propagation velocities at the depth level z_m of the input wavelfield as well into account. For a more generalized solution of the migration propagator in media with high lateral heterogeneity the reader is referred to Wapenaar (1996), de Hoop (1996) and Hammad and Verschuur (2018). Moreover, the one-way wave equation is based on the decomposition of the total pressure wavefield into wavefields that propagate only upward or downward in the depth direction,

which means that horizontally propagating wavefields, like diving waves, are ignored. This will cause loss of valuable imaging information especially in the case of borehole measurements, where the receivers might be positioned along vertical structures like salt flanks. In that case, the FWMod algorithm will not model those events unless the modelling grid is flipped to consider wave propagation in the lateral direction (see Davydenko et al., 2014).

2.5 Discussion

In this chapter we have discussed the FWMod algorithm, with its two main components namely the scattering operator at every grid point in the subsurface and the propagation mechanism to extrapolate pressure wavefields between depth levels. Moreover, a comparison with the finite difference method is shown using a simple $1.5D$ model. The major advantages of the FWMod algorithm are computation efficiency, especially when utilized in an inversion procedure, as will be discussed in the next chapter, and the freedom in including or excluding the different energy modes that are present in seismic data in the modelling process. On the other hand, the finite difference method remains an excellent tool to simulate seismic data, but when it is utilized in an inversion scheme, the latter becomes inefficient and highly non-linear (Berkhout, 2012). Our current implementation of the FWMod algorithm uses the PSPI algorithm to handle propagation in media with lateral velocity variations. This might not be accurate enough especially in the case of media with high lateral velocity contrasts. However, when the FWMod is utilized in an inversion scheme the propagation velocities should be allowed to be modified and updated, even if the true velocity model is utilized as a starting velocity model, such that an effective processing velocity model can be obtained that produces more accurate propagation operators to fit the measured seismic data.

3

Joint Migration Inversion

Major challenges in seismic imaging are the determination of accurate migration velocities and the proper handling of higher-order scattering energy modes. The Joint Migration Inversion (JMI) technology is developed to address these challenges and offers an advanced imaging algorithm that utilizes all energy modes available in the measured seismic data (i.e.primaries and multiples) via an iterative inversion process (Berkhout, 2014b,c). Especially in the case of coarse acquisition geometries, such as with 3D BSD or OBN data, the use of all propagation modes is crucial for adequate illumination of the subsurface. This will enhance the quality of seismic images and improve our understanding of the subsurface (El Marhfoul and Verschuur, 2017). In addition, JMI restores the transmission effects and also removes the cross-talk of surface and internal multiples from the final image and focuses their energy into the right position in the subsurface. This is accomplished by using the Full Wavefield Modelling algorithm (FWMod), described in the previous chapter, to simulate seismic data and then subtract it from the observed data. Next, the residue is translated, in an alternating manner, into a reflectivity gradient to update the seismic image and a slowness gradient to update the erroneous starting migration velocity model. The final output of the JMI algorithm is a high-resolution structural seismic image of the subsurface along with its corresponding updated migration velocity model (Verschuur et al., 2016). After having finalized the JMI process, it is possible to fix the velocity

model and perform the so-called Angle-dependent Full Wavefield Migration (AD-FWM) to produce high-resolution subsurface-offset gathers that include the illumination of all higher-order scattering energy modes (i.e. primaries and multiples). These subsurface-offset gathers can be converted into the reflection-angle domain, based on the work of Sava and Vasconcelos (2011), by applying a 3D Radon transform and produce common image point (CIP) gathers that can be utilized as input for (conventional) pre-stack elastic inversion algorithms.

3.1 Objective function of the JMI algorithm

With the recently developed paradigm of JMI, as explained by Berkhout (2014c), the modelled data are iteratively compared to the measured data, after having updated both the reflectivity and the velocity model. By closing the loop in the inversion-imaging process and feeding back the residual data into the JMI engine, optimized reflectivity and velocity models will be obtained, which is illustrated in Figure 3.1.

In the case of 3D borehole or OBN seismic data, we apply reciprocity, meaning that we assume sources in the borehole or on the ocean bottom and receivers at the surface. This means that we obtain 3D common receiver gathers that become 3D shot gathers similar to surface seismic data with the source position at a certain depth z_n. Therefore, the following cost-function will be minimized, based on a gradient descent scheme:

$$J = \frac{1}{2} \sum_{k} \sum_{\omega} \parallel \vec{P}^{-}_{obs}(z_0) - \vec{P}^{-}_{mod}(z_0) \parallel^2, \tag{3.1}$$

where $\vec{P}^{-}_{obs}(z_0)$ represents the observed data and $\vec{P}^{-}_{mod}(z_0)$ is the modelled data for shot gather k detected at the measurements-surface z_0. The subscript ω indicates the summation over all frequencies and the subscript k indicates the summation over all seismic shot gathers. Note that in Equation 3.1 we should write $\vec{P}^{-}_{k,obs}(z_0)$ and $\vec{P}^{-}_{k,mod}(z_0)$, but for the sake of readability, we omit the subscript k. By substituting Equation 2.22 in Equation 3.1 we obtain the following expression for the objective function:

$$J = \frac{1}{2} \sum_{k} \sum_{\omega} ||\vec{P}^{-}_{obs}(z_0) - \sum_{n=1}^{N} \mathbf{W}^{-}(z_0, z_n) \delta\vec{S}(z_n)||^2. \tag{3.2}$$

Equation 3.2 shows that the JMI objective function is described by the propagation operator $\mathbf{W}$ and the scattering operator $\delta\vec{S}$, which is a function of the

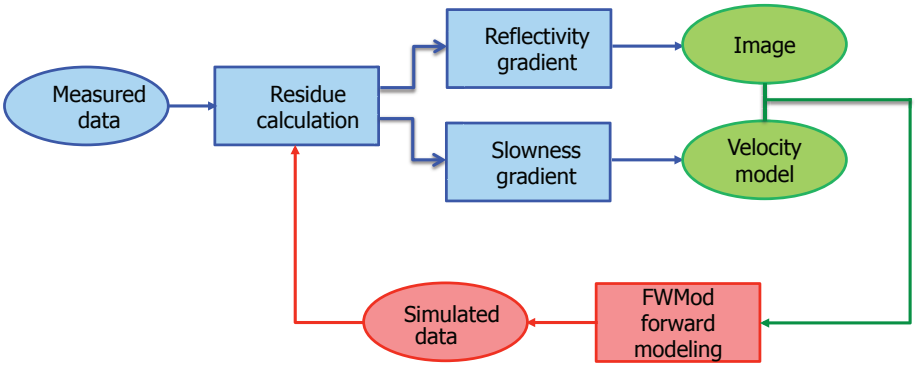

Figure 3.1: Block diagram explaining the inversion process of joint migration inversion. The modelled data is continuously compared to the input data after updating the model parameters, being the reflectivity image and the migration velocity model.

reflectivity operator **R**, as can be seen in Equation 2.17. In order to make the inversion process less non-linear and to avoid being trapped into local minima we can assume that the propagation operator **W** and the reflectivity operator **R** are decoupled, meaning independent of each other. This means that the propagation operator **W** will affect only the kinematics of the wavefields, and is not allowd to include any scattering, while the reflectivity operator **R** will be concerned with all amplitude effects. This will circumvents some of the non-linearity issues faced in traditional Full Waveform Inversion (FWI) (see e.g. Virieux and Operto, 2009), as was illustrated by Verschuur et al. (2016). Moreover, this decoupling enables us to derive two separate gradients one for the reflectivity operator **R** and one for the propagation operator **W** to update the erroneous velocity and reflectivity models independent of each other. Once we are close to the right solution we can link the propagation operator **W** with the reflectivity operator **R** by imposing a so-called reflectivity constraint on the objective function. It is an additional condition minimizing the difference between the derivative of the acoustic impedance and the estimated reflectivity. This will enable the JMI algorithm to retrieve more details into the solution of the propagation velocity model and improve the convergence process (Masaya and Verschuur, 2018).

3.2 Gradient for the reflectivity operator

The JMI algorithm utilizes a gradient descent scheme to optimize the reflectivity and the propagation velocity model. Therefore, the gradient of the objective function with respect to the model parameters must be calculated. By substituting Equation 2.17 for the scattering operator $\delta\vec{S}$ in Equation 3.2 we can describe the objective function J in terms of the model parameters $\mathbf{R}^{\cup}$, which indicates the reflectivity operator from the upward side of the reflector, and $\mathbf{R}^{\cap}$, which indicates the reflectivity operator from the downward side of the reflector:

$$J = \frac{1}{2}\sum_{k}\sum_{\omega}||\vec{P}^{-}_{obs}(z_0) - \sum_{n=1}^{N}\mathbf{W}^{-}(z_0,z_n)\mathbf{R}^{\cup}(z_n)\vec{P}^{+}(z_n) - \sum_{n=1}^{N}\mathbf{W}^{-}(z_0,z_n)\mathbf{R}^{\cap}(z_n)\vec{P}^{-}(z_n)||^2. \tag{3.3}$$

In order to calculate the gradient of the objective function with respect to the reflectivity operator $\mathbf{R}^{\cup}$ we make use of of the following rule according to Petersen and Pedersen (2012):

$$\frac{\partial}{\partial\mathbf{X}}\left[(\mathbf{AXB}+\mathbf{C})(\mathbf{AXB}+\mathbf{C})^H\right] = 2\mathbf{A}^H(\mathbf{AXB}+\mathbf{C})\mathbf{B}^H. \tag{3.4}$$

This means that the gradient of the objective function J with respect to the reflectivity operator $\mathbf{R}^{\cup}$ can be written as follows:

$$\frac{\partial J}{\partial\mathbf{R}^{\cup}(z_n)} = \sum_{k}\sum_{\omega}\left[\mathbf{W}^{-}(z_0,z_n)\right]^H\left[\vec{P}^{-}_{obs}(z_0) - \vec{P}^{-}_{mod}(z_0)\right]\left[\vec{P}^{+}(z_n)\right]^H. \tag{3.5}$$

Equation 3.5 describes a cross correlation between the forward modelled incident wavefield $\vec{P}^{+}(z_n)$ and the data misfit $\left[\vec{P}^{-}_{obs}(z_0) - \vec{P}^{-}_{mod}(z_0)\right]$ backward propagated to depth level z_n with the propagation operator $[\mathbf{W}^{-}(z_0,z_n)]^H$. This operation is similar to the application of a conventional imaging condition except in this case the incident wavefield $\vec{P}^{+}(z_n)$ contains the primary source wavefield and all higher-order scatterings as well. This will automatically allows us to image surface and internal multiples at the last bounce of the corresponding event. Figure 3.2 displays a schematic representation of the the gradient calculation for the reflectivity operator $\mathbf{R}^{\cup}(z_n)$.

In a similar manner we can calculate the gradient of the objective function with respect to the reflectivity operator $\mathbf{R}^{\cap}$. For that purpose we substitute

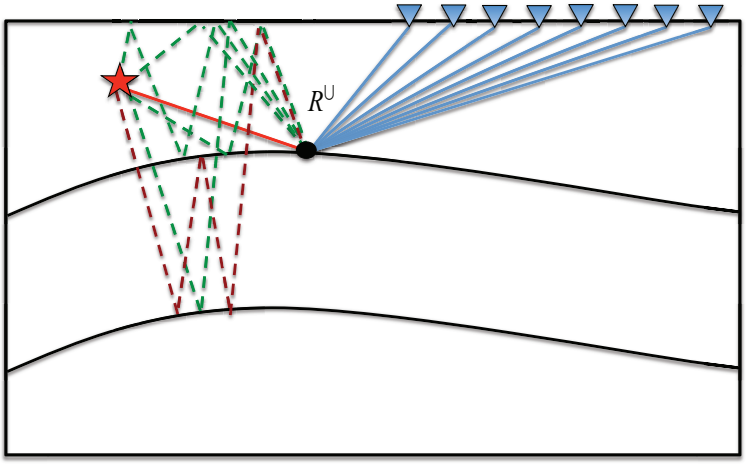

Figure 3.2: Schematic illustration of the calculation of the gradient for the reflectivity from above. The data misfit, indicated in blue, is back propagated to every imaging depth level and cross-correlated with the downgoing forward modelled wavefield at every lateral location, as is indicated by the black dot. Note the complexity of the downgoing forward modelled wavefield that contains the primary incident wavefield (red) and all higher-order scatterings (green and brown).

the expression of the incident wavefield $\vec{P}^{+}$ from Equation 2.20, together with Equation 2.17 for the scattering operator $\delta\vec{S}$, in Equation 3.3 to obtain the following expression:

$$
\begin{aligned}
J = \frac{1}{2}\sum_{k}\sum_{\omega} ||\vec{P}^{-}_{obs}(z_0) - \\
&\sum_{n=1}^{N}\mathbf{W}^{-}(z_0,z_n)\mathbf{R}^{\cup}(z_n)\left[\sum_{m=0}^{n-1}\mathbf{W}^{+}(z_n,z_m)\mathbf{R}^{\cup}(z_m)\vec{P}^{+}(z_m)\right] - \\
&\sum_{n=1}^{N}\mathbf{W}^{-}(z_0,z_n)\mathbf{R}^{\cup}(z_n)\left[\sum_{m=0}^{n-1}\mathbf{W}^{+}(z_n,z_m)\mathbf{R}^{\cap}(z_m)\vec{P}^{-}(z_m)\right] - \\
&\sum_{n=1}^{N}\mathbf{W}^{-}(z_0,z_n)\mathbf{R}^{\cap}(z_n)\vec{P}^{-}(z_n)||^2.
\end{aligned}
\tag{3.6}
$$

Equation 3.6 shows that we now have two variables z_n and z_m indicating the depth levels variation, with $z_n > z_m$. This means that we can take the

derivative of the objective function J with the respect to $\mathbf{R}^{\cap}(z_n)$ or with respect to $\mathbf{R}^{\cap}(z_m)$ in order to obtain the gradient for the reflectivity from below $\mathbf{R}^{\cap}$. The third term in Equation 3.6 contains the reflectivity operator $\mathbf{R}^{\cap}(z_m)$ and considering it for one particular depth level z_m yields:

$$\sum_{n=m+1}^{N} \mathbf{W}^{-}(z_0, z_n)\mathbf{R}^{\cup}(z_n)\left[\mathbf{W}^{+}(z_n, z_m)\mathbf{R}^{\cap}(z_m)\vec{P}^{-}(z_m)\right], \tag{3.7}$$

with $m \geq 0$. By using again the rule from Equation 3.3 we can calculate the gradient of the objective function with the respect to the reflectivity from below $\mathbf{R}^{\cap}(z_m)$:

$$\begin{aligned}\frac{\partial J}{\partial \mathbf{R}^{\cap}(z_m)} = \sum_{k}\sum_{\omega}\left[\sum_{n=m+1}^{N} \mathbf{W}^{-}(z_0, z_n)\mathbf{R}^{\cup}(z_n)\mathbf{W}^{+}(z_n, z_m)\right]^{H} \\ \left[\vec{P}^{-}_{obs}(z_0) - \vec{P}^{-}_{mod}(z_0)\right]\left[\vec{P}^{-}(z_m)\right]^{H}.\end{aligned} \tag{3.8}$$

Equation 3.8 describes a cross correlation between forward modelled upgoing wavefield $\vec{P}^{-}(z_m)$ and the data misfit $\left[\vec{P}^{-}_{obs}(z_0) - \vec{P}^{-}_{mod}(z_0)\right]$ backward propagated toward every depth level z_n below the imaging depth level z_m, then scaled with the reflectivity operator $\mathbf{R}^{\cup}(z_n)$ of that particular depth level and backward propagated toward the imaging depth level z_m with the propagation operator $[\mathbf{W}^{+}(z_n, z_m)]^{H}$. Note that this operation is mainly concerned about the imaging of all orders of internal multiples at one depth position prior to the last bounce of the corresponding event. This can be very helpful especially in areas with shadow zones and gaps in the acquisition geometry (Davydenko and Verschuur, 2017). Figure 3.3 displays a schematic representation of the the gradient calculation for the reflectivity operator $\mathbf{R}^{\cap}(z_m)$. As was explained in the previous chapter, in the acoustic case we assume that $\mathbf{R}^{\cap}(z_n) = -\mathbf{R}^{\cup}(z_n)$, which means that we can focus mainly on the reflectivity from above and the internal multiples will be imaged at the last bounce of the corresponding reflector, as indicated in Figure 3.2. However, for examples where the reflectivity from below is used in a more active way the reader is referred to Davydenko and Verschuur (2013) and Davydenko and Verschuur (2017).

3.3 Reflectivity update

The solution for the reflectivity operator $\mathbf{R}$ is optimized via an iterative process by minimizing the difference between the observed and the modelled

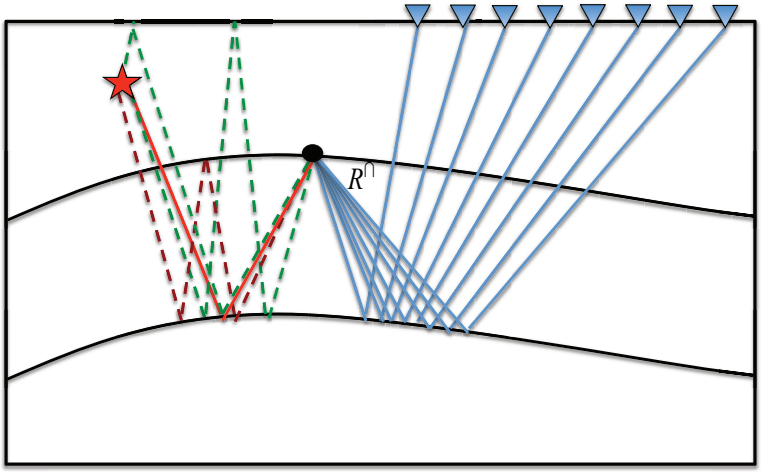

Figure 3.3: Schematic illustration of the calculation of the gradient of the reflectivity from below. The data misfit, indicated in blue, is back propagated toward every depth level below the imaging depth level, then scaled with the reflectivity operator of that particular depth level and back propagated toward the imaging depth level. Finally, that wavefield is cross-correlated with the upgoing forward modelled wavefield at every lateral location as is indicated by the black dot. Note the complexity of the upgoing forward modelled wavefield that illuminates the reflector from below and contains all higher-order scatterings.

data. Actually, when the velocity model is assumed known, this reflectivity update can be used as stand alone process called Full Wavefield Migration (FWM) (Berkhout, 2014b; Davydenko and Verschuur, 2017). During the JMI process, where we also have to update the erroneous propagation velocity model, the reflectivity operator $\mathbf{R}$ is kept angle-independent with elements only along its diagonal. This is mainly done to avoid exchanging and confusing velocity errors with angle dependency (Sun et al., 2018). In practice, for angle-dependent imaging the propagation velocity model is kept constant and the reflectivity operator is updated via the Angle-Dependent Full Wavefield Migration (AD-FWM) process (Davydenko, 2016). In the JMI process, the scalar reflectivity operator $\mathbf{R}$ at a certain iteration i can be described and updated as follows:

$$\mathbf{R}_i = \mathbf{R}_{i-1} + \alpha \Delta \mathbf{R}, \tag{3.9}$$

where $\Delta\mathbf{R}$ is the reflectivity update that can be obtained based on the gradient of the objective function $\frac{\partial J}{\partial \mathbf{R}}$ depending on whether a conjugate gradient or a steepest decent scheme is utilized. α is the step length, obtained via a line search procedure and determined based on the following initial scaling factor:

$$\alpha = \frac{\sum_k \sum_\omega \left(\left[\Delta\vec{P}^-(z_0) \right]^H \vec{E}^-(z_0) + \left[\vec{E}(z_0) \right]^H \Delta\vec{P}^-(z_0) \right)}{\sum_k \sum_\omega \left(2 \left[\Delta\vec{P}^-(z_0) \right]^H \Delta\vec{P}^-(z_0) \right)}, \tag{3.10}$$

where $\vec{E}^-(z_0) = \left[\vec{P}^-_{obs}(z_0) - \vec{P}^-_{mod}(z_0) \right]$ represents the data misfit at iteration i and $\Delta\vec{P}^-(z_0)$ is the wavefield perturbation that corresponds with the current reflectivity update $\Delta\mathbf{R}$ and can be calculated as follows:

$$\Delta\vec{P}^-(z_0) = \sum_{n=1}^{N} \mathbf{W}^-(z_0, z_n) \Delta\mathbf{R}^\cup(z_n) \vec{P}^+(z_n). \tag{3.11}$$

3.4 Gradient for the propagation operator

In order to be able to update the migration velocity model, the gradient of the objective function from Equation 3.3 with respect to the migration velocity c or its corresponding slowness $\sigma = \frac{1}{c}$ must be derived. However, the objective function is described in terms of the propagation operator $\mathbf{W}$, which is a phase shift operator based on the one-way wave equation and is a non-linear function of the slowness σ in the wavenumber domain but still affecting purely the phase of the wavefields:

$$\tilde{W}(k_x, k_y; \omega) = e^{-i\Delta z \sqrt{\omega^2\sigma^2 - k_x^2 - k_y^2}}. \tag{3.12}$$

3.4.1 Linearisation of the phase-shift operator

The phase-shift operator is linearised by taking its Taylor expansion up to the second term around the current and background value of the slowness σ_0. This will enable us to calculate the gradient of the objective function with

respect to the slowness σ.

$$\tilde{W}(k_x, k_y; \omega) \approx \tilde{W}_0(k_x, k_y; \omega) + \left[\frac{\partial \tilde{W}(k_x, k_y; \omega)}{\partial \sigma}\right]_{\sigma_0} (\sigma - \sigma_0) \tag{3.13}$$

$$\approx \tilde{W}_0(k_x, k_y; \omega) - i\omega\Delta z \left[\frac{k}{k_z}\right]_{\sigma_0} \tilde{W}_0(k_x, k_y; \omega)\Delta\sigma \tag{3.14}$$

$$\approx \tilde{W}_0(k_x, k_y; \omega) + \Delta\tilde{W}(k_x, k_y; \omega), \tag{3.15}$$

where $\tilde{W}_0(k_x, k_y; \omega) = e^{-i\Delta z\sqrt{\omega^2\sigma_0^2 - k_x^2 - k_y^2}}$ is the phase-shift operator defined in the background medium and $\Delta\tilde{W}(k_x, k_y; \omega)$ is the linearised difference between the true and the background phase-shift operator and is defined as follows:

$$\Delta\tilde{W}(k_x, k_y; \omega) = -i\omega\Delta z \left[\frac{k}{k_z}\right]_{\sigma_0} \tilde{W}_0(k_x, k_y; \omega)\Delta\sigma. \tag{3.16}$$

This means that an update in the propagation operator can easily be translated into an update of the slowness and hence an update of the propagation velocity model.

3.4.2 Gradient for the velocity model update

The gradient for the propagation operator $\mathbf{W}$ between two consecutive depth levels z_m and z_{m+1} has tow contribution from $\mathbf{W}^-(z_m, z_{m+1})$ and $\mathbf{W}^+(z_{m+1}, z_m)$ that can be added together. In order to derive the gradient w.r.t. the operator in the upward direction $\mathbf{W}^-(z_m, z_{m+1})$ we must consider only scattering effects that are happening beneath depth level z_m and therefore we rewrite the objective function from Equation 3.2 as follows:

$$\begin{aligned} J = \frac{1}{2}\sum_k \sum_\omega ||\vec{P}^-_{obs}(z_0) - \sum_{n=1}^{m} \mathbf{W}^-(z_0, z_n)\delta\vec{S}(z_n) - \\ \sum_{n=m+1}^{N} \mathbf{W}^-(z_0, z_n)\delta\vec{S}(z_n)||^2. \end{aligned} \tag{3.17}$$

The propagation operator $\mathbf{W}^-(z_0, z_n)$ can then be decomposed into two parts as follows:

$$\mathbf{W}^-(z_0, z_n) = \mathbf{W}^-(z_0, z_m)\mathbf{W}^-(z_m, z_n). \tag{3.18}$$

Filling in this into Equation 3.17 we obtain the following formulation for the objective function:

$$J = \frac{1}{2}\sum_{k}\sum_{\omega}||\vec{P}^{-}_{obs}(z_0) - \sum_{n=1}^{m}\mathbf{W}^{-}(z_0,z_n)\delta\vec{S}(z_n) - \mathbf{W}^{-}(z_0,z_m)\sum_{n=m+1}^{N}\mathbf{W}^{-}(z_m,z_n)\delta\vec{S}(z_n)||^2. \tag{3.19}$$

Note that the last summation represents the total upgoing wavefield at depth level z_m based on Equation 2.22 and consequently the objective function becomes:

$$J = \frac{1}{2}\sum_{k}\sum_{\omega}||\vec{P}^{-}_{obs}(z_0) - \sum_{n=1}^{m}\mathbf{W}^{-}(z_0,z_n)\delta\vec{S}(z_n) - \mathbf{W}^{-}(z_0,z_m)\vec{P}^{-}(z_m)||^2. \tag{3.20}$$

By substitution of the expression for the incident wavefield $\vec{P}^{-}(z_m)$ from Equation 2.19 we then obtain:

$$J = \frac{1}{2}\sum_{k}\sum_{\omega}||\vec{P}^{-}_{obs}(z_0) - \sum_{n=1}^{m}\mathbf{W}^{-}(z_0,z_n)\delta\vec{S}(z_n) - \mathbf{W}^{-}(z_0,z_m)\mathbf{W}^{-}(z_m,z_{m+1})\vec{Q}^{-}(z_{m+1})||^2. \tag{3.21}$$

As can be seen from Equation 3.21 the objective function is now a function of the propagation operator in the upward direction $\mathbf{W}^{-}(z_m,z_{m+1})$ and therefore its gradient w.r.t. $\mathbf{W}^{-}(z_m,z_{m+1})$ can be derived, in analogy with the derivation of the gradient for the reflectivity operator $\mathbf{R}$, as follows:

$$\frac{\partial J}{\partial \mathbf{W}^{-}(z_m,z_{m+1})} = \sum_{k}\sum_{\omega}\left[\mathbf{W}^{-}(z_0,z_m)\right]^{H}\left[\vec{P}^{-}_{obs}(z_0) - \vec{P}^{-}_{mod}(z_0)\right]\left[\vec{Q}^{-}(z_{m+1})\right]^{H}, \tag{3.22}$$

where $\left[\vec{P}^{-}_{obs}(z_0) - \vec{P}^{-}_{mod}(z_0)\right]$ is again the data misfit at depth level z_0, $\vec{Q}^{-}(z_{m+1})$ is the total wavefield leaving depth level z_{m+1} toward depth level z_m as defined in Equation 2.14. Equation 3.22 describes a cross-correlation between the total forward-modelled upgoing wavefield $\vec{Q}^{-}(z_{m+1})$ and the data misfit $\left[\vec{P}^{-}_{obs}(z_0) - \vec{P}^{-}_{mod}(z_0)\right]$ backward propagated to depth level z_m with the propagation operator $\mathbf{W}^{-}(z_0,z_m)$. Note that both wavefields are propagating in

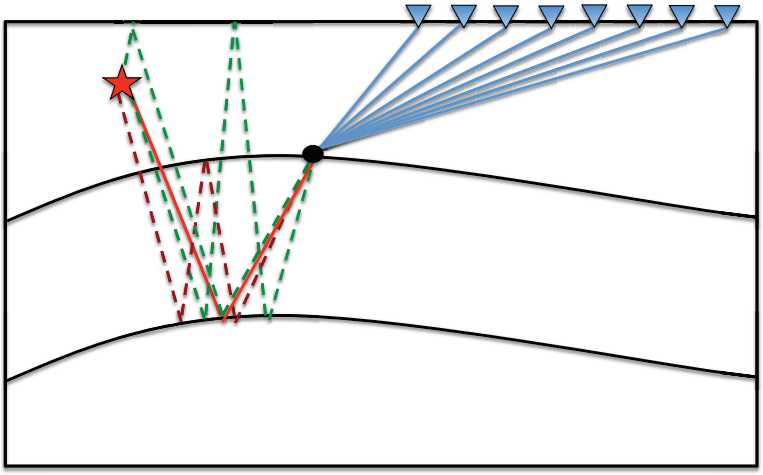

Figure 3.4: Schematic illustration of the calculation of the gradient of the propagation operator in the upward direction. The data misfit, indicated in blue, is back propagated toward every imaging depth level and is cross-correlated with the total upgoing forward-modelled wavefield, that is leaving depth level z_{n+1}, at every lateral location as is indicated by the black dot. Note the complexity of the upgoing forward modelled wavefield that contains primary energy (red) and all higher-order scatterings (green and brown).

the same upward direction and that the upgoing wavefield $\vec{Q}^{-}(z_{m+1})$ contains the primary source wavefield and all higher-order scatterings as well. This will automatically allow us to include surface and internal multiples in updating the velocity model. Figure 3.4 displays a schematic representation of the the gradient calculation for the propagation operator $\mathbf{W}^{-}(z_m, z_{m+1})$.

In a similar way we can evaluate the gradient of the objective function for the propagation operator in the downward direction $\mathbf{W}^{+}(z_{m+1}, z_m)$ and for that purpose we substitute the expression of the incident wavefields $\vec{P}^{+}(z_m)$ and $\vec{P}^{-}(z_m)$ from Equation 2.19 into the objective function from equation

3.6 to obtain the following formulation:

$$
\begin{aligned}
J = \frac{1}{2}\sum_{k}\sum_{\omega} ||\vec{P}^{-}_{obs}(z_0) - \\
\sum_{n=1}^{N} \mathbf{W}^{-}(z_0, z_n)\mathbf{R}^{\cup}(z_n)\left[\sum_{m=1}^{n-1} \mathbf{W}^{+}(z_n, z_m)\mathbf{R}^{\cup}(z_m)\mathbf{W}^{+}(z_m, z_{m-1})\vec{Q}^{+}(z_{m-1})\right] - \\
\sum_{n=1}^{N} \mathbf{W}^{-}(z_0, z_n)\mathbf{R}^{\cup}(z_n)\left[\sum_{m=0}^{n-1} \mathbf{W}^{+}(z_n, z_m)\mathbf{R}^{\cap}(z_m)\mathbf{W}^{-}(z_m, z_{m+1})\vec{Q}^{-}(z_{m+1})\right] - \\
\sum_{n=1}^{N} \mathbf{W}^{-}(z_0, z_n)\mathbf{R}^{\cap}(z_n)\mathbf{W}^{-}(z_n, z_{n+1})\vec{Q}^{-}(z_{n+1})||^2.
\end{aligned}
\tag{3.23}
$$

We consider the second term from Equation 3.23 for one particular depth level z_m:

$$
\sum_{n=m+1}^{N} \mathbf{W}^{-}(z_0, z_n)\mathbf{R}^{\cup}(z_n)\left[\mathbf{W}^{+}(z_n, z_m)\mathbf{R}^{\cup}(z_m)\mathbf{W}^{+}(z_m, z_{m-1})\vec{Q}^{+}(z_{m-1})\right], \tag{3.24}
$$

with $m \geq 0$. The derivation of the gradient of the objective function with respect to the propagation operator in the downward direction $\mathbf{W}^{+}(z_{m+1}, z_m)$ between depth levels z_m and z_{m+1} is the same as for $\mathbf{W}^{+}(z_m, z_{m-1})$ between depth levels z_{m-1} and z_m and therefore is equal to:

$$
\frac{\partial J}{\partial \mathbf{W}^{+}(z_{m+1}, z_m)} = \sum_{k}\sum_{\omega}\left[\mathbf{V}^{+}(z_0, z_{m+1})\right]^{H}\left[\vec{P}^{-}_{obs}(z_0) - \vec{P}^{-}_{mod}(z_0)\right]\left[\vec{Q}^{+}(z_m)\right]^{H}, \tag{3.25}
$$

where $\mathbf{V}^{+}(z_0, z_{m+1})$ is defined as follows:

$$
\mathbf{V}^{+}(z_0, z_{m+1}) = \sum_{n=m+2}^{N} \mathbf{W}^{-}(z_0, z_n)\mathbf{R}(z_n)\mathbf{W}^{+}(z_n, z_{m+1})\mathbf{R}(z_{m+1}). \tag{3.26}
$$

Equation 3.25 describes a cross-correlation between the total forward modelled downgoing wavefield $\vec{Q}^{+}(z_m)$ that is leaving depth level z_m and the data misfit $\left[\vec{P}^{-}_{obs}(z_0) - \vec{P}^{-}_{mod}(z_0)\right]$ backward propagated toward every depth level z_n below the imaging depth level z_{m+1}, then scaled with the reflectivity operator $\mathbf{R}^{\cup}(z_n)$ of that particular depth level and backward propagated toward the imaging depth level z_{m+1}. Note again that both wavefields are propagating in the same downward direction and that the downgoing wavefield $\vec{Q}^{+}(z_m)$

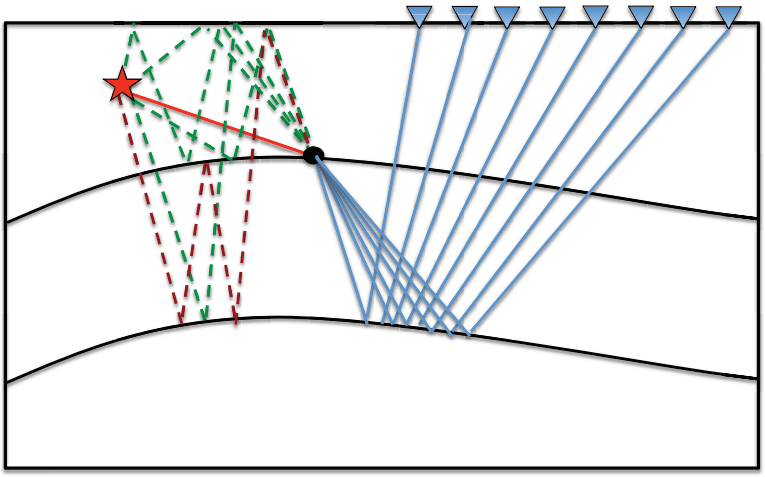

Figure 3.5: Schematic illustration of the calculation of the gradient of the propagation operator in the downward direction. The data misfit, indicated in blue, is back propagated toward every depth level below the imaging depth level then scaled with the reflectivity operator of that particular depth level and back propagated toward the imaging depth level. Finally that wavefield is cross-correlated with the total downgoing forward-modelled wavefield, that is leaving depth level z_m, at every lateral location as is indicated by the black dot. Note the complexity of the downgoing forward modelled wavefield that contains primary energy (red) and all higher-order scatterings (green and brown).

contains the primary source wavefield and all higher-order scatterings as well. Figure 3.5 displays a schematic representation of the the gradient calculation for the propagation operator $\mathbf{W}^{+}(z_{m+1}, z_m)$. Note that both gradients are related to velocity errors in the layer between depth level z_m and z_{m+1} and therefore we can choose to assign their corresponding update to depth level z_m or z_{m+1}.

Furthermore, with the linearised approximation between $\tilde{W}$ and $\Delta\sigma$ (Equation 3.16) we can relate the gradients of the propagation operator $\mathbf{W}$ to the

gradient of the slowness σ:

$$\begin{aligned}\frac{\partial J}{\partial \sigma(z_m)} = &\sum_k \sum_\omega \left[\mathbf{G}(z_m, z_{m+1})\right]^H \frac{\partial J}{\partial \mathbf{W}^-(z_m, z_{m+1})} + \\ &\sum_k \sum_\omega \left[\mathbf{G}(z_{m+1}, z_m)\right]^H \frac{\partial J}{\partial \mathbf{W}^+(z_{m+1}, z_m)},\end{aligned} \tag{3.27}$$

where $\mathbf{G}$ is an operator that is defined in the (k_x, k_y) domain as follows:

$$\tilde{G}(k_x, k_y; \omega) = -j\omega\Delta z \left[\frac{k k_z^*}{k_z k_z^* + \epsilon}\right]_{\sigma_0} \tilde{W}_0(k_x, k_y; \omega), \tag{3.28}$$

where $\tilde{W}_0(k_x, k_y; \omega)$ is the propagation operator in the background medium σ_0, k_z^* is the complex conjugate of k_z and ϵ is a stabilisation factor. Note that the gradient of the slowness $\frac{\partial J}{\partial \sigma(z_m)}$ is a matrix, with the same dimension as the propagation operator $\mathbf{W}$, and where the off-diagonal elements represent a description of the angle-dependent slowness parameter $\sigma(\theta)$, with θ being the phase angle as described by the eikonal equation (Fei and Liner, 2008). This means that anisotropy effects can be derived and updated in a similar manner as for the calculation of the angle-dependent reflectivity operator, without the limitations of any pre-assumed parametrization for the subsurface anisotropy type. However, this is beyond the scope of this thesis and we limit the slowness update to the diagonal elements that represent the vertical slowness parameter.

3.5 Slowness update

As we have seen in the previous section the gradient for the propagation operator can be translated into an update of the slowness σ by using the parametrization as described in Equation 3.16. Furthermore, in a similar way as for the reflectivity operator $\mathbf{R}$, the propagation velocity model is optimized via an iterative process by minimizing the difference between the observed and the modelled data. This is achieved by alternating between updating the reflectivity model and the velocity model during the JMI process. According to the optimization gradient scheme the angle-independent slowness σ_i at a certain iteration i can be described and updated as follows:

$$\sigma_i = \sigma_{i-1} + \alpha\Delta\sigma, \tag{3.29}$$

where $\Delta\sigma$ is the slowness update that can be obtained based on the gradient of the objective function $\frac{\partial J}{\partial \sigma}$ depending on whether a conjugate gradient or

a steepest decent scheme is utilized. α is the step length, obtained via a line search procedure and determined based on the following initial scaling factor:

$$\alpha = \frac{\sum_k \sum_\omega \left(\left[\Delta \vec{P}^-(z_0) \right]^H \vec{E}^-(z_0) + \left[\vec{E}(z_0) \right]^H \Delta \vec{P}^-(z_0) \right)}{\sum_k \sum_\omega \left(2 \left[\Delta \vec{P}^-(z_0) \right]^H \Delta \vec{P}^-(z_0) \right)}, \tag{3.30}$$

where $\vec{E}^-(z_0) = \left[\vec{P}^-_{obs}(z_0) - \vec{P}^-_{mod}(z_0) \right]$ represents the data misfit at iteration i and $\Delta \vec{P}^-(z_0)$ is the wavefield perturbation that corresponds to the current slowness update $\Delta\sigma$ and can be calculated as follows:

$$\begin{aligned} \Delta \vec{P}^-(z_0) = & \sum_{n=1}^{N} \mathbf{V}^-(z_0, z_n) \Delta\sigma(z_n) \mathbf{G}^-(z_n, z_{n+1}) \vec{Q}^-(z_{n+1}) \\ & + \sum_{n=1}^{N} \mathbf{V}^+(z_0, z_{n+1}) \mathbf{G}^+(z_{n+1}, z_n) \Delta\sigma(z_n) \vec{Q}^+(z_n). \end{aligned} \tag{3.31}$$

3.6 Reflectivity-constraint Joint Migration Inversion

The main unique characteristic of the JMI algorithm is the parametrization of seismic data in terms of reflectivity and propagation operators in the forward modelling engine. Moreover, these two parameters are assumed to be decoupled, which makes the inversion process less non-linear and stabilizes the convergence process especially in the case when the starting velocity model is not close enough to the true model. However, in reality the reflectivity is by definition a function of the propagation velocities and therefore a more accurate approach could be realised by imposing additional constraints on the objective function. For example, requiring that the solutions of the JMI inversion process should be consistent with the empirical relationship between the reflectivity and the acoustic impedance. This means that the estimated JMI reflectivity should be consistent with the reflectivity that can be derived from the JMI estimated velocity model according to the following equation, when assuming a constant density distribution (see also Masaya and Verschuur, 2018):

$$R_{constr}(x, y, z_n) \approx \frac{c(x, y, z_n) - c(x, y, z_{n-1})}{c(x, y, z_n) + c(x, y, z_{n-1})}. \tag{3.32}$$

With this in mind we can extend the formulation of the objective function from Equation 3.1 to the following:

$$J = \frac{1}{2}\sum_{k}\sum_{\omega} \parallel \vec{P}^{-}_{obs}(z_0) - \vec{P}^{-}_{mod}(z_0) \parallel^2 + \lambda_2 \parallel R_{JMI}(z_n) - \Gamma R_{constr}(z_n) \parallel^2, \tag{3.33}$$

where Γ is a scaling factor that compensates for neglecting the density distribution in the calculation of R_{constr} and λ_2 is a weight factor to balance the contributions of the two terms in the Equation 3.33 (Masaya and Verschuur, 2018). Note that the gradient from the second term will affect only the update of the velocity model and can be calculated as follows:

$$\nabla J_{2,c}(z_n) = \lambda_2 \int (R_{JMI}(z_n) - \Gamma R_{constr}(z_n))dz. \tag{3.34}$$

In order to ensure that the low wavenumbers contribution is still provided only by the seismic data, which is controlled by the first term in Equation 3.33, a low-cut filter could be applied to the gradient from Equation 3.34. Note that $\nabla J_{2,c}(z_n)$ indicates a gradient for the velocity that can easily be translated into a gradient for the slowness via the following equation in a linear approximation:

$$\nabla J_{2,\sigma}(z_n) = \frac{-\nabla J_{2,c}(z_n)}{c_0^2}. \tag{3.35}$$

This new gradient can be added to slowness update $\Delta\sigma$ from Equation 3.29 after applying a scaling factor Λ that fits both contributions to each other in the least-squares sense:

$$\Lambda = argmin\|\Delta\sigma(z_n) - \Lambda\nabla J_{2,\sigma}(z_n)\|^2. \tag{3.36}$$

Note that the effect of this additional gradient will be emphasizing the high wavenumbers contribution and introducing more details into the velocity model update.

3.7 JMI algorithm for 3D BSD

All the described theory so far is valid for all acquisition geometries including the special case of 3D BSD, where the reciprocal sources are positioned in the subsurface. A unique characteristic of 3D borehole data is the availability of the measured direct wavefield that represents the true Green's function at the source position. The direct wavefield can be utilised to calibrate the source

wavelet but more importantly to update the velocity model when combined in one-way tomography with reflection JMI. In practice, the 3D BSD is divided into a data subset without the direct wavefield, which is used in the reflection JMI process, and another data subset where the direct wavefield is isolated. This means that the objective function from Equation 3.33 can be extended with an additional third term that includes the contribution from the direct wavefield for the velocity model update:

$$J = \frac{1}{2}\sum_{k}\sum_{\omega} \parallel \vec{P}^{-}_{obs}(z_0) - \vec{P}^{-}_{mod}(z_0) \parallel^2 + \lambda_2 \parallel R_{JMI}(z_n) - \Gamma R_{constr}(z_n) \parallel^2 + \frac{\lambda_3}{2}\sum_{k}\sum_{\omega} \parallel \vec{P}^{-}_{direct}(z_0) - \vec{P}^{-}_{direct-mod}(z_0) \parallel^2, \tag{3.37}$$

where λ_3 is a weight factor that controls the contribution of the one-way tomography in the JMI process. $\vec{P}^{-}_{direct}(z_0)$ and $\vec{P}^{-}_{direct-mod}(z_0)$ are the measured and modelled directed wavefields, respectively. The first term in Equation 3.37 uses data without the direct wavefield $\vec{P}^{-}_{obs}(z_0)$ and is utilized to update the reflectivity and the velocity model using reflected energy. The third term uses the data misfit between the measured and modelled direct wavefield and its gradient for the slowness can be calculated as follows:

$$\nabla J_{3,\sigma}(z_n) = \sum_{\omega} \left[\mathbf{G}(z_n, z_{n+1})\right]^H \frac{\partial J_3}{\partial \mathbf{W}^{-}(z_n, z_{n+1})}. \tag{3.38}$$

Note that this gradient is utilized in updating the velocity model only for the depth levels above the position of the reciprocal source as can be seen in Figure 3.6. In analogy with the derivation of Equation 3.22 we can calculate the gradient $\frac{\partial J_3}{\partial \mathbf{W}^{-}(z_n, z_{n+1})}$ as follows:

$$\frac{\partial J_3}{\partial \mathbf{W}^{-}(z_n, z_{n+1})} = \sum_{k} \left[\mathbf{V}^{-}(z_0, z_n)\right]^H \left[\vec{P}^{-}_{direct}(z_0) - \vec{P}^{-}_{direct-mod}(z_0)\right] \left[\mathbf{W}^{-}(z_{n+1}, z_{src})\vec{S}^{-}(z_{src})\right]^H. \tag{3.39}$$

Equation 3.39 describes a cross-correlation between the direct forward-modelled upgoing wavefield $\vec{W}^{-}(z_{n+1}, z_{src})\vec{S}^{-}(z_{src})$ and the data misfit backward propagated to depth level z_n with the propagation operator $\mathbf{W}^{-}(z_0, z_n)$ and scaled by $\mathbf{I} - \mathbf{R}(z_n)$. Furthermore, an initial scaling factor α_3 for this additional

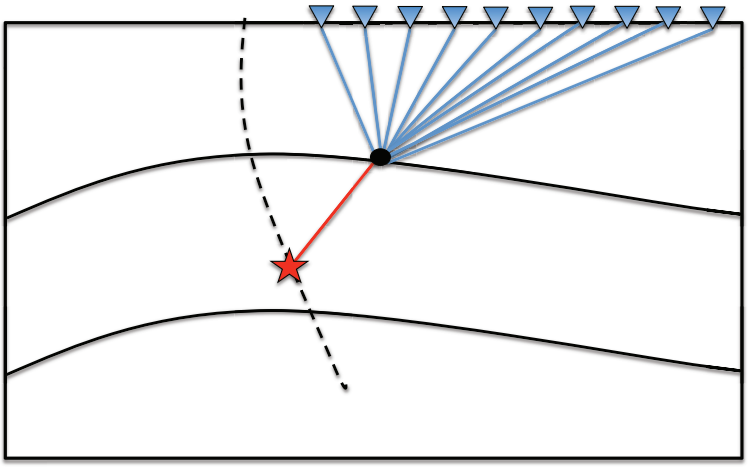

Figure 3.6: Schematic illustration of the calculation of the gradient of the propagation operator based on the measured direct wavefield. The dashed black line indicates the well-trajectory, where the reciprocal sources are positioned. The data misfit, indicated in blue, is back propagated toward every depth level above the position of the reciprocal source and is cross-correlated with the direct upgoing forward-modelled wavefield, that is leaving depth level z_{n+1}, at every lateral location as is indicated by the black dot.

gradient can be calculated as follows:

$$\alpha_3 = \frac{\sum_k \sum_\omega \left(\left[\Delta \vec{P}^-(z_0) \right]^H \vec{E}^-(z_0) \right)}{\sum_k \sum_\omega \left(\left[\Delta \vec{P}^-(z_0) \right]^H \Delta \vec{P}^-(z_0) \right)}, \tag{3.40}$$

where $\vec{E}^-(z_0) = \left[\vec{P}^-_{direct}(z_0) - \vec{P}^-_{direct-mod}(z_0) \right]$ represents the data misfit and $\Delta \vec{P}^-(z_0)$ is the wavefield perturbation that corresponds to the current slowness update $\nabla J_{3,\sigma}(z_n)$ and can be calculated as follows:

$$\Delta \vec{P}^-(z_0) = \sum_{n=1}^{N_{z_{src}}} \mathbf{V}^-(z_0, z_n) \nabla J_{3,\sigma}(z_n) \mathbf{G}^-(z_n, z_{n+1}) \mathbf{W}^-(z_{n+1}, z_{src}) \vec{S}^-(z_{src}). \tag{3.41}$$

The scaled slowness gradient based on the measured direct wavefield, together with the gradient based on the reflectivity constraint from Equation 3.35 are added to the scaled slowness gradient based on reflected energy from equation 3.29 to form the total update of the slowness after which an optimum step-length is determined via a line search procedure. By utilizing all available information in 3D borehole data and the different slowness gradients, as described in this chapter, we have a better chance to overcome the important issue of the non-uniform fold distribution that imposes extra challenges on the JMI algorithm, especially for the velocity model update part. Furthermore, the reflectivity constraint as described in the previous section together with the utilization of prior geological information and available well-logs will help steering the algorithm toward the right solution and will decrease the turnaround time.

3.8 Practical aspects in the JMI algorithm

3.8.1 Anisotropic phase-shift operator

Anisotropy is an important phenomenon in wave propagation that should be taken into account in the imaging process in order to produce accurate results (see e.g. Byun et al., 1989; Lynn et al., 1991). The main cause of anisotropy is the fine layering of the subsurface and the intrinsic preferred orientation of the mineral grains (Banik, 1984). Anisotropy manifests itself in different forms, however in this thesis we restrict ourself to Vertical Transversely Isotropic (VTI) media and we utilize the Fourier finite-difference FFD method as described by Fei and Liner (2008) and Ristow and Ruhl (1994) to account for anisotropic effects. The FFD method can suppress the pseudo S-wave solution that exists in the VTI acoustic wave equation (Alkhalifah, 2000) but is computationally expensive. According to Alkhalifah (2000) the acoustic VTI vertical k_z has the following dispersion relationship:

$$k_z = \frac{\omega}{v_{p0}} \sqrt{1 - \frac{u^2}{1 - 2\eta u^2}}, \tag{3.42}$$

where v_{p0} represents the vertical P-wave velocity, $\eta = (\epsilon - \delta)/(1 + 2\delta)$ is a parameter originally introduced by Alkhalifah and Tsvankin (1995), with ϵ and δ the Thomsen parameters (Thomsen, 1986) and u defined as follows:

$$u^2 = \frac{(k_x^2 + k_y^2) v_n^2}{\omega^2}, \tag{3.43}$$

with $v_n = v_{p0}\sqrt{1+2\delta}$ is the NMO velocity as defined by Thomsen (1986). The FFD algorithm is derived by adding and subtracting the isotropic wavenumber from the anisotropic wavenumber as defined in Equation 3.42:

$$\begin{aligned} k_z = &\frac{\omega}{c}\sqrt{1-\frac{c^2}{v_n^2}u^2} \\ &+\frac{\omega}{v_{p0}}\sqrt{1-\frac{u^2}{1-2\eta u^2}}-\frac{\omega}{c}\sqrt{1-\frac{c^2}{v_n^2}u^2}, \end{aligned} \tag{3.44}$$

where c is a reference velocity typically chosen as the minimum vertical wave velocity. The first term in Equation 3.44 is the isotropic phase-shift contribution and the second term represents the correction for anisotropy. Considering only the second-order operator in the infinite series of the Taylor expansion of the second term in Equation 3.44 yields:

$$\begin{aligned} k_z \approx &\frac{\omega}{c}\sqrt{1-\frac{c^2}{v_n^2}u^2}+\frac{\omega}{c}(p_0-1) \\ &+\frac{\omega}{c}\left[p_n^2\left(\frac{u^2}{A_1-B_1u^2}\right)-p_0\left(\frac{u^2}{a_1-b_1u^2}\right)\right], \end{aligned} \tag{3.45}$$

where $p_0 = c/v_{p0}$ and $p_n = c/v_n$. The coefficients (a_1, b_1) and (A_1, B_1) are defined as follows:

$$\begin{aligned} a_1 &= 2 \qquad b_1 = \frac{1}{2}(8\eta+1) \\ A_1 &= 2 \qquad B_1 = \frac{1}{2}p_n^2. \end{aligned}$$

For the complete series expansion of Equation 3.44 the reader is referred to Fei and Liner (2008). Note that in this thesis we only invert for the vertical slowness, which is related to v_{p0} and we assume that the anisotropy parameters ϵ and δ are known. This means that during the JMI process the anisotropy parameters are fixed and included in the propagation operator in the forward modelling as well as in the gradient calculation for the reflectivity and the velocity model. For a more comprehensive and detailed work where the JMI algorithm is used to invert for anisotropy as well, the reader is referred to Alshuhail (2017).

3.8.2 Quality factor compensation

The JMI algorithm is a true-amplitude inversion scheme where the modelled data is continuously compared to the observed measurements. This means

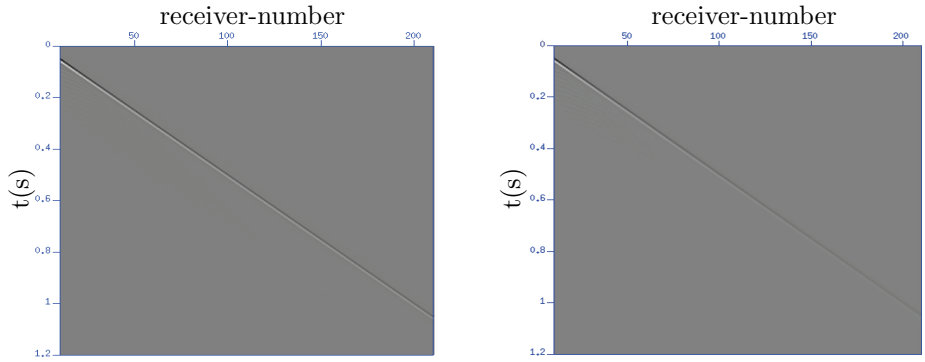

Figure 3.7: Comparison between seismic modelling with and without absorption effects of the direct wavefield of a zero-offset VSP in a simple synthetic model. a) Direct wavefield modelled without absorption effects. b) Direct wavefield modelled with absorption effects by taking $Q = 100$. Note the decay of the seismic amplitude in the right panel as a function of the receivers-depth, which increases with increasing receiver-number.

that effects like intrinsic absorption that causes frequency-dependent amplitude attenuation, as illustrated in Figure 3.7, should be included in the forward modelling part of the JMI algorithm. This will make the total upgoing wavefield at the surface $\vec{P}^{-}_{mod}(z_0)$, from Equation 3.1, more consistent with the observed data $\vec{P}^{-}_{obs}(z_0)$. Like anisotropy in the previous section, we assume that a profile for the quality factor $Q(z)$ is known and we take that into account, e.g. based on the spectral ratio method (see e.g. Futterman, 1962; Haase and Stewart, 2003). In the forward modelling, we multiply the downgoing and upgoing wavefields $\tilde{P}^{\pm}(k_x, k_y, z, \omega)$ after each forward propagation step over Δz in the frequency-wavenumber domain (k_x, k_y, ω) with the Q filter as follows:

$$\tilde{P}^{\pm}(k_x, k_y, z, \omega) = \tilde{P}^{\pm}(k_x, k_y, z, \omega) e^{-\omega \Delta z / (2Q(z) v_{p0})}, \tag{3.46}$$

where Δz is the vertical grid-size of the imaging model and v_{p0} is the vertical P-wave velocity. Note that in the gradient calculation part for both the reflectivity and the velocity model, the inverse of this Q filter, defined as $e^{\omega \Delta z / (2Q(z) v_{p0})}$, should be applied to the back propagated residual data in combination with the application of the forward Q filter to the forward modelled data $\tilde{P}^{+}(k_x, k_y, z, \omega)$ as described in Equation 3.46. It is expected that this will enhance the amplitude spectrum of the modelled data w.r.t.

the observed measurements and consequently the estimated solutions of the JMI algorithm.

3.9 Discussion

In this chapter we have discussed the 3D JMI algorithm, which is a non-linear inversion scheme where the seismic data is parametrized in terms of subsurface reflectivity and propagation operators. These two parameters are assumed to be independent of each other in order to stabilize the inversion process and avoid being trapped into a local minima. However, once the estimated velocity model is adequate enough the reflectivity and propagation operator can be linked together via an additional reflectivity-constraint in the objective function. This will introduce more details in the estimated velocity model and speed up the convergence process. The JMI propagation operators are one-way phase-shift operators where additional wave-phenomena effects like anisotropy and frequency-dependent amplitude attenuation can easily be implemented. However, a more general description for anisotropy, without the limitations of any pre-assumed parametrization of the subsurface anisotropy type, can be realised by considering the angle-dependent slowness parameter and inverting for it similar to the angle-dependent reflectivity operator. Furthermore, as can be seen from Equation 3.22 and 3.25, it is envisioned that it could be possible to invert directly for the propagation operator $\mathbf{W}$ in a completely data-driven manner without any prior parametrization for the propagation operator (Berkhout, 2014c). Note that this generalized propagation operator will implicitly include all wave-phenomena effects like anisotropy and absorption.

4

3D FWM and JMI applications for borehole and surface seismic data

Surface-related and internal multiples enhance the illumination of the subsurface and enable us to image areas that are beyond the coverage of primary reflections, especially in the case of marine environment and datasets with a sparse acquisition geometry like 3D BSDor OBN seismic data. In addition, shadow zones and acquisition geometry footprints, which we also encounter in 3D surface seismic, can be overcome by including the multiple scattering in the imaging process. In conventional imaging, it is first attempted to linearise the input data by suppressing the surface-related multiples, and ignoring the internal multiples, to make it suitable for linear migration algorithms and the associated velocity models are updated accordingly. However, it has been demonstrated that the non-linearity in the data adds extra sensitivity to erroneous propagation operators (Berkhout et al., 2015). This unique property puts additional constraints to the possible solutions of the velocity model and will help expediting and steering the inversion algorithms toward more reliable estimates. Furthermore, non-linear migration algorithms like the FWM and JMI algorithms must have a closed-loop architecture, as explained in Chapter 3. This is mainly to ensure consistency between the input data and the estimated model parameters (Berkhout, 2014b). In this chapter we will demonstrate the contribution of the downgoing wavefield of the 3D

BSD to the illumination of the subsurface and the added value of surface-related multiples, in general, in the case of datasets with sparse acquisition geometry. Furthermore, the capability of the 3D JMI algorithm to simultaneously estimate the subsurface reflectivity image and its corresponding propagation velocity model is shown. This will be done for surface seismic and 3D borehole-related data.

4.1 Introduction

It is well-known that BSD measurements have unique properties compared to surface seismic data (Hardage, 1985). Some main aspects are the access to upgoing and downgoing wavefields and the shorter travel path of the seismic waves, yielding less amplitude loss, especially at the high frequencies. The latter is amplified by the fact that the unconsolidated near surface is traversed only once. However, the conventional BSD images suffer from the limited lateral extent as a result of the non-uniform fold distribution especially when only primaries are utilized (Blias and Hughes, 2015). Moreover, the downgoing wavefield, in 3D BSD, is usually neglected and removed prior to the imaging process.

In addition, multiples have long been considered as noise, which means that a lot of extra subsurface illumination by multiples has been neglected for a long time. Only in the last decade the ideas of using multiples in the imaging scheme have been materialized, although there were some early attempts (e.g. Berkhout and Verschuur, 1994). This topic is revisited by Whitmore et al. (2010), Verschuur and Berkhout (2011) and Lu et al. (2011). Using multiples in the imaging process will lead to more reliable model parameters estimates. However, the involved cross-talk needs to be resolved in the migration process. This can be done via a least-squares inversion approach, as shown by Zhang and Schuster (2014). Also, the use of internal multiples needs to be incorporated. The latter has been carried out by Malcolm et al. (2009), who used the imaged reflection coefficient to build an illumination by first-order internal multiples. Berkhout (2012) generalized all the above approaches by the concept of Full Wavefield Migration (FWM), as is explained in Chapter 3, where all multiples – surface and internal – are considered as part of the illuminating wavefield and where a full waveform inversion approach, based on a two-way integral formulation of the scattered data, is used to find reflectivities such that the measured data is fully explained. In this way multiples do not wrongly map in the image and, in addition, they can contribute to the illumination of areas not well covered by primaries. FWM was described in

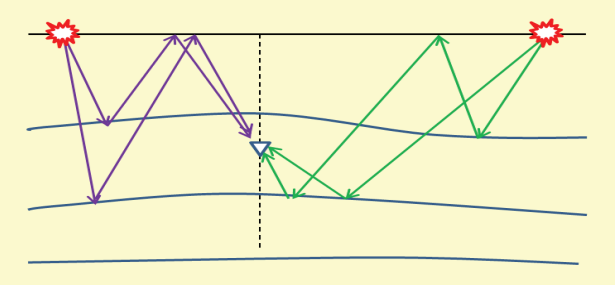

Figure 4.1: Schematic overview of upgoing (green) and downgoing (purple) wavefields for 3D BSD.

more detail by Davydenko and Verschuur (2013) and Berkhout (2014b) and applied to 3D BSD by El Marhfoul and Verschuur (2014).

In addition, as was explained in Chapter 3, the propagation velocity model can also be updated simultaneously, yielding the so-called Joint Migration Inversion (JMI) algorithm (Berkhout (2012); Staal and Verschuur (2013); Berkhout (2014a,b,c)). Its main feature is the decoupling of the propagation operators that describe the kinematics from the scattering operators that affect the amplitudes in the seismic data. Like FWM, it is an iterative process, where the modelled data is constructed in a recursive manner and continuously compared with the measured input data. The residue is then translated into an update of both the reflectivity and velocity model. All multiples - surface and internal - are considered as part of the illuminating wavefield and, thus, are used to find reflectivity and propagation operators such that the measured data is fully explained. In this way multiples do not wrongly map in the image but will even contribute in the illumination of areas not well covered by primaries. This decoupling of the parameters provides a less non-linear inversion method (Verschuur et al., 2016) and, thereby, circumvents some of the non-linear issues related to traditional full waveform inversion (see e.g. Virieux and Operto, 2009).

4.2 3D FWM of up- and down-going BSD wavefields

The downgoing wavefield in the 3D BSD (see the purple lines in Figure 4.1) can be considered as multiple scattering and will add to the illumination of the subsurface. In this section we will illustrate the added value of the

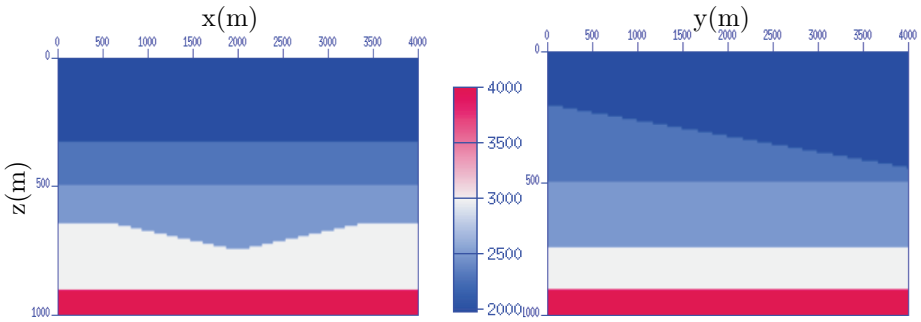

Figure 4.2: Tow perpendicular cross-sections, from the 3D velocity model, at the well location. Note that the well location is at $x = 2000, y = 2000$ *and the sources are positioned in the borehole starting from* $z = 120m$ *up to* $z = 720m$ *with* $\Delta z = 40m$.

downgoing wavefield in the 3D BSD when the FWM technology, as described in the previous chapter and the preceding section, is deployed. The synthetic model depicted in Figure 4.2 is utilized to model 3D BSD. It can be observed that the 3D model has a few dipping and flat reflectors in both the x- and y-directions. The true reflectivity model, which is derived from the 3D velocity model and a constant density distribution, is used to model 3D BSD. We have used reciprocity, meaning that for the modelling and the imaging process the sources are assumed in the well, while the receivers were located at the surface. The modelling was carried out using the FWMod algorithm, which is based on one-way wave propagators and scalar reflectivities (see Berkhout (2014a) and the description in Chapter 2). The receiver grid was chosen to be uniform over the whole model with $\Delta x = \Delta y = 20m$. The well location was set at the center of the model. The 3D BSD was modelled for sixteen levels with elevation starting from $z = 120m$ up to $z = 720m$ with $\Delta z = 40m$. Figure 4.3 shows zero-offset VSP data for both up- and downgoing wavefields. Primary reflections and multiple scattering from several reflectors can be seen in the zero-offset shot gather.

In Figure 4.4 the results of the FWM using the modelled 3D BSD are displayed. The image in Figure 4.4b represents the conventional image from regular pre-stack depth migration. The image in Figure 4.4c represents the output after ten iterations of FWM using only the upgoing wavefield. Figure 4.4d displays the result of the FWM using only the downgoing wavefield. Note the strong influence of the BSD primaries in the conventional image, which is understood from the fact that these sources are close to the reflector. However, after only ten iterations of FWM, a largely improved consistency

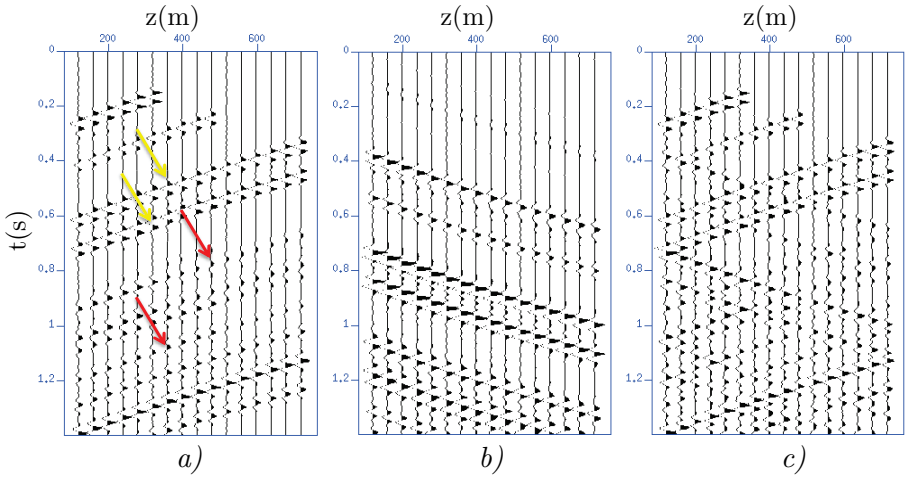

Figure 4.3: Zero-offset VSP data. a) Upgoing wavefield. b) Downgoing wavefield. c) Total wavefield. The yellow arrows are indicating primaries and the red arrows are indicating multiples.

and a better resolution of the reflectivity of the events across the whole imaging area can be observed. This is mainly due to the closed-loop approach of FWM and the fact that the obtained reflectivity has to explain primaries and all multiple scattering. Comparing Figures 4.4c and 4.4d shows that the downgoing wavefield, measured in the 3D BSD, provides an additional contribution to the final image that is equal to the one from the upgoing wavefield, and therefore it should not be neglected.

4.3 3D JMI example: the added value of surface-related multiples

In this section we will illustrate the JMI technology as described in the previous chapter for the 3D model depicted in Figure 4.5. It is a homogeneous model containing a low-velocity channel embedded in a relatively high-velocity layer. For the sake of illustration, the true reflectivity model is not derived from the true velocity model but is assumed to consist of only three horizontal reflectors and is displayed in Figure 4.6a. 3D surface seismic data was modelled, according to the coarse source configuration as displayed in Figure 4.5a, with the receivers densely sampled over the complete areal extent of the model according to an uniform grid with $\Delta x = \Delta y = 20m$. The modelling was carried out using the FWMod algorithm based on one-way

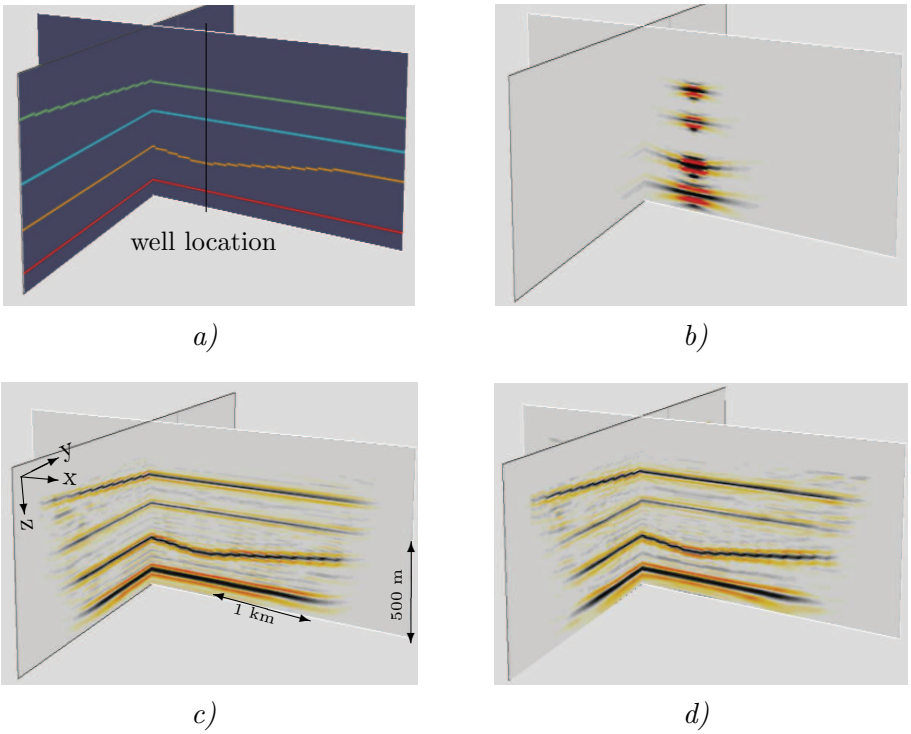

Figure 4.4: 3D reflectivity image cubes. a) The true reflectivity image with the well location indicated by the black line. b) The reflectivity image from regular pre-stack depth migration (equivalent to the first FWM iteration). c) The result of FWM of up-going 3D BSD wavefield. d) The result of FWM of down-going 3D BSD wavefield. Note the consistency and the high resolution of both FWM results from the up- and down-going BSD wavefield.

wave propagation operators and scalar reflectivities and assuming free-surface boundary conditions. In this experiment we assume that the migration velocities are well defined everywhere except in the area around the anomalous layer. Therefore, during the JMI process we allow velocity updates only within that specific layer. Figure 4.5c,d show the results of the JMI algorithm for the estimated velocity model, where the full wavefield (primaries and multiples) is deployed in the inversion process. In spite of the sparse acquisition geometry, the 3D JMI algorithm was able to delineate the horizontal channel present in the true velocity model. This is mainly because the multiple scattering is reinforcing the primary energy during the inversion process. Figure 4.6 displays a vertical cross-section from the 3D reflectivity

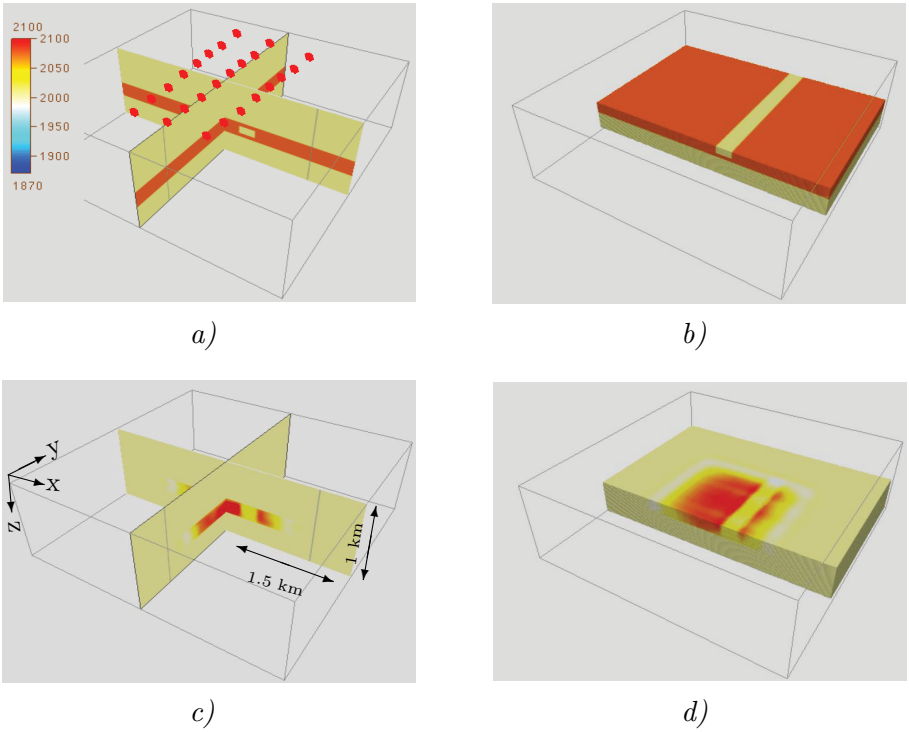

Figure 4.5: The 3D true and the JMI estimated velocity models. a) The true velocity model with the sparse acquisition geometry. b) 3D view of the true velocity model. c) The JMI estimated velocity model with the same view as a). d) The estimated JMI velocity model with the same view as b). Note that the starting velocity model is homogeneous with $v = 2000m/s$. The JMI algorithm is able to update the migration velocity model and adequately delineate the horizontal channel.

cube estimated by the JMI algorithm compared with the image from regular PSDM process using the initial velocity model and primary reflections only. Note the higher resolution in the image, when 3D JMI is deployed and the correct vertical positioning of the three horizontal reflectors. This is mainly due to the closed-loop architecture of the JMI algorithm and the fact that the estimated parameters (propagation velocity model and reflectivity model) have to explain primaries and all multiple scattering present in the input dataset.

In addition, to even further clarify and demonstrate the added value of the multiple scattering in the JMI process, another experiment is conducted

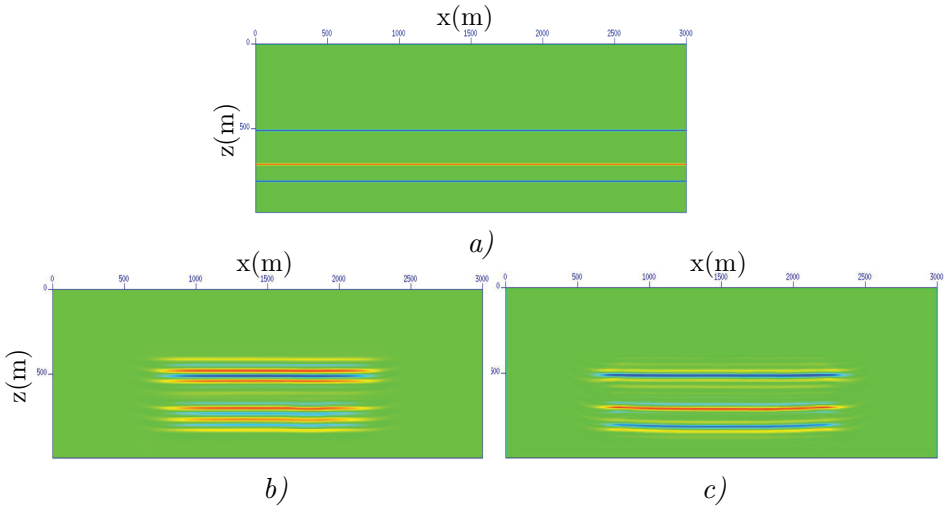

Figure 4.6: Cross-section from the 3D estimated reflectivity image cube using the JMI algorithm. a) The true reflectivity image. b) The conventional PSDM image. c) The estimated JMI reflectivity image. Note the high resolution and the right vertical positioning of the horizontal reflectors.

where only primary reflections from the same dataset are utilised as input to the JMI inversion algorithm. Figure 4.7 shows a cross-section from the 3D estimated velocity model, after the same number of iterations as when the full wavefield (including the multiple scattering) is used. It can be noticed that the estimate of the velocity model, by including the multiples in the JMI process, is converging to the true solution in a much faster and consistent manner. Note again that in this example we allowed velocity updates only in the area around the low-velocity channel. Figure 4.8 shows the same cross-section as in Figure 4.7 from the estimated reflectivity model. By including the multiples in the JMI process better estimates of the velocity and reflectivity models are obtained.

4.4 JMI strategy for 3D borehole seismic data

4.4.1 Strategy for the estimation of the source-wavelet

The JMI algorithm has the flexibility to consider only a certain reflection mode, like surface-related multiples, and update the model parameters – reflectivity and migration velocity model – accordingly. This means that in the

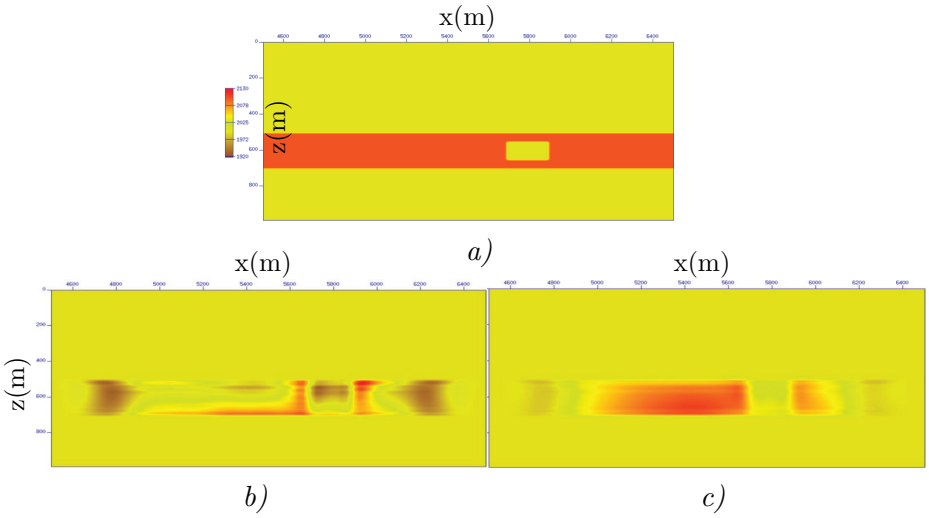

Figure 4.7: Cross-section from the 3D JMI estimated velocity model. a) The true velocity model. b) Result by deploying only primary reflections in the JMI process. c) Result by including the multiple scattering in the JMI process.

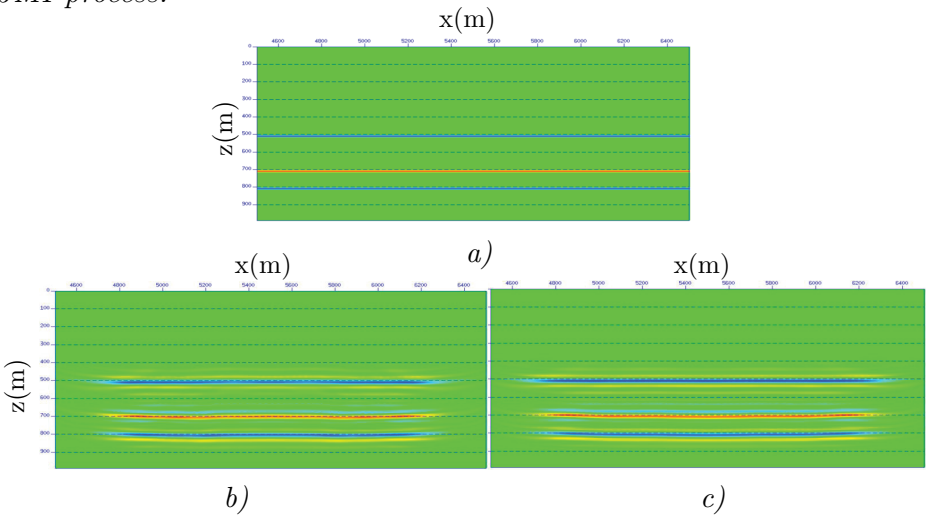

Figure 4.8: cross-section from the 3D JMI estimated reflectivity image. a) The true reflectivity image. b) Result by deploying only primary reflections in the JMI process. c) Result by including the multiple scattering in the JMI process.

case of unknown source-wavelet only surface-related multiples should be deployed to update, at least, the shallow part of the migration velocity model. This process is purely data-driven and independent of the source-wavelet, which is then needed for the imaging of the primary reflections and internal multiples. Once a reasonable update of the shallow part of the migration velocity model is achieved, the direct wavefield from a selected common receiver gather is then focused into its corresponding depth-position to estimate a 3D source wavefield. Note that the update of the migration velocity model based on the surface-related multiples will affect mostly the first few hundred meters of the subsurface (depending on the length of the recording tool in the borehole) and therefore it is preferred to choose the shallowest common receiver gather to estimate one unified source wavefield.

It is also possible to have a source wavefield for every common receiver gather, as long as we ensure general consistency in terms of amplitude and phase over all estimated source wavefields. Note that this process does not necessarily lead to a better solution for the migration velocity model and reflectivity image mainly because of the requirement of an accurate migration velocity model for the focusing of the direct wavefield.

Finally, additional calibration of the estimated source wavefield might be necessary. This is achieved by running few iterations of a least-squares inversion imaging process where we assume only primary reflections in the input data to produce an estimate for the reflectivity image and ensure amplitude consistency with the estimate when only surface-multiples are deployed.

In conclusion, the source wavefield estimation procedure can be summarized as follows:

- Deploying only the surface-related multiples in updating of the shallow part of the migration velocity model.
- Focusing of the direct wavefield from the shallowest common receiver gather into its corresponding depth-position.
- Additional calibration of the estimated source wavefield by ensuring amplitude consistency between the reflectivity image based on the surface-related multiples and the one obtained by assuming primary reflections only.

The primary reflections and the internal multiples will then be engaged together with the surface-related multiples in one full wavefield JMI process

to invert for the reflectivity image and the migration velocity model. It is advisable to repeat the process of the source wavefield estimation during the JMI process each time we have a substantial update in the migration velocity model. Note that the source wavefield estimation process becomes much simpler and more accurate when dealing, for example, with OBN data due to the well defined migration velocities of the water column.

In the case of field surface seismic data, where we don't have access to the direct wavefield, the current velocity model is used to produce an estimate for the reflectivity image based on surface-related multiples only. Next, a backward propagation process of the measured data toward every depth level z_n in the subsurface is applied where we multiply with the estimate of the reflectivity image, from the surface-related multiples, at that particular depth level z_n followed by a backward propagation process toward the source position at the surface level z_0. This will focus the energy from the primary reflections into the source position (Davydenko, 2016). Finally, in order to isolate only the energy that belongs to the source wavefield, some muting in the spatial and temporal directions must be applied based on the prior knowledge available about the used source-wavelet. This procedure can be summarized as follows:

- Deploying only the surface-related multiples with the current migration velocity model to produce an estimate for the reflectivity image.
- Backward propagation of the measured data into the subsurface and multiplying by the reflectivity image at every depth level z_n then backward propagation toward the source position at the surface z_0.
- Muting in the spatial and temporal direction to remove all events that are not focused at the source position.
- Additional calibration of the estimated source wavefield by ensuring amplitude consistency between the reflectivity image based on the surface-related multiples and the one obtained by assuming primary reflections only.

A major advantage of borehole-related data is the availability of the direct wavefield, which is used to estimate the source wavefield and also allows us to combine one-way tomography of the direct wavefield with reflection JMI of all orders of scattering simultaneously in order to update the velocity model and therefore have a more consistent and reliable solution for the migration velocity model. This could also be seen as a similar process to combining the inversion of diving waves using Full Waveform Inversion with reflection

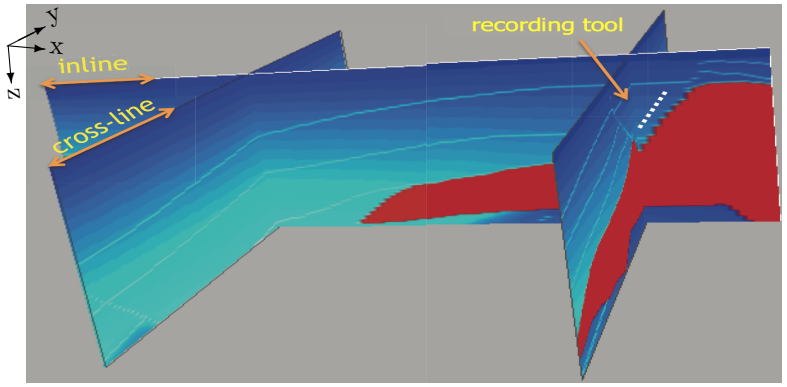

Figure 4.9: The true velocity model with the deviated well trajectory. The recording tool covers a total length of 1200m.

energy modes by deploying the JMI algorithm (Davydenko and Verschuur (2019); Eisenberg et al. (2019)).

4.4.2 3D numerical example

The sparse acquisition geometry of borehole data will result in non-uniform fold distribution of the imaging grid points, even when the multiple scattering is included. Therefore, the reflectivity image should be used as additional constraint to guide and steer the update of the velocity model toward a more

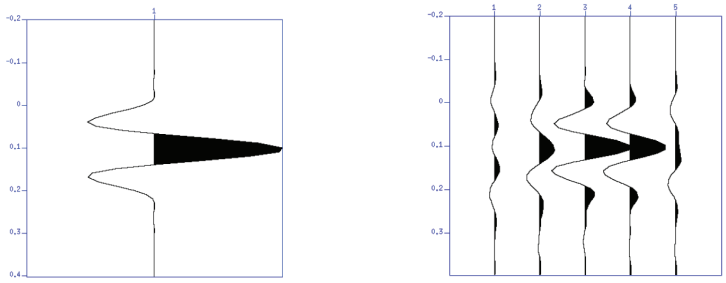

Figure 4.10: The true wavelet (left figure) compared to the JMI estimated source wavefield. Note that the lateral energy spreading is mainly because of the spatial band limitation. In addition the original source is located between two grid-points of the imaging grid that was used in the JMI process, which had a larger grid size than the original grid that was used in finite difference modelling.

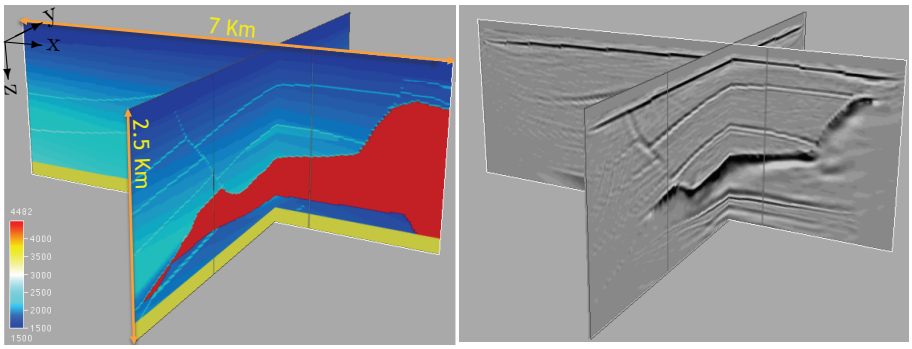

a) b)

Figure 4.11: 3D FWM results. a) The true velocity model. b) The FWM estimated reflectivity image. Note the high resolution of the FWM image and the consistency with the true velocity model.

reliable solution (see Masaya and Verschuur (2018) and the description in Chapter 3). The latter allows us also to delineate high-contrast velocity variations in environments with complex geology like what we encounter in areas with salt structures. This will be illustrated in this section together with the strategy for the source-wavelet estimation, as described in the preceding section, for the SEG salt model. The dataset was modelled with a 3D acoustic finite differences code by using a zero-phase Ricker wavelet with peak frequency of $10Hz$. In this example, we have used reciprocity, which means that the sources are placed in the borehole and receivers are at the surface according to a 'carpet-shooting' geometry, with $\Delta x = \Delta y = 20m$. The well was placed along the salt flank with lateral deviation of $300m$ in both directions. The acquisition tool covers a total depth interval of $1200m$ starting from $z = 300m$ and depth steps of $40m$. Figure 4.9, shows a 3D view of the acquisition geometry. The starting velocity model is a smooth 1D model without any prior salt information. First, the surface-related multiples are used to update the shallow part of the model after which the direct wavefield, from the shallowest shot gather, is focused at the source depth to estimate the source wavefield. Figure 4.10, displays a comparison between the estimated source wavefield and the true source-wavelet. Note that due to the spatial band limitation the estimated source wavefield will spread out over a certain area. Moreover, the original source is located between two grid-points of the imaging grid that was used in the JMI process, which had a larger grid size than the original one that was used in finite difference modelling. As a benchmarking, in Figure 4.11 the FWM image from the 3D BSD is depicted,

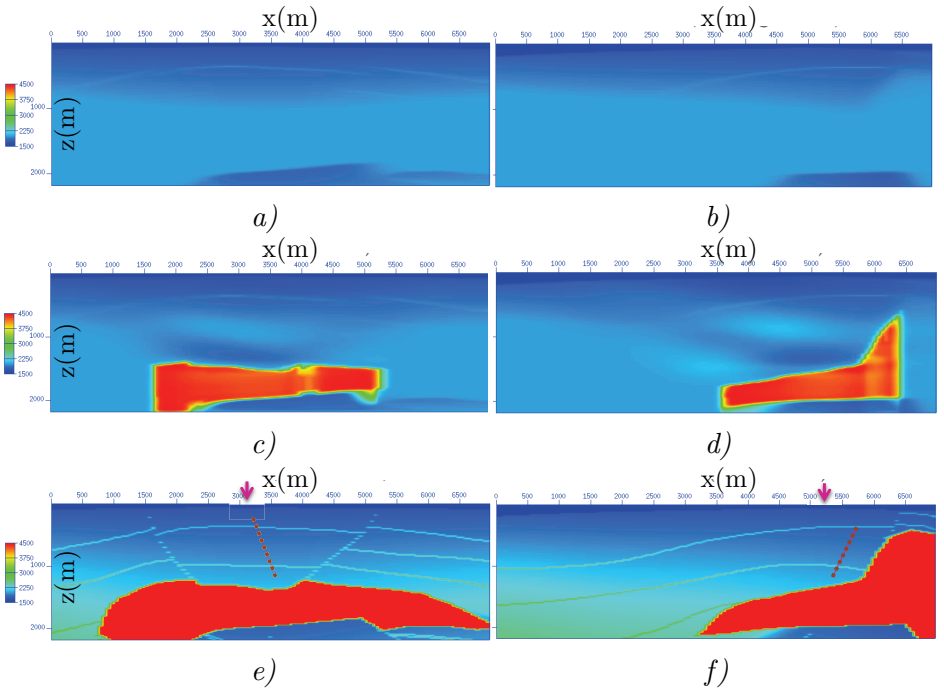

Figure 4.12: Results of the 3D JMI process. a) Cross-line section from the starting velocity model. b) Inline section from the starting velocity model. c) Cross-line section from the JMI estimated velocity model. d) Inline section from the JMI estimated velocity model. e) Cross-line section from the true velocity model. f) Inline section from the true velocity model. The brown dashed line indicates the well trajectory and the arrows indicate the location where the two sections are crossing each other.

for which a smoothed version of the true velocity model is utilized. Note the high resolution and the maximised lateral extent of the image especially at the shallow part of the model.

Even with the sparse acquisition geometry of the 3D BSD, the JMI process results, depicted in Figure 4.12, show a remarkable update of the migration velocity model. The obtained velocity update is consistent with the true velocity model and follows the imposed reflectivity constraint, as explained in Chapter 3, in delineating the salt body. Note that in this case we have also imposed an additional penalty function on the velocity update within the volume that is enclosed by the salt structure. The implemented penalty function is just a simple scaling factor, applied to the velocity gradient during

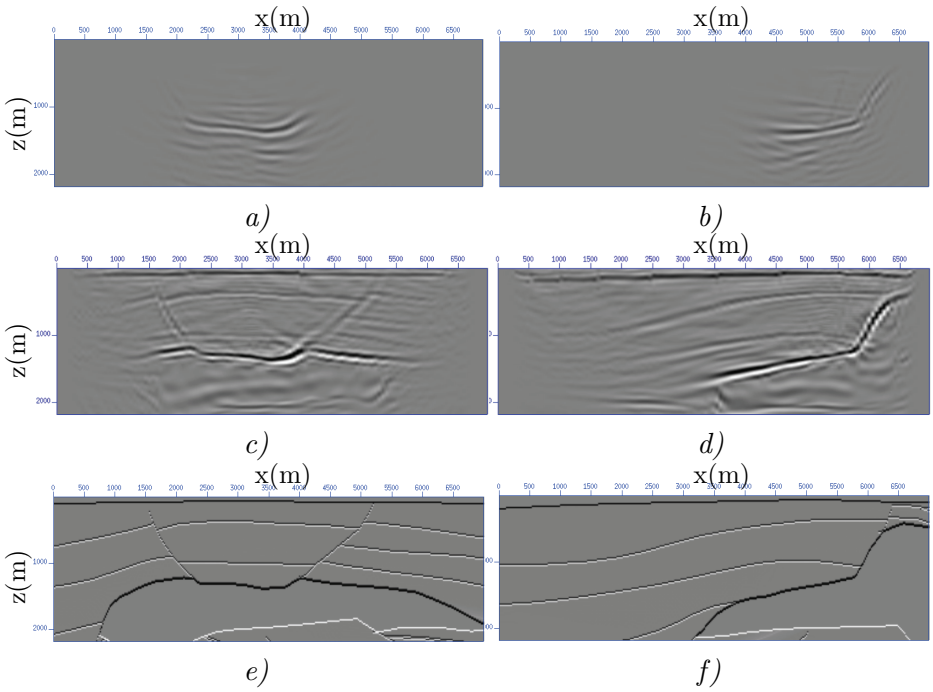

Figure 4.13: The 3D JMI estimated reflectivity image. a) Cross-line section from the PSDM image. b) Inline section from the PSDM image. c) Cross-line section from the JMI estimated reflectivity image. d) Inline section from the JMI estimated reflectivity image. e) Cross-line section from the true reflectivity image. f) Inline section from the true reflectivity image. Note the high resolution and maximum lateral extent in the JMI estimated image.

the first few iterations, that depends on the direction of the velocity gradient within the volume that is determined by the salt structure. This means that the scaling factor is made large if the velocity gradient is positive, indicating increasing migration velocities, and if the gradient is negative within the salt structure then the scaling factor should be small. This process is similar to the automated salt-flooding technique that can be utilized in this kind of geological scenarios (Kalita et al., 2019). Figure 4.13, shows the reflectivity image from the first iteration, which is equivalent to the conventional PSDM image, and the JMI updated reflectivity image. Note the limited lateral extent and lack of resolution in the PSDM image. The JMI reflectivity image shows significant increase of the lateral extent of the imaging area, mainly because of the contribution of the higher-order scattering. In addition, the resolution is improved due to the closed-loop approach of the JMI process,

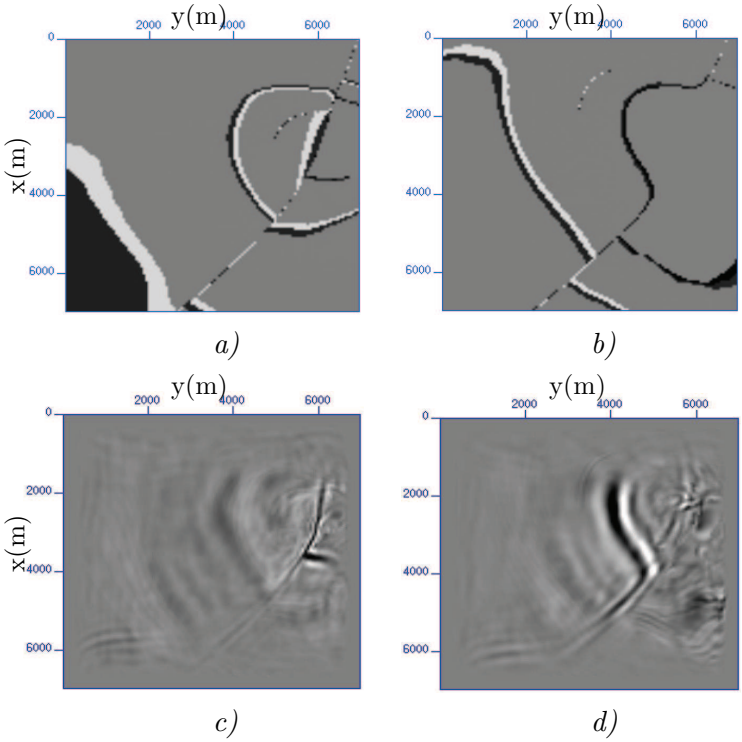

Figure 4.14: Depth slices from the true and the JMI estimated reflectivity image. a) Depth slice at $z = 1200m$ from the true reflectivity image. b) Depth slice at $z = 1600m$ from the true reflectivity image. c) Depth slice at $z = 1200m$ from the JMI estimated reflectivity image. d) Depth slice at $z = 1600m$ from the JMI estimated reflectivity image. Note the consistency of the JMI results with the true model.

even though the maximum used frequency in the JMI inversion process was restricted to $15Hz$ because of computational power and time limitations. Figure 4.14, shows depth slices from the true and JMI reflectivity cubes at two different depths. Note the adequate delineation of the salt flank in the JMI reflectivity model. This is mainly due to the accurate velocity estimation, which is supported by the sensitivity of the JMI algorithm to the high angles available in the 3D borehole data.

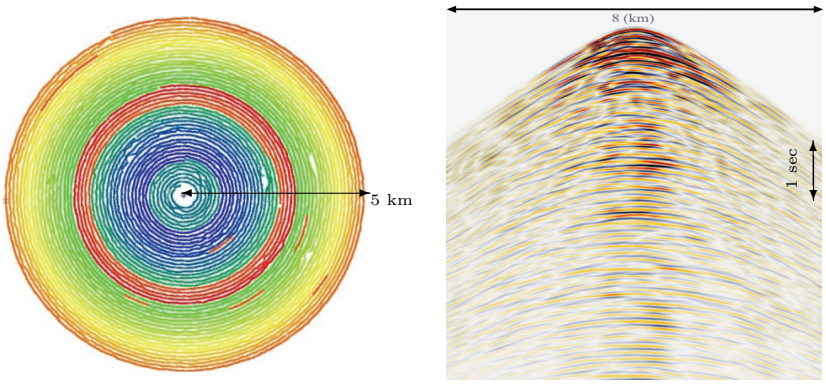

a) *b)*

Figure 4.15: 3D BSD acquisition geometry with a cross-section from the 3D BSD. a) The spiral acquisition geometry of the 3D BSD. The first shot is located at approximately $300m$ *from the well and the total shot radius is* $5km$*. The shot spacing is* $25m$ *and the distance between the spiral source rings is* $100m$*. b) A selected cross-section from a 3D reconstructed BSD common receiver gather.*

4.5 3D BSD field data example

In this section, we will demonstrate the application of the JMI algorithm to the 3D BSD field data. The dataset was acquired in the Arabian Gulf and the main objective was to produce higher-resolution images around the borehole to delineate thin sand stringer, not only in the immediate vicinity of the borehole but also away from it to optimize the placement of multi lateral horizontal wells (Al Bannagi et al., 2018). The survey was acquired in a spiral shooting geometry configuration with minimum radial source offset of 300 m, maximum radial source offset of 5 km, source ring spacing of 100 m and source spacing of 25 m (Figure 4.15). The recording tool in the borehole consisted of around 100 receivers spaced at $15m$. The 3D BSD was processed using a customized and simplified processing workflow to preserve the multiples available in the data. The main processing steps include horizontal tool rotation, elastic wavefield separation to suppress converted waves, and noise-removal. Figure 4.16 shows the processed PP data after regularization to a dense well-sampled spatial grid of $25m$ using a sparse Radon reconstruction algorithm to fill in the acquisition gaps as illustrated in Figure 4.15. Figure 4.16a shows a 3D view of the starting velocity earth model which is based on a smooth 1D checkshot velocity profile at the borehole location. Figure

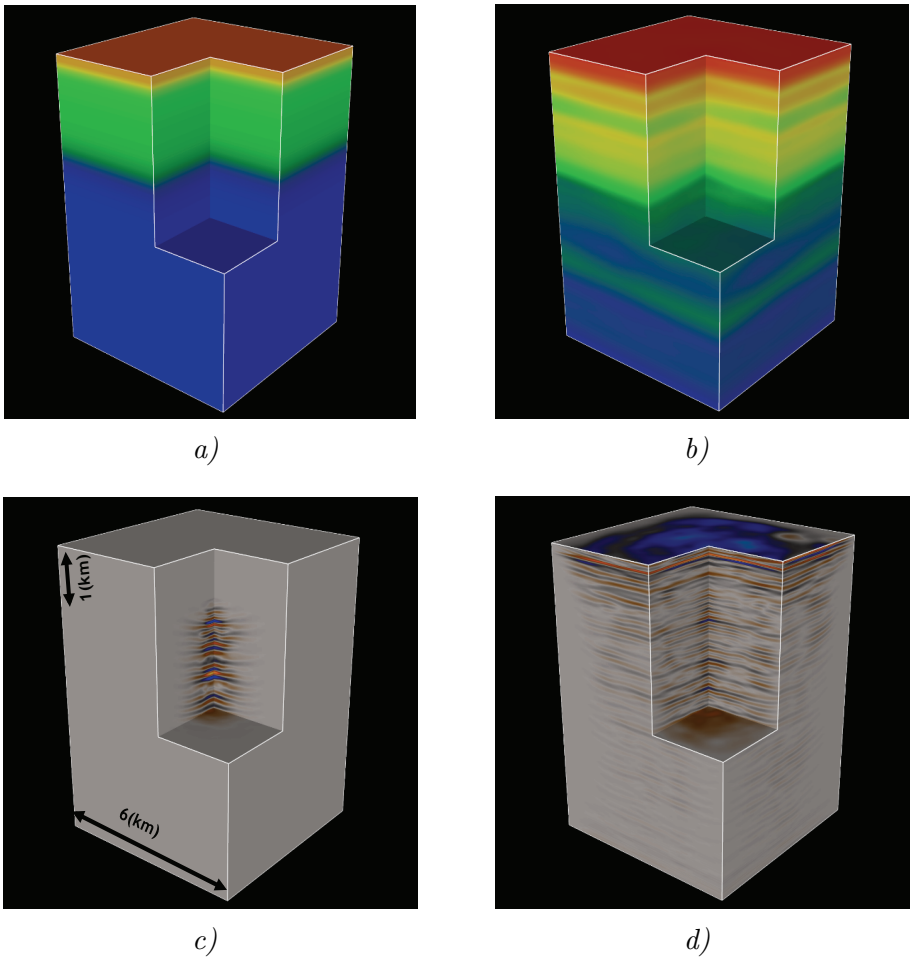

Figure 4.16: 3D JMI estimate of velocity model and reflectivity image cubes. a) The starting velocity model based on a smooth 1D checkshot velocity profile at the borehole location. b) The JMI estimated velocity model. Note the significant and lateral consistent update along the horizons. c) The reflectivity image from conventional pre-stack depth migration using the final JMI velocity model. d) The JMI estimated reflectivity image using the full BSD wavefield. Note the maximized lateral extent of the reflectors up to 4km around the borehole and the high resolution compared to the PSDM image.

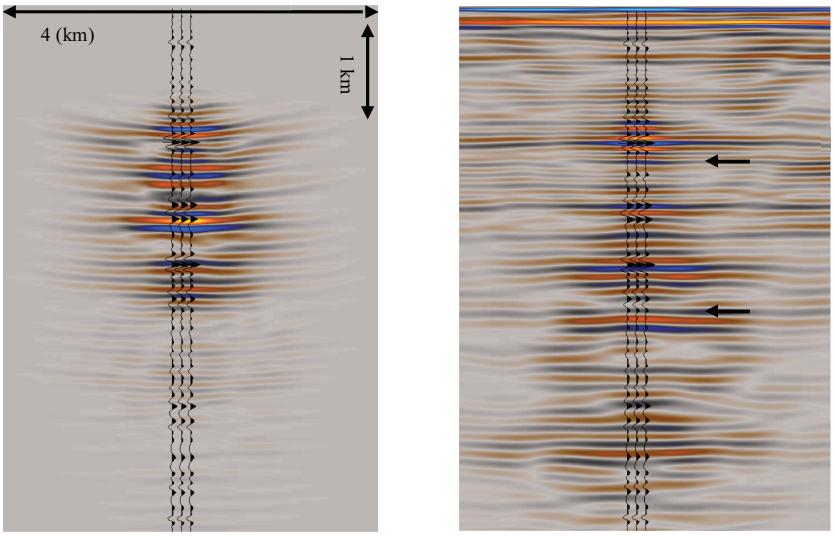

a) *b)*

Figure 4.17: The zero-offset VSP corridor stack spliced, at the well location, in the conventional and the JMI estimated reflectivity image. a) The conventional PSDM cross-section. b) The JMI estimated reflectivity image.

4.16b shows the JMI final updated velocity earth model where it shows a significant update, which is consistent with the imposed lateral smoothness constraint supported by the prior knowledge of geology in the area that follows mainly the 'layered-cake' scenario of the subsurface with a very gentle dip in one direction. Therefore, the velocity gradient is heavily smoothed laterally during the JMI process to minimize the effect of the non-uniform fold distribution in the 3D BSD. Figure 4.16c shows the 3D conventional PSPI PSDM image, whereas Figure 4.16d shows the reflectivity image resulting from the 70th iteration of the JMI algorithm. Both images of Figures 4.16c and 4.16d were produced using the JMI final updated velocity model shown in Figure 4.16b. The correlation between the band-pass filtered zero-offset VSP corridor stack, spliced at the borehole location, and the vertical cross-section from the conventional PSDM is shown in Figure 4.17a. Whereas, Figure 4.17b shows the correlation between the VSP corridor stack and the JMI reflectivity vertical cross-section. This VSP-seismic tie is generally good and multiples were mostly mapped into the right location especially at the target reservoir as a result of the closed-loop approach. Note the limited lateral coverage and lack of resolution in the conventional image relying on

primary reflections only. Conversely, the JMI reflectivity image shows substantial increase in the imaging coverage, even at the shallower part of the subsurface, mainly because of the higher-order scattering. Multiple scattering events have a drastic contribution to the final image which is clearly observed in the area above the shallowest receiver defined by the start of the conventional image. The sea floor is nicely imaged as well. Imaging such shallow subsurface cannot be done by conventional algorithms. The image resolution is improved due to the closed loop approach of the JMI algorithm in which the maximum frequency used in this paper was restricted to 20 Hz. Definitely, opening up the maximum frequency limit and increasing the number of iterations shall improve the image resolution further and take into account remaining multiples as the one marked in Figure 4.17b.

4.6 Discussion

In this chapter the potential of the recently developed 3D JMI algorithm is demonstrated using datasets with different types of acquisition geometries like 3D BSD and surface seismic data. Within the JMI framework, it is relatively straightforward to simultaneously invert the full wavefield including all high-order scattering from both up- and downgoing wavefields available in the 3D BSD measurements. In spite of the sparse acquisition geometry, the 3D JMI algorithm is able to provide reliable estimates of both the migration velocity and reflectivity model. This is mainly because the multiple scattering is improving the subsurface illumination and reinforcing the primary energy during the inversion process. Therefore, it adds significant value to the JMI inversion scheme and steers the algorithm towards more reliable solutions. Moreover, prior knowledge, like well logs, check-shot time-to-depth curves and geologic formation tops can be used as valuable constraints to the JMI inversion process, especially when dealing with datasets with sparse acquisition geometry. The 3D data example presented in this chapter shows that 3D BSD data can indeed provide reliable solutions for the reflectivity as well as the velocity model and extend over quite an offset range to provide high-resolution information that will be of great added value for reservoir characterization.

Acknowledgement

The author would like to thank Saudi Arabian Oil Company (Saudi Aramco) for the permission to publish the field data example.

5

Integration and simultaneous imaging of different seismic measurements

3D borehole-related seismic data plays a crucial role at the stage of reservoir development, especially when deployed in a full wavefield inversion algorithm to provide valuable information about the elastic parameters of the subsurface (Owusu et al., 2016). The broader frequency-bandwidth of borehole seismic data and its relatively enhanced signal to noise ratio make it possible to provide high-resolution images around the borehole (Hardage, 1985). This is mainly because of the position of receivers close to the reservoir yielding a shorter travel path hence less amplitude loss, especially at the high-frequencies range (Li et al., 2015). The latter is amplified by the fact that the unconsolidated near surface is traversed only once. On the other hand, 3D surface seismic data has always been the backbone of the oil and gas exploration to obtain general structure images of the subsurface for locating potential prospects and reservoirs at areas of interest. This is mainly due to the large areal extent that it can cover and the extensive illumination it can achieve especially using modern acquisition geometries (Vermeer, 2012). Moreover, utilizing seismic measurements for the accurate characterization of the subsurface geophysical properties and the delineation of complex fault systems are essential for geothermal energy exploration and production (Gao et al., 2021). In addition, seismic data could also be deployed in the deter-

mination of the elasticity modulus and stiffness of the shallow nearsurface for the purpose of the installation of wind turbines. Recently, there have been developments to integrate wind turbines in the seismic method and use them as non-destructive seismic sources for permanent monitoring of the subsurface (Ruigrok et al., 2020).

All of the above mentioned applications and other non-industrial practices indicate the crucial contribution of seismic imaging to produce reliable estimate of the reflectivity image together with the corresponding medium parameters for better understanding and continuous monitoring of the subsurface. Preferably, this should be achieved by minimum investments in terms of data acquirement and preprocessing, which requires more advanced and integrated inversion-imaging algorithms. Therefore, in this chapter we will demonstrate the added value of the simultaneous deployment of different datasets, like 3D BSD with surface seismic data and multi-well 3D BSD data, in one JMI process.

5.1 Introduction

Usually, 3D BSD and surface seismic data are processed separately and in most cases at different time periods. The final BSD image is low-cut filtered to match the bandwidth of the surface seismic image and then spliced into it. This procedure does not guarantee adequate consistency of the final images (see e.g. Müller et al., 2010). Since both datasets have encountered the same heterogeneities in the subsurface, it should be rather logical to integrate them in one imaging-inversion process. The final obtained reflectivity should then explain the BSD as well as the surface seismic data.

The FWM and JMI algorithms, as described in Chapter 3 offer a tool to carry out the simultaneous imaging-inversion process. This is mainly due to the shot-based mechanism of both algorithms. This means that all shot gathers will adequately contribute to the inversion solutions as long as for every particular dataset the right source wavelet or wavefield is utilized. It is also important to ensure the right amplitude-balancing of both datasets with respect to each other. Note again that for 3D borehole data we apply reciprocity to obtain 3D common receiver gathers that become 3D shot gathers similar to surface seismic data with the source position at a certain depth z_n. Therefore, the cost-function from Equation 3.1 can be extended to the

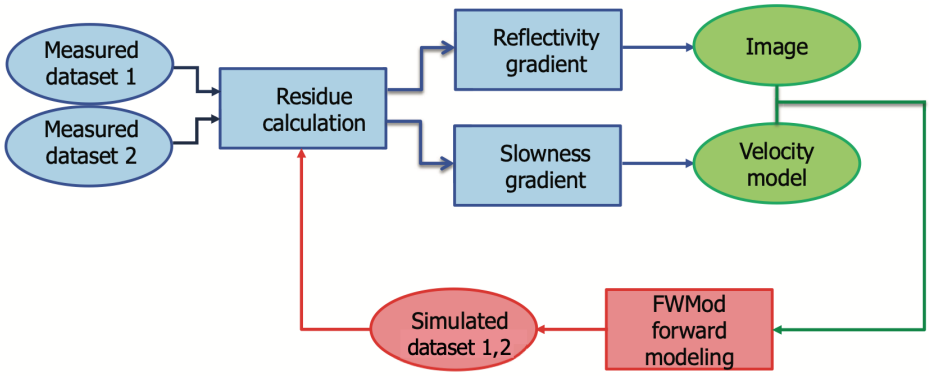

Figure 5.1: Block diagram explaining the simultaneous inversion of different datasets in one integrated JMI process. All shots will contribute adequately to the gradient calculation of the reflectivity image and the migration velocity model, as long as the right corresponding source wavefields are used for every dataset. In addition, amplitude-balancing of both datasets with respect to each other is required.

following expression:

$$J = \frac{1}{2}\sum_{s}\sum_{\omega} \parallel \vec{P}^{-}_{obs}(z_0) - \vec{P}^{-}_{mod}(z_0) \parallel^2 + \frac{1}{2}\sum_{b}\sum_{\omega} \parallel \vec{P}^{-}_{obs}(z_0) - \vec{P}^{-}_{mod}(z_0) \parallel^2, \tag{5.1}$$

where the subscripts s and b indicate the summations over the surface and borehole seismic shot gathers respectively. The subscript ω indicates the summation over all frequencies. $\vec{P}^{-}_{obs}(z_0)$ represents the observed data and $\vec{P}^{-}_{mod}(z_0)$ is the modelled data for a particular shot gather s or b detected at the measurements-surface z_0. The extended cost-function from Equation 5.1 is then minimized based on a gradient descent scheme, as illustrated in Figure 5.1, where we are continuously feeding back the residue from both datasets into the JMI engine until optimized reflectivity and velocity models are obtained. Note that the solutions for the reflectivity image and the migration velocity model will naturally inherit the broader frequency-bandwidth content of the borehole data, within the area around the borehole that is properly illuminated by the BSD data.

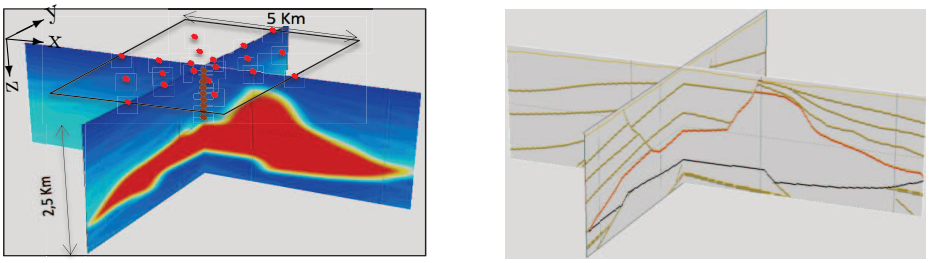

a) *b)*

Figure 5.2: 3D SEG salt model. a) Velocity model with the acquisition geometry. b) True reflectivity model.

5.2 Simultaneous FWM of BSD and surface seismic data

In this section we first focus mainly on the integration of 3D BSD dataset with surface seismic data in the imaging stage by assuming that the velocity model is known. This is demonstrated for the 3D SEG salt model depicted in Figure 5.2a. The true reflectivity model, which is derived from the 3D velocity model, is displayed in Figure 5.2b.

5.2.1 3D FWM of only 3D BSD

For the 3D BSD dataset, we have used reciprocity, meaning that in the modelling as well as the imaging process the sources are assumed in the well, while the receivers are located at the surface. The well location was set at the center of the model. The 3D BSD dataset was modelled, with a maximum frequency of $50Hz$, for nine levels with elevation starting from $z = 100m$ up to $z = 900m$ with $\Delta z = 100m$. The modelling was carried out using the FWMod algorithm, which is based on one-way wave propagation and scalar reflectivities, as explained in Chapter 2. In the reciprocal domain the receiver grid, at the surface, was chosen to be uniform with $\Delta x = \Delta y = 20m$ and covering an area of $3km$ by $3km$ around the borehole. The FWM algorithm is applied to this dataset and the results are displayed in Figure 5.3. Note the significant improvement in the FWM image when compared with the image from conventional PSDM, where the imaging algorithm assumes primary reflections only, while the data contains multiples as well, which are mapped as crosstalk. Shallow reflectors, like the water bottom, and the salt flank are well imaged with maximum lateral extent and high resolution. This is mainly

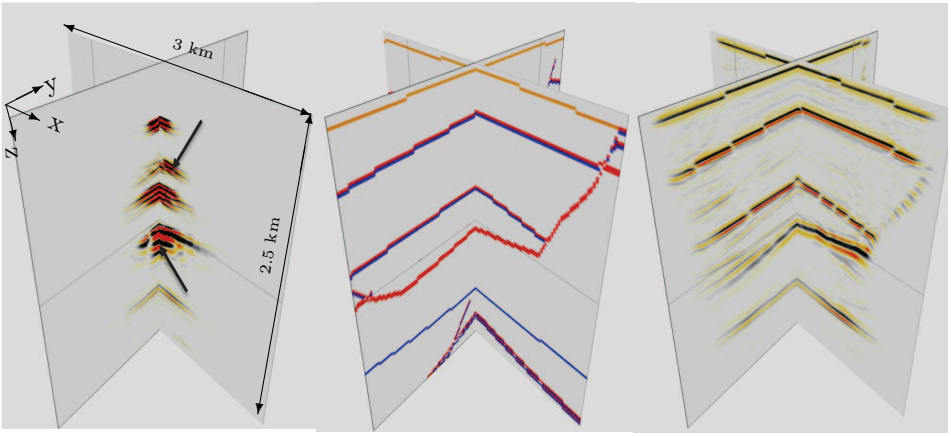

a) b) c)

Figure 5.3: 3D estimated reflectivity based on only the 3D BSD dataset. a) Result of conventional PSDM. b) True refelctivity. c) Result of the FWM approach. Note the artifacts from the multiples in the PSDM image as indicated by the black arrows.

due to the closed-loop approach of FWM and the fact that the multiples are correctly mapped into the right location and, thereby, contribute to the image.

5.2.2 Integration of surface seismic and 3D BSD

3D surface seismic data was modelled, with a maximum frequency of $30Hz$, using a moving split-spread geometry of $1500m$ by $1500m$ with $\Delta x = \Delta y = 20m$ and twenty sources with the configuration as illustrated by the red dots in Figure 5.2a. Figure 5.4 shows a cross-section from a 3D surface seismic versus a 3D BSD shot record. Primary reflections and multiple scattering from several reflectors and the salt structure can be observed. Furthermore, the BSD dataset has a broader frequency-bandwidth. Figure 5.5 shows a comparison of the result of the integrated FWM process of 3D BSD and surface seismic data with the result of conventional imaging, where this time only primary reflections from the 3D surface seismic and 3D BSD data are selected and used as input to the prestack depth migration process. Both datasets are then processed separately and the final BSD image is spliced into the surface seismic image like is done in the industry's daily practice. Note the acquisition geometry footprint because of the sparseness of the sources

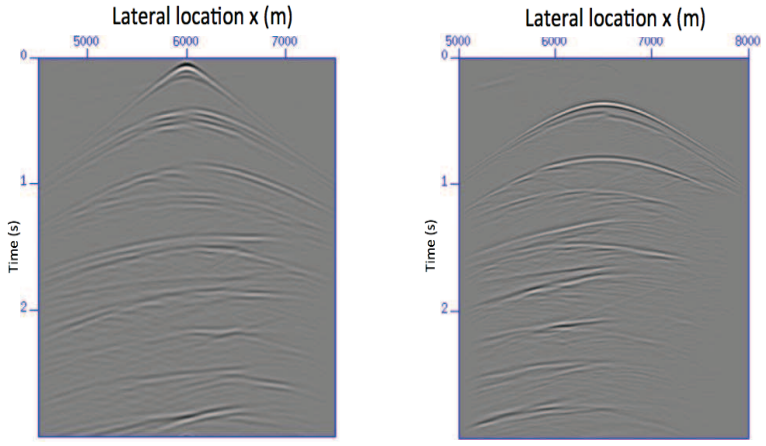

a) *b)*

Figure 5.4: Cross-section from a 3D shot record. a) Result for surface seismic data with maximum frequency of $30Hz$*, the first strongest event is the water bottom primary reflection. b) Result for BSD dataset with maximum frequency of* $50Hz$*. Note that in the BSD dataset the direct wavefield is removed.*

configuration in the 3D surface seismic and the expected discontinuities at the interface of the two images, as can be seen in Figure 5.5a. The integrated FWM image in Figure 5.5b shows a remarkable enhanced resolution and a smooth transition from the area covered by the BSD dataset to the area covered solely by surface seismic data. Moreover, the acquisition footprint visible in image 5.5a are removed due to the contribution fom the multiples and the closed-loop character of the FWM algorithm.

5.3 Simultaneous JMI of BSD and surface seismic data

In the JMI algorithm the inversion problem is made less non-linear by decoupling propagation operators that describe the kinematics from the scattering operator that affect the amplitude in the seismic data. However, In the case of geological environments with high-velocity contrast like what we encounter in areas with complex salt structures, the estimated reflectivity should be used as additional constraint for the velocity gradient, as discussed in Chapter 3

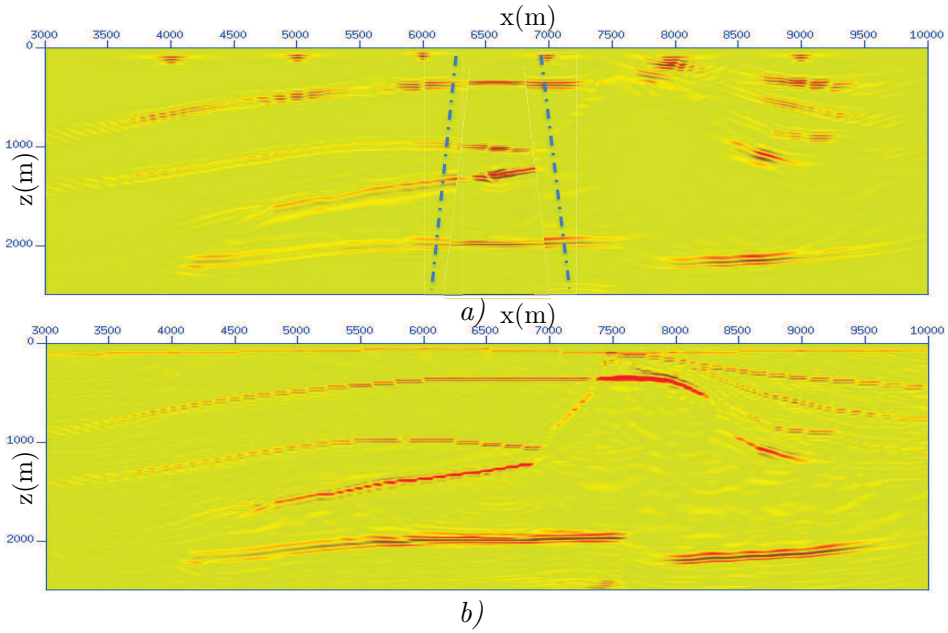

Figure 5.5: Comparison of conventional and FWM imaging. a) A cross-section from the 3D PSDM image of the BSD dataset spliced into the 3D PSDM image of surface seismic, the dashed lines indicate the area covered by the 3D BSD dataset. b) A cross-section from the 3D integrated FWM image of surface seismic and BSD dataset. Note the better resolution and the smooth transition from the area covered by the BSD dataset to the area covered solely by surface seismic data.

and 4. This will help expedite the inversion process and steering it toward a more reliable solution, especially when we deal with datasets with sparse acquisition geometry like 3D borehole or OBN seismic data data. In this section we will demonstrate the simultaneous JMI of different datasets like multi-well BSD and surface seismic data.

5.3.1 3D JMI of a single-well borehole seismic dataset

A relatively small 3D model is selected from the 3D SEG salt model to demonstrate the simultaneous JMI process. Figure 5.6c shows the true velocity model along with its reflectivity model. It covers a total area of $6km$ by $6km$ and a total depth of $2km$. 3D BSD seismic data was modelled, with a maximum frequency of $20Hz$. Again we used reciprocity meaning that for the modelling and the imaging process the sources are assumed in the well,

while the receivers were located at the surface. The vertical-well location was set close to the fault at the cross-section as indicated in Figure 5.6c. The 3D BSD dataset was modelled, for thirty-seven levels with elevation starting from $z = 0m$ up to $z = 1440m$ with a $40m$ interval. The receiver grid is fixed and is densely sampled over the complete areal extent of the model according to a uniform grid with $\Delta x = \Delta y = 20m$.

In this numerical example, we have started the JMI process with a $1D$ velocity profile, as depicted in Figure 5.6a. In Figure 5.6b, we see the results of the JMI algorithm for the estimated velocity and reflectivity model, where the full wavefield (primaries, multiples and down-going wavefield) is deployed in the inversion process. In spite of the sparse acquisition geometry, at the borehole side, the 3D JMI algorithm was able to update the velocity model and steer it toward a reasonable solution. This is mainly because the multiple scattering and the down-going wavefield are reinforcing the primary energy during the inversion process. It can clearly be noticed that the JMI algorithm has succeeded in updating the velocity model even in areas beyond the coverage of primary reflections, which is due to the contribution of the multiple scattering and the down-going wavefield. Furthermore, the main features of the salt structure are retrieved, despite the poor quality of the starting model, mainly because of the reflectivity constraint. The obtained velocity model has a smooth profile that explains the kinematics in the seismic data and the high-resolution details can be found in the corresponding reflectivity model. Note the tremendous improvements in the final image compared to the estimate from the first iteration, which is equivalent to the output of conventional PSDM.

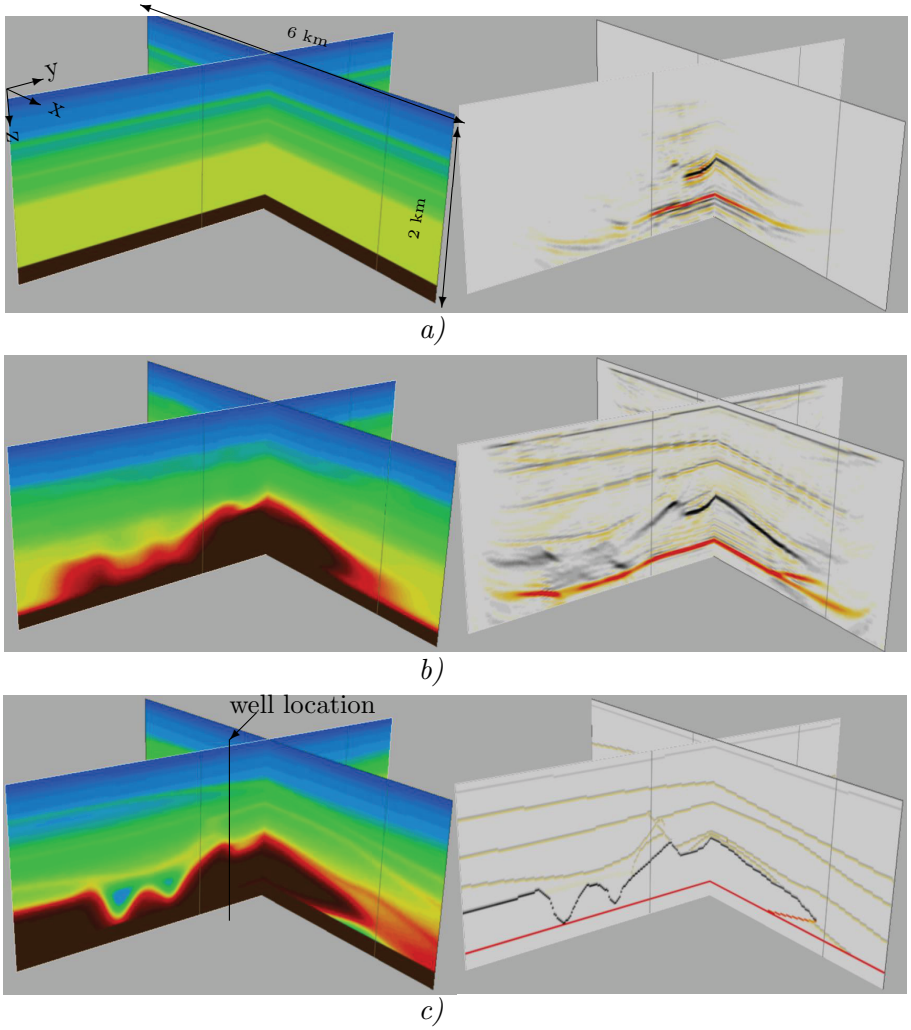

Figure 5.6: 3D view of the JMI results of single-well borehole data. a) The starting velocity model together with the reflectivity image from the first iteration . b) The JMI estimated model and its corresponding reflectivity image. c) The true velocity model and the true reflectivity image. Note the maximum areal extent of the JMI results, this is mainly from the contribution of the multiple scattering that is reinforcing the primary energy during the inversion process.

The final estimate of the reflectivity is consistent with the true reflectivity model, within the area that is adequately illuminated by the total wavefield,

and has maximum lateral coverage with a resolution that is determined by the seismic data frequency bandwidth. Figure 5.7b shows a lateral cross-section from the final 3D JMI reflectivity model, for which the true reflectivity is shown in Figure 5.7c. The contribution of the multiple scattering and the down-going wavefield in the JMI reflectivity image is clearly noticeable, especially at the shallow part of the image where the lateral extent is maximized. Moreover, the salt body is better illuminated even beyond areas outside the coverage range of primary reflections, which can be detected from the reflectivity image at the first iteration that is displayed in Figure 5.7a. Furthermore, the high angles present in the 3D borehole data, because of the position of the deeper sources which is close to the target area, make the JMI algorithm more sensitive to erroneous velocities, hence, expediting and steering the algorithm to a more accurate solution.

5.3.2 3D JMI of multi-well borehole seismic data

In this section, we will demonstrate the capability of the 3D JMI algorithm in simultaneously inverting seismic datasets from different wells that are present in a certain area. By combining datasets from different wells, some illumination problems can be overcome and additional constraints will be put on the estimated model parameters. In this numerical example, an additional 3D BSD dataset is simulated in a second well, as indicated in Figure 5.7c. Both datasets are then jointly utilized in one integrated JMI process and the results are displayed in Figure 5.7d. Note the better illumination of the top of the salt and also some dipping shallow reflectors around $1000m$ depth, between well 1 and 2. Figure 5.8d shows the 3D JMI velocity model, when both datasets are combined in the inversion process, compared with the 3D JMI model when only the dataset from well number 1 is deployed represented in Figure 5.8b. It is clearly noticeable that the velocity model, in the area around well number 2, is significantly improved and shows more similarities with the true model (Figure 5.8c). This demonstrates that the more datasets are included in the JMI inversion process the better the estimated model parameters will be. Figure 5.9 shows a depth slice from the 3D velocity models of Figure 5.8 at the depth position as indicated by the black line in Figure 5.8c. It can be noticed that both datasets from well number 1 and 2 are reinforcing each other when they are simultaneously deployed in one JMI process and consequently a better velocity profile delineation is achieved.

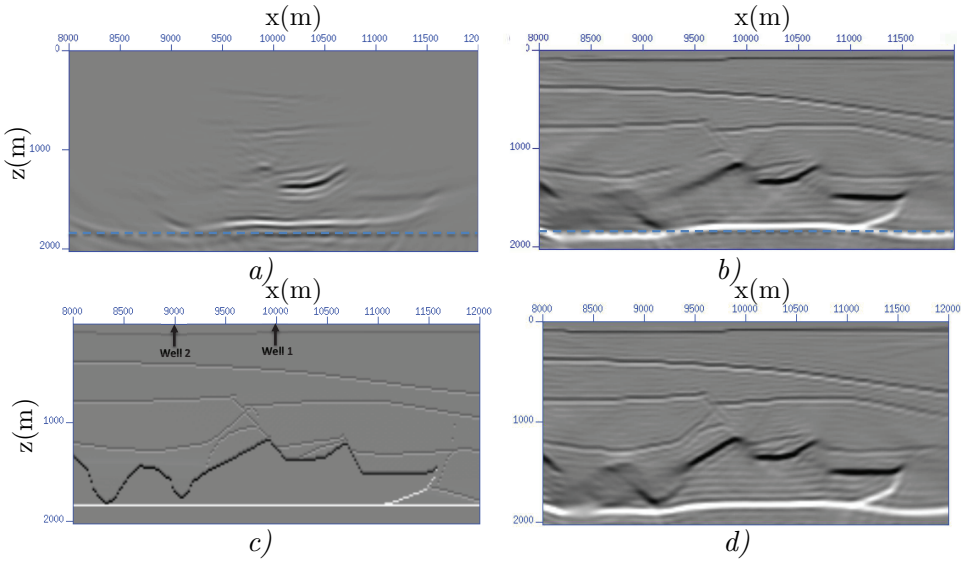

Figure 5.7: Vertical cross-section from the 3D JMI reflectivity image showing comparison between conventional imaging, JMI imaging based on a dataset from one well and JMI imaging of two borehole datasets simultaneously. a) Reflectivity image from the first iteration using the dataset from the first well, which is equivalent to conventional PSDM image. b) Final JMI reflectivity image based on the dataset from the first well. c) The true reflectivity image as a reference. d) Final JMI reflectivity image based on the datasets from both wells. Note the better focusing and the correct positioning of the salt structure in Figure b) and d), which can be seen along the dashed line indicating the true basement reflector depth. Moreover, significant enhancement of the illumination is achieved and consequently improved results when the two datasets are deployed simultaneously.

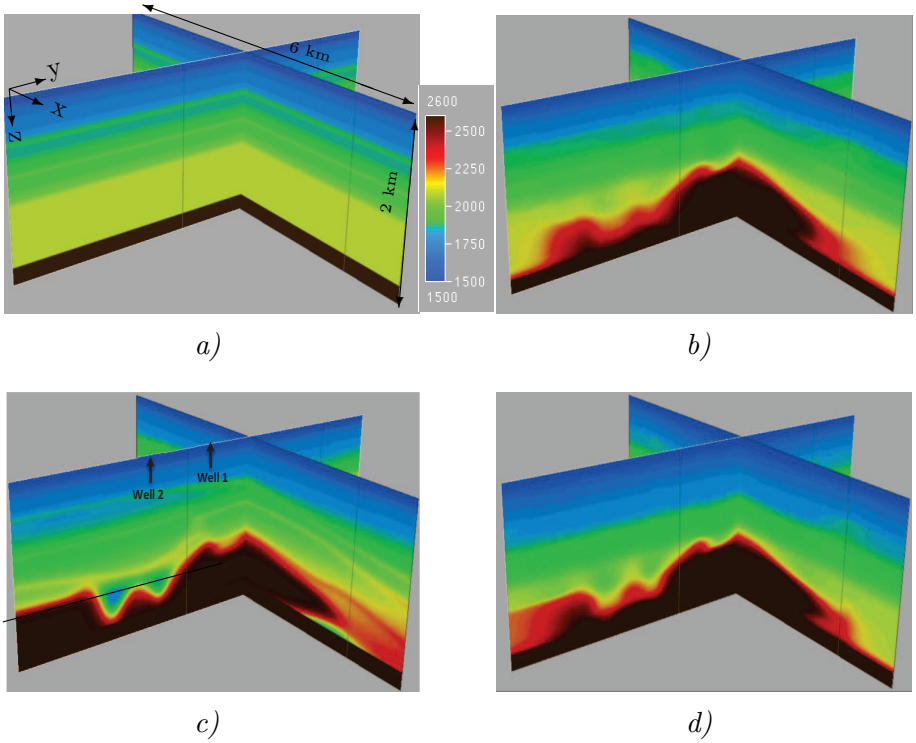

Figure 5.8: 3D view of the JMI model showing comparison between results based on inversion of a dataset from one well versus results when two borehole datasets are deployed simultaneously. a) Initial migration velocity model. b) JMI model when only the dataset from well number 1*, located at* $x = 10000m$*, is utilized. c) The true velocity model, with the well-locations indicated. d) JMI model when both datasets from wells number* 1 *and* 2 *are simultaneously utilized, where well number* 2 *is located at* $x = 9000m$*. Note the better delineation of the velocity profile in the area around well number* 2*.*

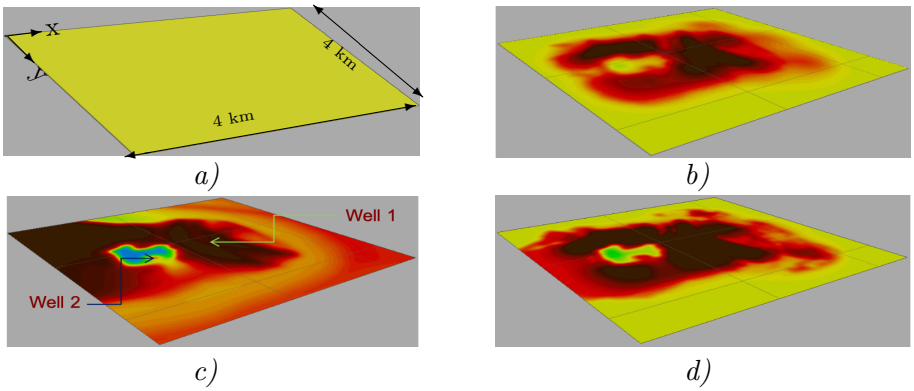

Figure 5.9: Depth slice from the JMI model showing comparison between results based on inversion of a dataset from one well versus results when two borehole datasets are deployed simultaneously. a) The starting model. b) The velocity model estimate by deploying only the dataset from well number 1*. c) The true velocity model, with the well-locations indicated. d) JMI model when both datasets from wells number* 1 *and* 2 *are simultaneously utilized. Note the better delineation of the velocity profile in the area around well number* 2*.*

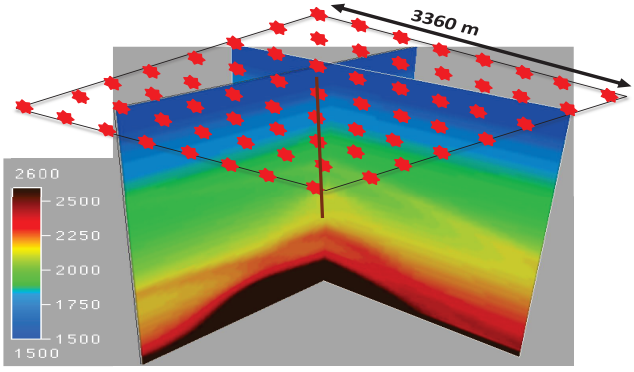

Figure 5.10: The 3D velocity model with the 3D acquisition geometry. The red stars are the source locations and the well location is indicated by the brown line.

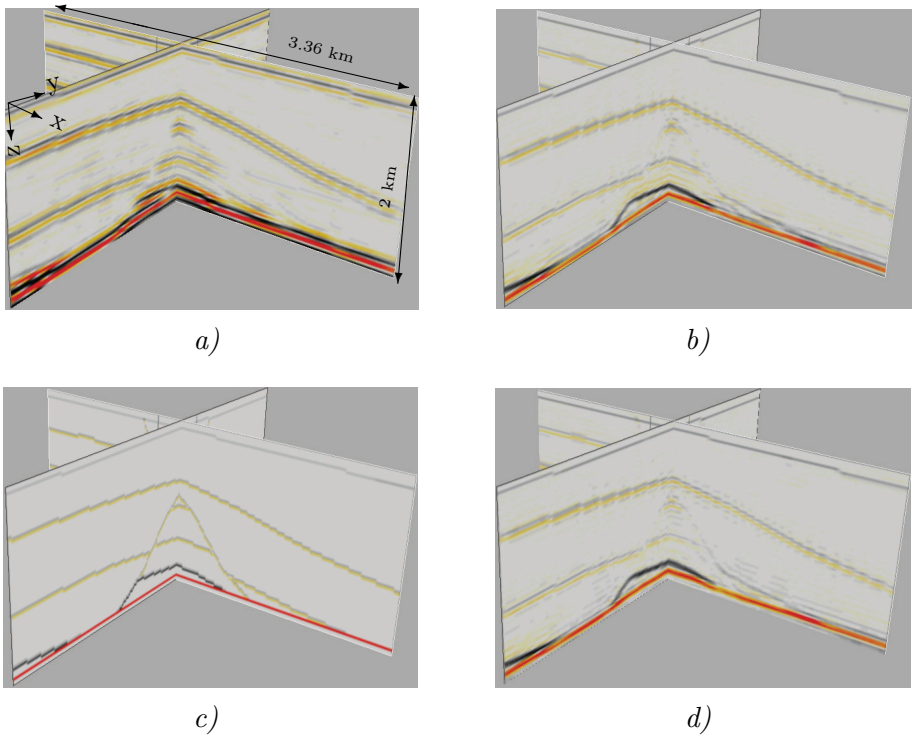

Figure 5.11: Results of the 3D JMI reflectivity image. a) The reflectivity estimate from the first iteration. b) The reflectivity estimate by deploying only surface seismic data. c) The true reflectivity model. d) The reflectivity estimate after including 3D borehole data.

5.3.3 Integration of 3D borehole and surface seismic data

Finally, we will illustrate the simultaneous JMI technology for the 3D model depicted in Figure 5.10, in which now surface and borehole data are simultaneously deployed. 3D surface seismic data was modelled, according to the sparse source configuration, as displayed in Figure 5.10, with the receivers densely sampled over the complete areal extent of the model according to an uniform grid with $\Delta x = \Delta y = 20m$. For the 3D BSD dataset, we have used reciprocity by assuming the sources in the borehole and the receivers at the surface. The seismic data was modelled with a maximum frequency of $20Hz$, using an algorithm based on one-way wave propagation operators and scalar reflectivities.

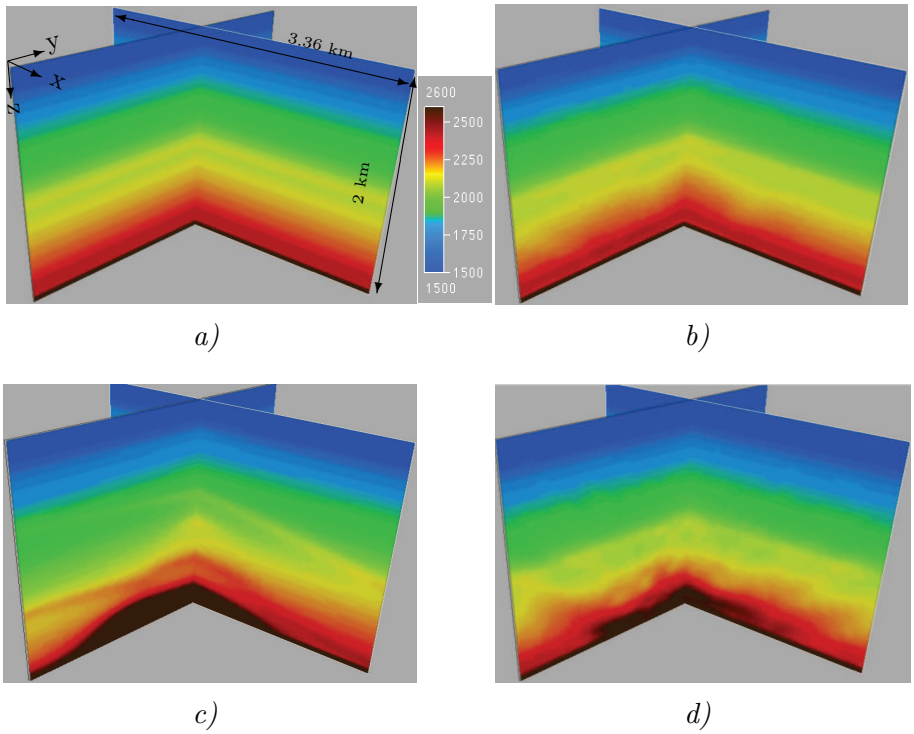

Figure 5.12: Results of the 3D JMI migration velocity model. a) The starting velocity model. b) The velocity model estimate by deploying only surface seismic data. c) The true velocity model. d) The velocity model estimate after including 3D borehole data. Note the better definition of the relatively high-velocity structure (indicated by the brown color) when borehole data is included in the inversion process.

In order to demonstrate the added value of the borehole data, we have first deployed only surface seismic data in the JMI algorithm and after 45 iterations the borehole data was engaged. Figure 5.11 shows the results of the JMI algorithm for the estimated reflectivity models, with and without the borehole data, where the full wavefield (primaries and multiples) is deployed in the inversion process. Figure 5.12 displays the estimated velocity models. After including the 3D borehole data, the 3D JMI algorithm was able to produce a good estimate of the velocity and reflectivity model mainly due to the high angles that are available in the 3D borehole data because of the position of the deeper sources that are close to the target. Furthermore, the multiple scattering is reinforcing the primary energy during the inversion process to produce the best estimate for the reflectivity and velocity models

in spite of the sparse acquisition geometry. Figure 5.13 displays a depth slice from the 3D velocity cube estimated by the JMI algorithm, with and without the 3D borehole data. When the 3D borehole data is deployed, a better delineation of the high velocity structure is achieved, especially around the borehole location, which is in the middle of the slice. This is mainly due to the sensitivity of the JMI algorithm to the high angles available in the 3D borehole data.

5.4 Discussion

In this chapter, we have demonstrated the added value of the simultaneous deployment of different datasets, like 3D borehole with surface seismic data and multi-well 3D borehole data, in one JMI process. In the case of 3D borehole data, reciprocity is used by exchanging the sources and receivers positions 3D buried-shot records are obtained, with the "receivers" at source elevations and the "source" at the receiver depth. The JMI process is a shot-based algorithm meaning that all shot-gathers will adequately and evenly contribute to the inversion solutions, within their coverage area, as long as for every particular dataset the right source wavelet or wavefield is utilized and amplitude-balancing of both datasets with respect to each other is ensured. In spite of the sparse acquisition geometry, the 3D JMI algorithm is able to provide adequate estimate of the reflectivity image and migration velocity model, mainly because of the high angles available in the 3D borehole data and the contribution from the multiple scattering including the downgoing wavefield. The numerical examples presented in this chapter show the effectiveness of the JMI approach, even in a complex geological environment, in retrieving the right kinematics properties from 3D borehole data and translate it into proper velocity updates. It is demonstrated that integrating borehole data with surface seismic or simultaneously inverting datasets from different boreholes in one JMI process leads to improved images and enhanced migration velocities, especially in the area around the boreholes.

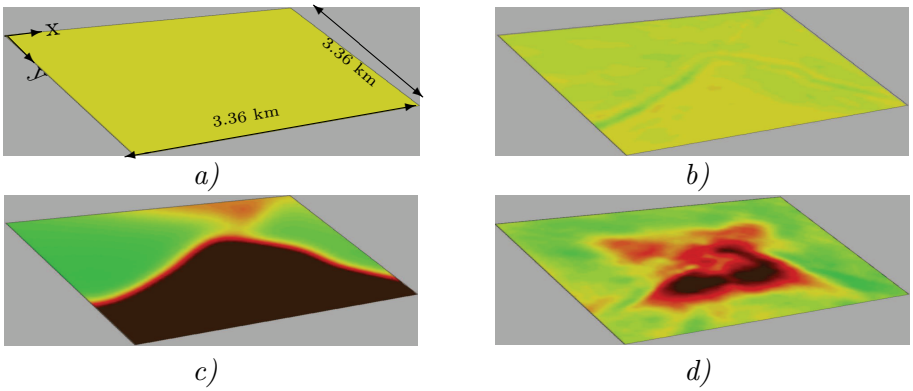

Figure 5.13: Depth slice from the JMI migration velocity model. a) The starting model. b) The velocity model estimate by deploying only surface seismic data. c) The true velocity model. d) The velocity model estimate after including 3D borehole data. Note the better definition of the relatively high-velocity structure (indicated by the brown color) when borehole data is included in the inversion process.

Even though the demonstrated examples are assumed to represent only the vertical component of the 3D borehole seismic data, the integrated imaging of different seismic measurements, presented in this chapter, provides us also with an opportunity to simultaneously image multi-component 3D borehole and OBN datasets. It is expected that some conventional preprocessing steps, like the PZ summation in the case of OBN data, will become unnecessary and obsolete mainly because they will be handled automatically during the JMI inversion process.

6

High-resolution reservoir monitoring using the full wavefield of 3D BSD surveys

Within the energy industry, the process of reservoir characterization and development requires profound knowledge and extensive understanding of the subsurface. Therefore, 3D BSD surveys are acquired to provide us with high-resolution images (Al Bannagi et al., 2018) and also to produce accurate estimates of the subsurface properties and lithology especially when utilized as input to pre-stack elastic inversion algorithms (Ahmad et al. (2012); Leaney (2015)). Moreover, the small volume-size of the 3D BSD surveys makes it very attractive and suitable for time-lapse imaging or even continuous reservoir monitoring for the area around the borehole, especially when combined with modern acquisition techniques like DAS technology where a recording cable can be permanently installed in the borehole without disturbing the production activities.

As was demonstrated in the previous chapters, the sparsity of the BSD surveys requires the deployment of imaging algorithms with closed-loop architecture, like FWM and JMI. This will improve the non-uniform fold distribution at every imaging grid-point and increase the lateral extent of the image further away from the borehole. The latter is achieved by utilizing the full signal measured in the 3D borehole data, including all multiple scatter-

ing from both up- and downgoing wavefields. In fact, closed-loop algorithms circumvent some principal issues that we encounter in time-lapse imaging like the requirement of the repeatability of the acquisition geometry (Qu and Verschuur, 2017) and even produce better results when the acquisition geometry parameters are by design not repeated. This is similar to retrieving sharp images or videos from consecutive blurry snapshots by taking temporal information and changes into consideration and communicating that through all observations during the inversion process (Wieschollek et al., 2017).

6.1 Introduction

In geophysics, time-lapse imaging is concerned about the mapping and detection of changes, like the fluid dynamics and rock properties, within a certain reservoir over a certain period of time. Therefore, subsequent seismic surveys are acquired and compared with each other in the data and/or image domain to retrieve the needed information about the reservoir (Lumley et al., 2003). In conventional time-lapse imaging, the acquisition geometry is required to be densely sampled and exactly repeatable for all surveys in order to ensure that the measured changes are purely a function of time. In addition, all processing steps should be the same for all surveys and the multiples must always be suppressed from the seismic data to fulfil the linear assumption of the utilized imaging algorithms. All these requirements become obsolete and even not desired when full wavefield algorithms, like FWM and JMI, are deployed. This was already shown by Qu and Verschuur (2017) for 2D surface seismic data by fitting all the datasets from the different surveys simultaneously, which allows the baseline and the monitoring surveys to communicate and complement each other during the inversion process to reduce the non-repeatability uncertainties. This can be achieved only by deploying imaging algorithms with a closed-loop architecture. Alternatively, inverting every survey separately using the FWM or JMI algorithm then subtracting the results afterwards is the simplest and most straightforward approach to obtain a time-lapse image. However, in that case it is still required to have the same acquisition geometry for the baseline and the monitoring surveys. This repeatability requirement might be relatively simple to realize for small surveys like in the case of 3D BSD data, where the small volume-size and the relatively good signal to noise ratio in combination with enhanced inversion-imaging algorithms will make it possible to retrieve high-resolution time-lapse images within a reasonable turnaround time. Tertyshnikov et al. (2018) have demonstrated the capability of 3D BSD measurements to produce reliable time-lapse images and monitor the evolution of the CO2 plume, even though

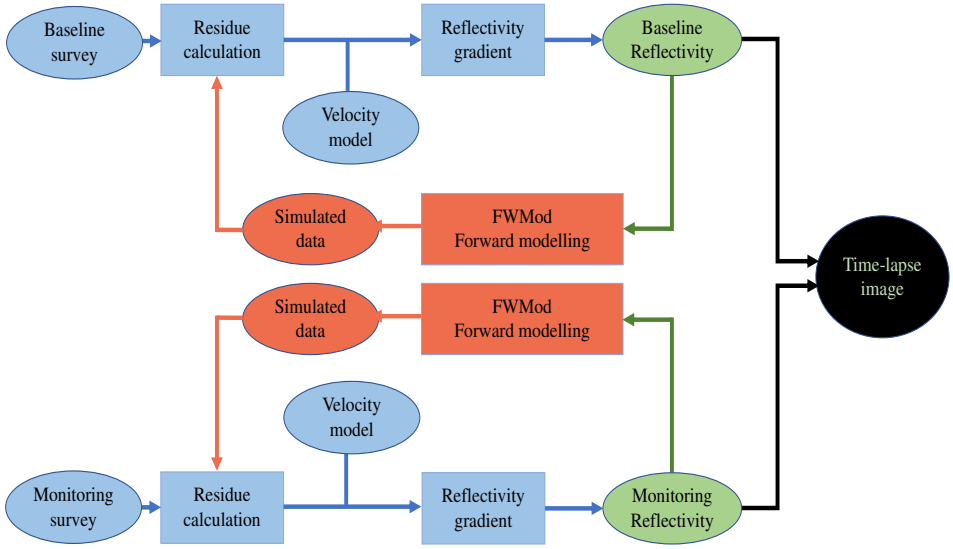

Figure 6.1: Block diagram explaining the workflow to retrieve a time-lapse image. The baseline and monitoring surveys are inverted separately and the final results are subtracted from each other. Note that a more sophisticated approach would be to invert all surveys simultaneously in one integrated scheme, however that is beyond the scope of this thesis.

only primary energy in combination with a conventional imaging algorithm was used. In this chapter, we will demonstrate a first attempt to retrieve a high-resolution time-lapse image based on 3D BSD, modelled using the SEG salt model, by deploying the FWM algorithm in order to make use of the full multiple scattering present in the data to enhance the quality of the time-lapse result.

6.2 Reservoir monitoring using the FWM algorithm

A major advantage of full wavefield algorithms like FWM and JMI is the deployment of the full measured signal including all higher-order scatterings. Combining the enhanced measurements from the 3D BSD with the FWM/JMI inversion-imaging algorithm results in a reliable reflectivity and velocity model that better explain changes in reservoir properties caused by injection and production. The same cost-function from Equation 3.1 is then engaged and minimized based on a conjugate gradient scheme as explained

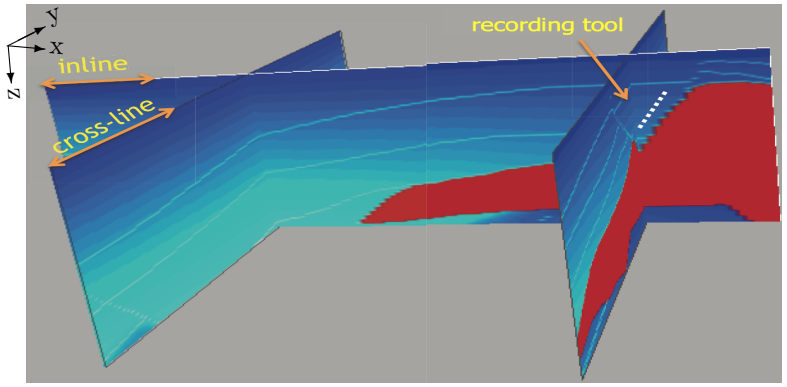

Figure 6.2: The true velocity model that was used to model the baseline survey. The deviated well trajectory is indicated by the dashed white line and the recording tool covers a total length of $1200m$.

in Chapter 3. Figure 6.1 shows a block diagram explaining the workflow of retrieving a time-lapse image by producing two subsurface reflectivity images for the baseline and monitoring survey. The velocity model is kept constant for both cases and the modelled data is iteratively compared to the measured one by closing the loop in the inversion-imaging process and feeding back the residue into the FWM engine. Consequently, optimized estimates of the subsurface reflectivity $\mathbf{R_{bsl}}$ and $\mathbf{R_{srv}}$ will be obtained for both the baseline and monitoring survey. The time-lapse effect is then simply the difference between the two estimated subsurface reflectivities.

$$\mathbf{R_{timelapse}} = \mathbf{R_{srv}} - \mathbf{R_{bsl}}. \tag{6.1}$$

6.3 3D SEG salt model time-lapse application

In this section we will illustrate the workflow described in the preceding section to retrieve a high-resolution time-lapse image based on 3D BSD dataset obtained from the 3D SEG salt model. The baseline survey was modelled with a 3D acoustic finite differences code by using a zero-phase Ricker wavelet with peak frequency of $10Hz$. In this example, we have used reciprocity, which means that the sources are placed in the borehole and receivers are at the surface according to carpet-receiving geometry, with $\Delta x = \Delta y = 20m$. The well was placed along the salt flank with lateral deviation of $300m$ in both directions. The acquisition tool covers a total depth interval of $1200m$ starting

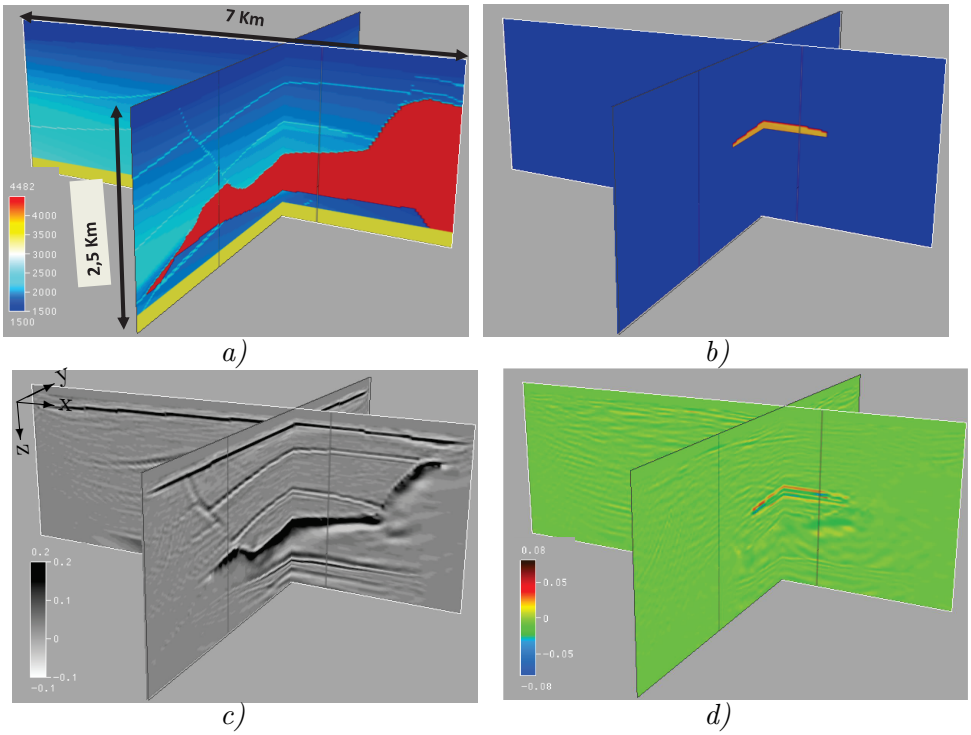

Figure 6.3: Results of time-lapse imaging using the FWM algorithm. a) The true velocity model. b) The true induced time-lapse effect, which is a change of 1% *of the velocity model in the indicated area. c) FWM reflectivity image from the baseline dataset. d) FWM estimated time-lapse effect. Note that we have used the same velocity model to image both the baseline and monitoring survey.*

from $z = 300m$ and depth steps of $40m$. Figure 6.2a shows a 3D view of the SEG salt model with the acquisition geometry. In order to simulate a scenario with changes in reservoir properties that can be caused by production or injection, a monitoring survey was modelled with the same acquisition parameter but with different noise level and after altering the velocity model by 1% in the area as indicated in Figure 6.3b. As a first approach, the datasets from both surveys are separately engaged in a FWM process and after the same number of iterations the final images are subtracted from each other to obtain the time-lapse effect. Alternatively, the simultaneous inversion of the baseline and the monitoring survey could produce even better time-lapse results (Qu and Verschuur, 2021), especially in the case of more complex field data situations, however this is beyond the scope of this thesis.

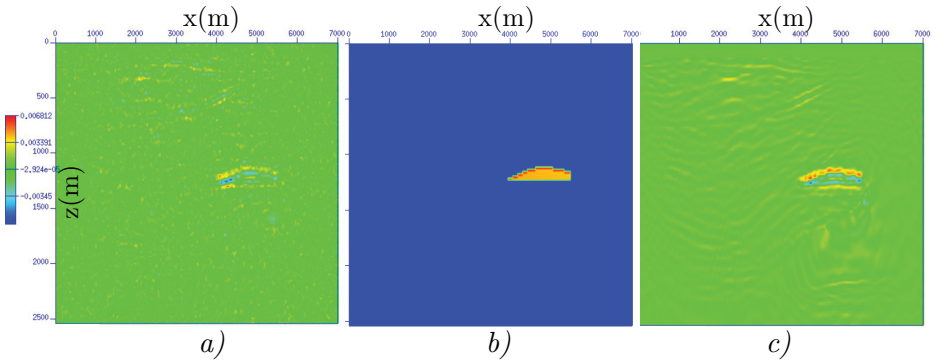

Figure 6.4: Vertical slices from the results of time-lapse imaging using the FWM technology. a) Vertical section from the conventional time-lapse imaging. b) Vertical section from the true time-lapse effect. c) Vertical section from the FWM estimated time-lapse image.

In this experiment, the true velocity model is used and only the reflectivity image was updated during the iterations. In the case of non-reliable velocity model, the JMI algorithm should be deployed to update the erroneous migration velocities as well. Figure 6.3c displays the 3D FWM reflectivity image obtained from the baseline dataset with a remarkable high-resolution characteristics and maximum lateral extent, which is consistent with the true velocity model. This is mainly because of the higher-order scattering and the closed-loop approach of the FWM process. The relatively small induced velocity increase has been retrieved in the time-lapse image as shown in Figure 6.3d. Figure 6.4 shows a vertical slice from the FWM estimated time-lapse image. Note the significant improvement of the resolution and decrease of the noise level. Figure 6.5 shows a depth slice at the top of the reflector where the change in the reservoir properties is assumed to happen. Note the consistent agreement of the time-lapse effect depth slice with the depth slice of the true velocity model difference.

6.4 Conclusions

In this chapter, the capability of the FWM algorithm to retrieve time-lapse images using 3D BSD seismic data is successfully demonstrated. Within the FWM framework, it is relatively straightforward to simultaneously invert the full wavefield including all high-order scattering from both up- and downgoing wavefields available in the 3D BSD measurements. In spite of the sparse acquisition geometry, the 3D FWM algorithm is able to provide reliable es-

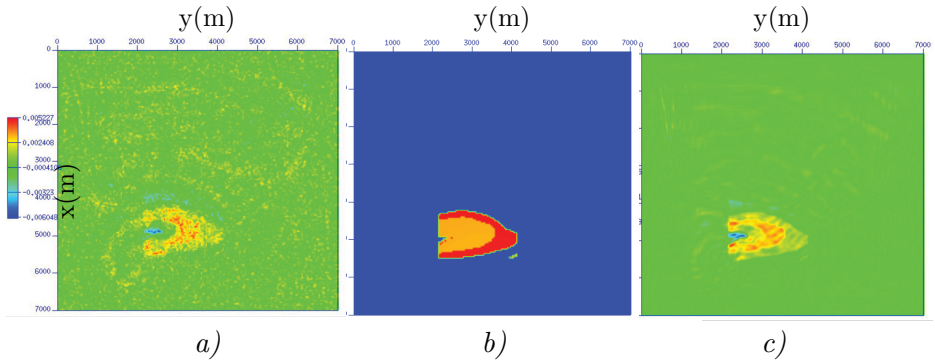

Figure 6.5: Depth slices from the results of time-lapse imaging using the FWM technology. a) Depth slice from the conventional time-lapse imaging. b) Depth slice from the true induced time-lapse effect. c) Depth slice from the FWM estimated time-lapse image.

timates of the reflectivity image and the time-lapse image. This is mainly because the multiple scattering is improving the subsurface illumination and reinforcing the primary energy during the inversion process. The 3D data example presented in this chapter shows that 3D BSD data in combination with the FWM inversion-imaging algorithm can indeed provide reliable solutions and extend over quite an offset range to provide high-resolution information that will be of great added value for reservoir characterization and monitoring. Moreover, an even more enhanced time-lapse results can be achieved if all datasets from the different surveys are simultaneously deployed in imaging algorithms with a closed-loop architecture like FWM and JMI (Qu and Verschuur, 2021). This allows the baseline and the monitoring surveys to communicate and complement each other during the inversion process. Consequently, the non-repeatability uncertainties and the noise level in the final results will be reduced.

7

Potential and challenges of 3D JMI in complex salt environment

In the case of geological media with complex structures like steep salt flanks, 3D borehole data is usually used to better delineate the salt-sediment boundary (Li and Hewett, 2016). However, the industry standard imaging procedure for 3D BSD is normally conducted after performing the separation of the up- and downgoing wavefields typically in the frequency-wavenumber domain. This will cause loss of valuable scattered energy that propagates horizontally toward the receivers in the borehole after illuminating steep or vertical structures in the subsurface like salt flanks (Gerea et al., 2016). As described in the previous chapters, 3D full wavefield migration (FWM) is an integrated inversion-imaging process that utilizes the full wavefield measured in the 3D BSD surveys, including all higher-order scatterings (i.e. primaries and multiples), without the need for a separation of the up- and downgoing wavefields. This allows us to retrieve and image the scattered energy from the steep structures in the subsurface. Moreover, the angle-dependency of the reflectivity operator must be included in the FWM process in order to drive the residue to an absolute minimum and fully explain the input dataset. The result is then high-resolution common image point (CIP) gathers including the illumination from all higher-order scattering modes. These CIP gathers will contain additional reflection angles even in areas not illuminated by

primary reflections.

The accuracy of imaging complex salt structure and constructing CIP gathers rely on the derivation of correct migration velocity models. This can be very challenging especially in the case of geological scenarios with high velocity contrast and given the current acoustic implementation of the JMI algorithm. In this chapter we will demonstrate the potential and challenges of the FWM and JMI methodology in handling elastic data simulated in a medium based on real geology and rich with converted waves.

7.1 Introduction

In the case of geological scenarios with gentle velocity contrast and weak converted waves, the Joint Migration Inversion technology has proven to be an effective methodology in providing reliable estimates for the subsurface reflectivity and simultaneously its corresponding migration velocity model (Berkhout (2014c); Verschuur et al. (2016); Al Bannagi et al. (2018)). Moreover, during the past years significant progress has been made in the application of the JMI technology to field data and numerical models with more realistic scenarios. However, some issues are yet to be resolved. Especially for the current implementation of the JMI algorithm the angle-dependent effects of the reflectivity operator (Sun et al., 2018) and the cross-talk from the converted waves (El Marhfoul and Verschuur, 2019), when they are not properly taken into account in the FWMod modelling engine, are the main challenges.

In practice, the adopted strategy in the JMI process for field or numerical elastic data to deal with angle-dependent effects is to suppress them in the preprocessing phase such that the velocity update, which should be conducted using scalar reflectivity, will not be affected. As a final step, the FWM algorithm is applied in an angle-dependent reflectivity mode to fully explain the amplitudes in the measured dataset. This process will produce common image point (CIP) gathers that contain the contribution of the higher-order scattering from both the up- and downgoing wavefields of the 3D BSD and exhibit high-resolution character due to the iterations in the closed-loop approach of the algorithm. In addition, the current implementation of the JMI algorithm handles mainly compressional waves, which means that the converted waves should be removed from the input data prior to the JMI process; this can be achieved via moveout discrimination (Al Bannagi et al., 2018), especially in the case of less complex geological scenarios like flat-layered environments or via adaptive subtraction of the estimate of converted waves by

utilizing multicomponent measurements. However, in the case of media with complex geology, like salt domes and dipping reflectors, this becomes a challenging task and the best approach would be to consider elastic scattering operators in the FWMod engine and include the converted waves as well in the JMI process (Verschuur and Hoogerbrugge (2020); Berkhout (2014b)).

In order to demonstrate the shortcomings of the acoustic implementation of the JMI algorithm in retrieving the right migration velocities for seismic data with strong converted waves we will simulate a 3D borehole dataset based on acoustic versus elastic modelling and also a 3D elastic surface seismic dataset. It will be shown that the converted waves, especially in areas around the salt structure, have a significant effect on the JMI inversion process and should be taken into account for a proper conversion of the JMI solution.

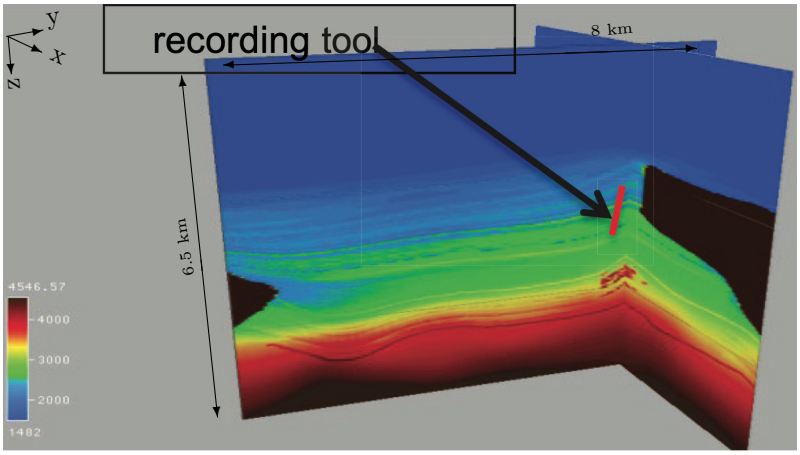

Figure 7.1: The true velocity model with the deviated BSD tool. Note that reciprocity is used, meaning the sources are in the borehole and the receivers are uniformly and densely distributed over the surface.

7.2 Practical prospects of the FWM algorithm for 3D borehole seismic data

The right definition and delineation of salt structures, during the process of velocity-model building of the subsurface, is a crucial step for proper sub-salt imaging and focusing of deeper events (Lomask et al., 2004). The lack of the right salt structure in the migration velocity model will result in a poor and defocused image of reflections from the base of salt and the deeper reflec-

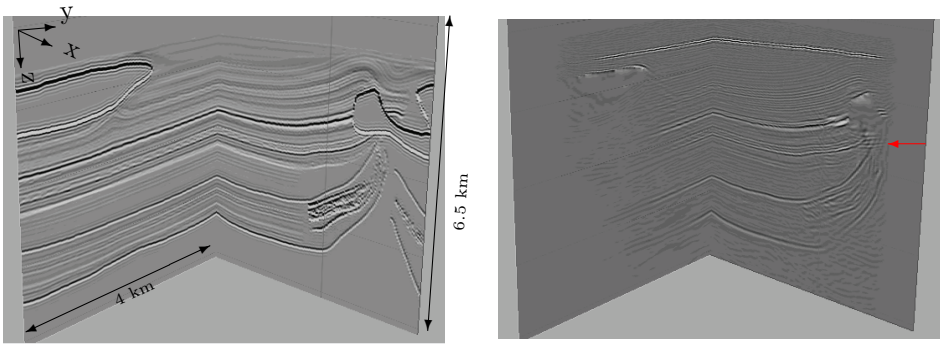

a) b)

Figure 7.2: 3D FWM results. a) The true reflectivity model. b) The FWM estimated reflectivity image. Note the high resolution and maximum lateral extent of the FWM image, which is consistent with the true reflectivity. However, strong crosstalk from the converted waves can be seen beneath the salt structure as indicated by the red arrow.

tors (O'Brien and Gray, 1996). Therefore, in this section we will illustrate the capability of the 3D FWM algorithm in combination with the unique positioning of the BSD tool in the subsurface to retrieve all energy modes available in the 3D borehole data and image steep boundaries of a complex salt structure. In Figure 7.1 we see a display of the 3D velocity model with the BSD tool orientation. The model shows complex salt structures embedded in sediment layers and is based on real geology of an actual exploration area offshore west Africa.

7.2.1 Steep flank imaging using the FWM algorithm

The true velocity model covers a total area of $8km$ by $8km$ and a total depth of $6.5km$. 3D BSD was modelled using a 3D elastic finite difference code for the BSD tool geometry as indicated in Figure 7.1. The maximum imaged frequency is $30Hz$, using reciprocity meaning that for the modelling and the imaging process the sources are assumed in the well, while the receivers are located at the surface. The 3D BSD was modelled, for 115 levels with elevation starting from depth level $z = 2872m$ up to $z = 4250m$ with $\Delta z = 12.5m$. The receiver grid is fixed and is densely sampled over the complete areal extent of the model according to a uniform grid with $\Delta x = 30m$ and $\Delta y = 40m$. In this numerical example, we have used a smooth version of the true velocity model in the FWM process and Figure 7.2 displays a 3D view of the true reflectivity model and the estimated FWM reflectivity image. In spite of the

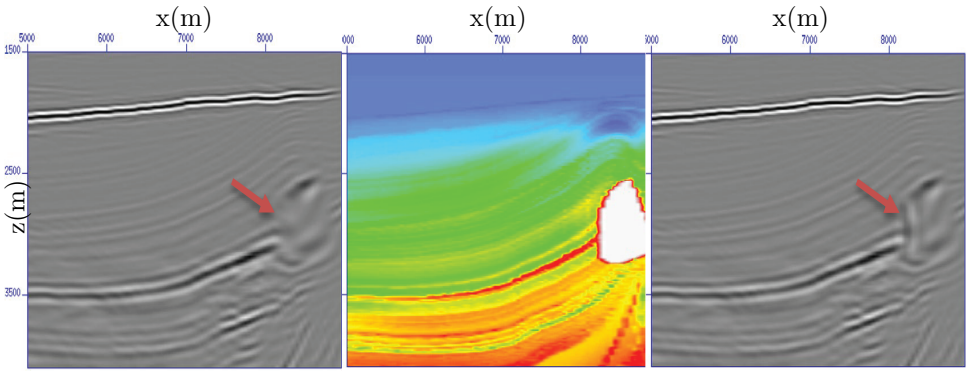

Figure 7.3: 3D FWM results including flank-imaging. a) FWM image without flank-imaging option. b) The true velocity model. c) FWM image with flank-imaging option.

sparse acquisition geometry, at the borehole side, the 3D FWM algorithm was able to retrieve a good solution of the reflectivity model consistent with the true one. This is mainly because the multiple scattering and the downgoing wavefield are reinforcing the primary energy during the FWM process even in areas beyond the coverage of primary reflections. Furthermore, Figure 7.3 shows that the steep events from the salt flank are nicely retrieved, mainly because their corresponding energy modes are preserved in the input dataset. Conventionally, these energy modes are usually lost after performing the separation of the up- and downgoing wavefields, which is based on dips discrimination in the frequency-wavenumber domain, because they are propagating horizontally toward the receivers in the borehole after illuminating the salt flanks. A fortunate feature of the FWM algorithm is that we continuously have access to the up- and downgoing forward modelled wavefields propagating through the imaging model at all depth levels. This makes it possible to apply the imaging condition to the back propagated measured data with the downgoing forward modelled wavefield, which is the regular imaging mode, or with the upgoing forward modelled wavefield for the salt flank imaging mode. This is only possible in the case of borehole acquisition geometry where the "source" is assumed to be positioned in the subsurface facing the steep salt flank. This is illustrated in Figure 7.4, based on the same salt structure from the true reflectivity model in Figure 7.2a, where it is visible that the forward modelled wavefield (indicated in yellow in Figure 7.4) is propagating to the right while the backward propagated measured data (indicated in blue in Figure 7.4) is propagating to the left. This means

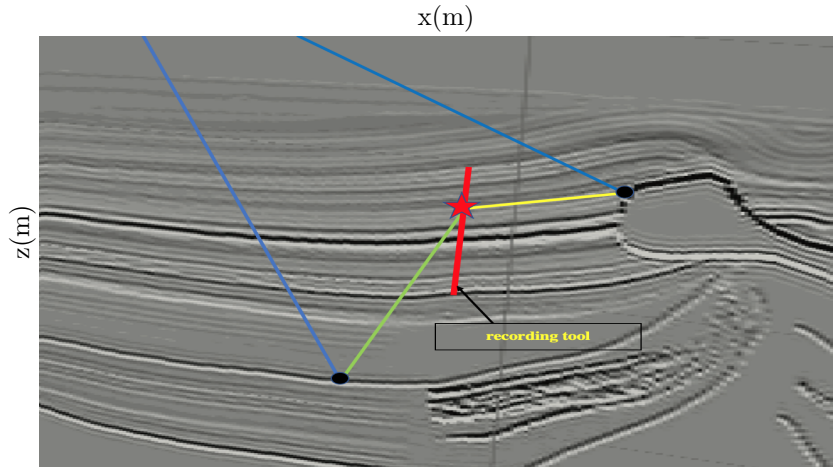

Figure 7.4: Schematic illustration of the salt-flank imaging mode based on reflected energy that reaches the receiver in the BSD tool from above. The data misfit, indicated in blue, is back propagated to every imaging depth level and cross-correlated with the upgoing forward modelled wavefield, indicated in yellow, to retrieve an image of the salt flank. Note that the reflected energy might propagate horizontally depending on the receiver's position in the BSD tool. The green line indicates the downgoing forward modelled wavefield that is utilized in regular imaging mode.

that the cross correlation of these two wavefields, that are propagating in different directions, will produce reflectivity information of the salt flank. This is fully in agreement with the description of the reflectivity operator in Equation 3.5. Note that the wavefields selection for the different imaging modes is done automatically inside the FWM algorithm to ensure the explanation of all energy modes available in the measured data as much as possible. This will result in a final estimate of the reflectivity image that is consistent with the true reflectivity model, within the area that is adequately illuminated by the total wavefield, and has maximum lateral coverage with a resolution that is determined by the seismic data frequency bandwidth.

However, the current implementation of the FWM algorithm does not include mode converted waves, which consequently will be mapped in the final image as crosstalk. This can be clearly seen in Figure 7.2b, as expected, immediately beneath the salt structure. Note that in this case we have used the right P-wave migration velocity model for imaging compressional waves,

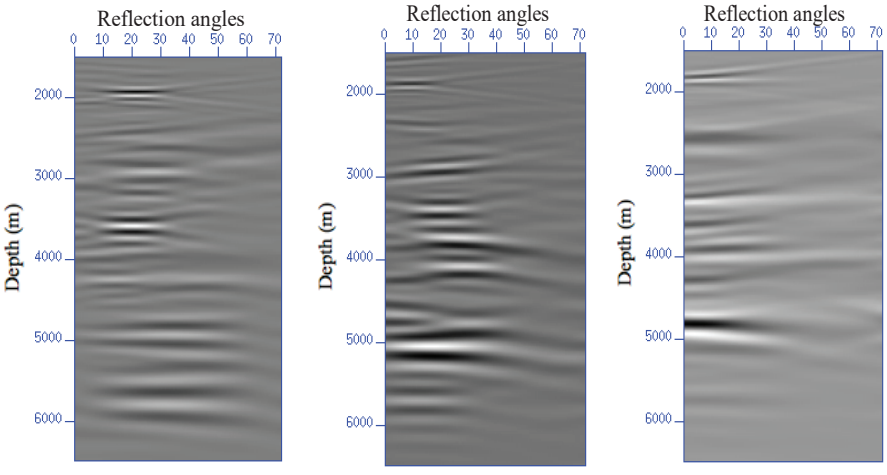

Figure 7.5: 3D FWM angle-dependent CIP gathers. a) lateral location $x = 6500$*, approximately* $1100m$ *away from the well. b) lateral location* $x = 7500$*, approximately* $100m$ *away from the well . c) lateral location* $x = 8500$*, approximately* $900m$ *away from the well. Note that all the reflections in the CIP gathers above depth* $3000m$ *are mainly from the contribution of the higher-order scatterings. Moreover, the variation of the angles coverage of every CIP gather based on its location can clearly be noticed, which is expected from the acquisition geometry of 3D borehole data.*

which by itself acts like a filter to suppress the focusing of the converted waves. Nevertheless, significant mode converted waves residual crosstalk is produced.

7.2.2 Angle-dependent full wavefield imaging of 3D borehole data

In order to be able to fully explain the observed data by producing even better and complete imaging results, the FWM algorithm must be executed using the angle-dependent reflectivity operator $\mathbf{R}$ as described in Chapter 2. This will explain the angle-dependent effect of the reflection coefficients of the boundaries in the subsurface. This can be achieved by constructing CIP gathers, as function of subsurface offset, including the higher-order scattering energy modes and keep updating them in the inversion process until the measured data is fully explained by the simulated data. The CIP gathers

from the final iteration are then converted into ray parameter or reflection angle domain by stretching the subsurface-offset gathers back to time along the depth axis, using the imaging velocity model, and applying a 3D Radon transform (Sava and Vasconcelos, 2011). This will convert the subsurface-offset gathers directly from the horizontally-oriented subsurface-offset domain to the reflection-angle domain that is oriented along the subsurface boundaries.

Figure 7.5 shows FWM angle-dependent CIP gathers at three different lateral locations around the borehole. Note the significant contribution of the higher-order scattering energy modes, specifically at the shallow part (above $3000m$), which is illuminated mainly by the multiples from the up- and downgoing wavefields. The obtained FWM CIP gathers show an angles range that is a function of depth and also varies with the location of the CIP gather. This is consistent with the shape of the subsurface reflectors and expected based on the acquisition geometry of 3D borehole data. The flatness of the CIP gathers can be used as additional QC for the accuracy of the utilized migration velocity model and more importantly they can directly be input to conventional prestack elastic inversion algorithms to produce estimates of the subsurface properties and lithology (Ahmad et al. (2012); Leaney (2015)).

7.3 The potential and challenges of the JMI algorithm in elastic media

Even though the acoustic implementation of the JMI algorithm is neglecting mode converted waves, a substantial update can be achieved for the migration P-wave velocity model. Moreover, the current obtained results suggest the the effect of the mode converted waves on the velocity gradient is more noticeable and stronger in the areas around the salt structure. This will be shown based on 3D BSD and surface seismic data simulated in an elastic medium with high velocity contrast. For this purpose, a second 3D BSD dataset is simulated based on the same velocity model from the previous section (Figure 7.1) using the same acquisition geometry but now deploying an acoustic finite difference code to model purely compressional waves. In addition and for a better understanding of the effect of BSD versus surface seismic acquisition geometry, a supplementary 3D elastic surface seismic dataset is simulated using the same receivers geometry and a sparse regular sources grid with $\Delta x = 500m$ and $\Delta y = 500m$. First a JMI process is conducted by deploying the 3D BSD elastic dataset and the velocity model that was pro-

duced to run prestack depth migration (PSDM), which can be seen in Figure 7.6b, as the starting velocity model. It shows gentle and very smooth lateral velocity variations and contains no salt information at all. As described in the previous section the full wavefield in the 3D BSD is utilized to delineate and define the full salt structure including the steep flanks. The defined salt boundaries can then be deployed in the reflectivity constraint as explained in Chapter 4 and also described by El Marhfoul and Verschuur (2017) to obtain the right migration velocities inside the salt body. Moreover, as can be seen from Figure 7.1 and based on the positioning of the BSD tool, the directed wavefield is propagating through the salt structure, which makes the one-way tomography of direct wavefield in the JMI process extremely sensitive to erroneous migration velocities inside the salt. All of this valuable information is exploited and reinforces one another in one integrated JMI process to define an optimum migration velocity model. The result of this process is depicted in Figure 7.6c, where a vertical slice is selected from the JMI updated model along the vertical black dashed line in Figure 7.8a that shows a depth slice from the true velocity model trough the salt structure. The comparison of the starting velocity model (Figure 7.6b) and the JMI updated one (Figure 7.6c) shows consistent updates with the true velocity model (Figure 7.6a) and follows nicely the overall velocity trend in 3D sense within the area which is adequately illuminated by the 3D BSD measurements.

In spite of the sparse acquisition geometry, at the borehole side, and the limited length of the BSD tool the 3D JMI algorithm was able to retrieve a significant velocity update, within a limited number of iterations, especially in areas where the ray paths are not affected by the mode converted waves around the salt structure. This is mainly because the multiple scattering and the downgoing wavefield are reinforcing the primary energy during the JMI process. Moreover, the one-way tomography of the directed wavefield is also integrated within the JMI process for an optimum and fast update of the salt structure around the borehole. Note that the estimated migration velocity of the salt structure is not yet at the right value of the true velocity model, as can be seen in Figure 7.6. This is mainly because this particular salt body is at the edge of the model and poorly illuminated by reflected energy and also covered only by small offset from the directed wavefield. Nevertheless, an effective migration velocity model is obtained that is explaining the reflected energy of the 3D BSD as much as possible.

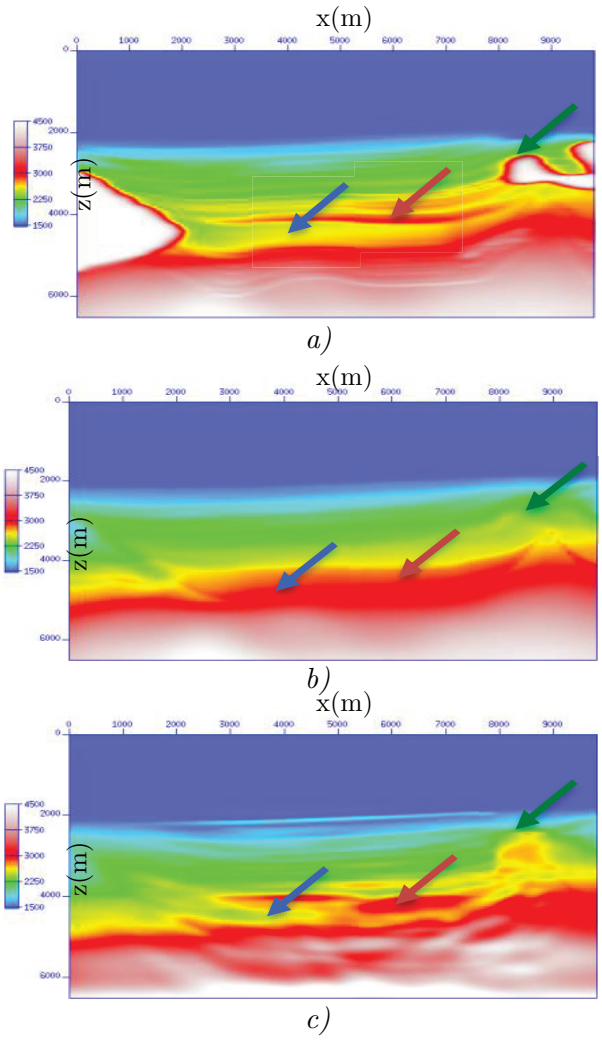

Figure 7.6: Vertical cross section of the JMI results. a) The true velocity model. b) The PSDM starting model. c) The JMI estimated model based on 3D elastic borehole data. Note the significant velocity update as is indicated by the arrows. The green arrow indicates the area which is also affected by the direct arrivals, the brown arrow indicates an area with velocity increase and the blue arrow indicates an area with velocity decrease consistent with the true velocity profile.

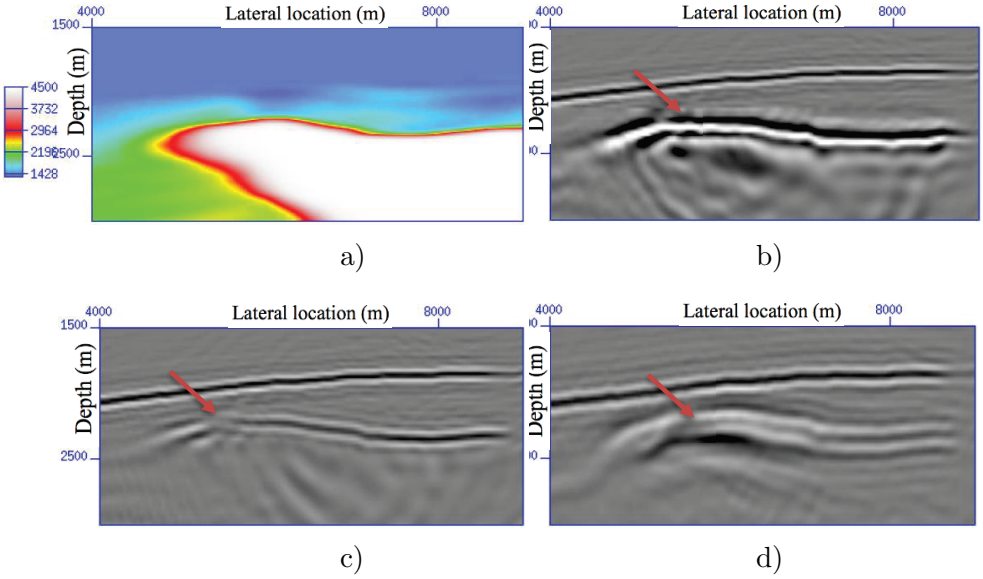

Figure 7.7: The effect of converted waves on the JMI inversion process. a) The true velocity model. b) The JMI estimated reflectivity image based on acoustic modelling of 3D borehole data. c) The JMI estimated image based on elastic modelling of 3D borehole data. d) The JMI estimated image based on elastic surface seismic data. Note the clear and proper delineation of the top of salt in picture b). However, strong destructive interference of the converted waves in picture c) and the strong cross-talk in picture d) are visible.

However, in areas close to the salt structure, the mode converted waves will produce strong crosstalk that will affect the velocity gradient. This is clearly visible in Figure 7.7c that shows a vertical slice from the reflectivity image along the yellow dashed line in Figure 7.8a. The reflectivity image, as displayed in Figure 7.7b, is free of crosstalk and a much better delineation of the salt boundaries is obtained when the second acoustic 3D BSD dataset is deployed in the JMI process. The effect of the mode converted waves, as can be seen in Figure 7.7d, is even more severe when imaging 3D surface seismic data. This is mainly because of the full fold distribution of the converted waves as opposed to the limited fold distribution in the 3D BSD.

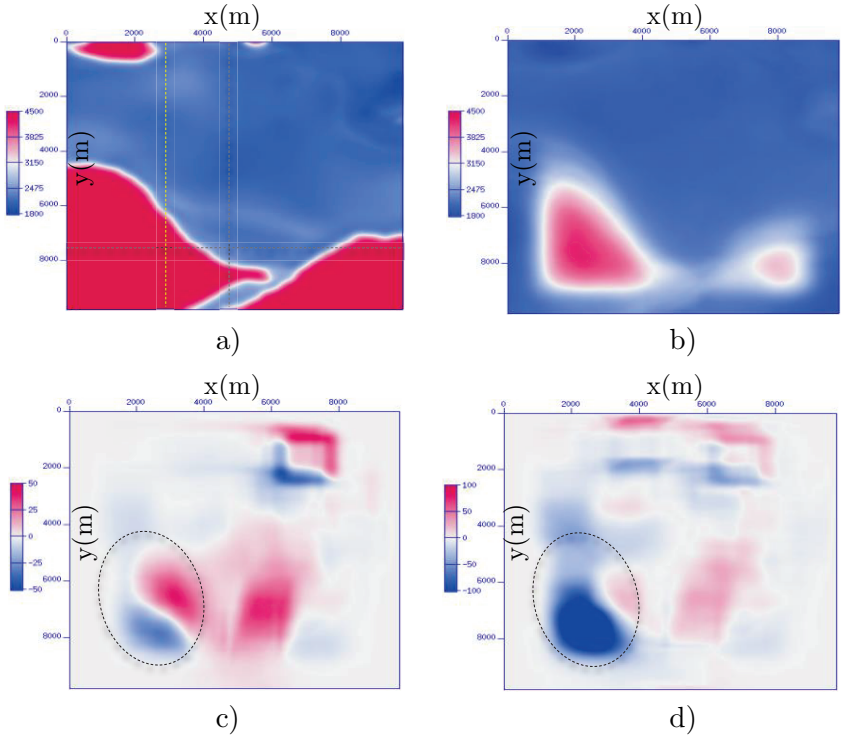

Figure 7.8: The effect of converted waves on the JMI velocity gradient. a) Depth slice of the true velocity model, the crossing point of the black dashed lines indicates the well location. b) Depth slice of JMI updated model by deploying the reflectivity constraint and including the direct wavefield in the inversion process. This model is then used as starting model for the JMI results in figure c) and d). Note that the initial PSDM model does not contain any salt information. c) Depth slice of the velocity gradient based on the 3D BSD acoustic dataset. d) Depth slice of the velocity gradient based on the 3D BSD elastic dataset. The oval shape indicates the area affected by the converted waves.

The acoustic implementation of the JMI algorithm will treat the mode converted waves as compressional waves and will try to explain them by updating the reflectivity image and the migration velocity model accordingly. This means that the velocity gradient will exhibit a wrong update, which is clearly noticeable in Figure 7.8d where the JMI algorithm has picked up the strong mode converted waves and will affect the final migration velocity model. This can be seen in the area indicated by the dashed oval in Figure 7.8d that shows a decrease in the migration velocities while they should be

increasing as indicated in Figure 7.8a.

7.4 Conclusions

In this chapter, the capability of the FWM algorithm in imaging and delineating steep events like salt flanks in a complex geological environment, based on 3D borehole data, is demonstrated. The full wavefield (primaries, multiples and downgoing wavefield) of 3D borehole data is deployed in one integrated process to produce the best estimate of the reflectivity image despite the sparse acquisition geometry of the 3D borehole data. The key factor is the preservation of the scattered energy from those salt flanks, which is usually destroyed during the separation of the up- and downgoing wavefield. Moreover, running the FWM process in an angle-dependent mode to produce CIP gathers clearly demonstrates the added value of utilizing the full wavefield in the 3D borehole data in providing additional reflection angles in areas beyond the coverage of the primary reflections. These CIP gathers are suitable input for conventional prestack elastic inversion algorithms to produce estimates of the subsurface properties and lithology.

In spite of the sparse acquisition geometry and the non-uniform fold distribution of the 3D borehole seismic data, the JMI algorithm is able to update the velocity model even far away from the well location, mainly because of the contribution from the multiple scattering and the downgoing wavefield. However, in areas with strong converted waves the acoustic implementation of the JMI algorithm might pick up the converted waves during updating the P-wave velocity model, resulting in wrong gradient direction. It is expected that this issue can be resolved by taking the converted waves into account in the the FWMod engine and utilizing them as well in the JMI algorithm. This might even improve the resolution of the obtained estimates of the reflectivity image and the migration velocity model.

Acknowledgement

The author thanks Total research center Pau for providing the simulated seismic datasets, their continuously support and the permission to publish this work.

8

Conclusions and recommendations

The accelerated energy transition that the world is currently undergoing, as an attempt to reduce and eventually annihilate man-caused CO_2 emission into the atmosphere, is posing substantial pressure not only on industrial organisations but on the whole society in general. Consequently, the scientific community in particular is also facing big challenges but at the same time great opportunities in answering the yet rising world's energy demand. Until the sustainable and renewable energy resources can sufficiently meet the world's energy demand, optimized management is required for the production of hydrocarbon-based fuels and the storage of their emitted CO_2 waste. This can be achieved by better understanding of the dynamics of the existing oil and gas reservoirs via continuous and advanced monitoring as was described in Chapter 6. Moreover, the injection of the industrial produced CO_2 into the deep geological formation is gaining more popularity as a mid-term storage solution. However, this puts even more emphasis on the need for continuous monitoring of the concerned area to ensure the sustainability and safety of this solution.

The methodology presented in this thesis shows that 3D BSD can effectively be utilized for the purpose of time-lapse imaging or even continuous monitoring of the subsurface reservoirs, especially when combined with full wavefield algorithms like FWM and JMI, such that the full signal in the

measured data can be exploited to extract as much as possible subsurface information. Moreover, the small volume-size of the 3D BSD surveys combined with modern acquisition techniques like DAS technology makes it a promising and attractive tool for permanent deployment. This provides us with a cost-efficient and good alternative for the conventional large 4D surface seismic surveys.

8.1 Conclusions

In this thesis we showed that the full potential of 3D borehole seismic data can be exploited by utilizing the full wavefield including all higher-order scatterings together with the deployment of imaging algorithms with a closed-loop architecture, like FWM and JMI. This is mainly because of the sparsity of the measured 3D borehole data at the borehole-side, where we usually have measurements only at a limited number of positions in the subsurface. It was shown that the FWM and JMI algorithms improve the non-uniform fold distribution at every imaging grid-point and increases the lateral extent of the image further away from the borehole. This is especially true for the case of a marine environment, where the surface multiples are significantly strong and the full signals measured in the 3D borehole data, including all multiple scatterings from both upgoing and downgoing wavefields, are utilized.

8.1.1 Obsoleteness of the separation of the up- and downgoing wavefields

One of the serious issues in conventional 3D BSD preprocessing is the separation of the up- and downgoing wavefields. This operation can cause the loss of valuable energy modes that are required for the delineation of steep events in the subsurface like in the case of complex salt environment with vertical salt flanks. This is mainly because the scattered energy from the salt flanks propagates in a more horizontal direction toward the receivers in the borehole. The FWMod algorithm, which is the backbone of the FWM and JMI algorithm, as described in Chapter 2, can simulate and model the full wavefield present in the seismic data including all higher-order scatterings. This means that the up- and downgoing wavefields of the 3D BSD will be automatically modelled at the same time, which makes the need for the traditional up/down separation obsolete. This was demonstrated in Chapter 4 with numerical and field data examples and in Chapter 7 the capability of the FWM algorithm in imaging vertical salt flanks was shown.

8.1.2 Capability of updating the migration velocities

In spite of the sparse acquisition geometry, the 3D JMI algorithm is able to provide reliable estimates of both the reflectivity image and the migration velocity model. This is mainly because the multiple scattering is improving the subsurface illumination and reinforcing the primary energy during the inversion process. Therefore, it adds significant value to the JMI inversion scheme and steers the algorithm towards more reliable solutions. Moreover, prior knowledge, like well logs, check-shot time-to-depth curves and geologic formation tops can be used as valuable constraints to the JMI inversion process, especially when dealing with datasets with sparse acquisition geometry. In addition, a major advantage of borehole-related data is the availability of the measured direct wavefield, which is used to estimate the source wavefield and also allows us to combine one-way tomography of the direct wavefield with reflection JMI of all orders of scattering simultaneously in order to update the velocity model and, therefore, have a more consistent and reliable solution for the migration velocity model. The 3D data examples presented in this thesis shows that 3D BSD can indeed provide reliable solutions for the reflectivity as well as the velocity model, with a lateral extent over quite an offset range, to provide high-resolution information that will be of great added value for reservoir illumination and characterization.

8.1.3 Integration of different seismic measurements

In this thesis, we have demonstrated the added value of the simultaneous deployment of different datasets, like 3D borehole with surface seismic data and multi-well 3D borehole data, in one JMI process. In the case of 3D borehole data, reciprocity is used by exchanging the sources and receivers positions 3D buried-shot records are obtained, with the "receivers" at source elevations and the "source" at the receiver depth. The JMI process is a shot-based algorithm meaning that all shot-gathers will adequately and evenly contribute to the inversion solutions, within their coverage area, as long as for every particular dataset the right source wavelet or wavefield is utilized and amplitude-balancing of both datasets with respect to each other is ensured. In spite of the sparse acquisition geometry, the 3D JMI algorithm is able to provide adequate estimate of the reflectivity image and migration velocity model, mainly because of the high angles available in the 3D borehole data and the contribution from the multiple scattering, including the downgoing wavefield. The numerical examples presented in this thesis show the effectiveness of the JMI approach, even in a complex geological environment, in retrieving the right kinematics properties from 3D borehole data and

translate it into proper velocity updates. It is demonstrated that integrating borehole data with surface seismic or simultaneously inverting datasets from different boreholes in one JMI process leads to improved images and propagation velocities, especially around the borehole.

Even though the demonstrated examples are assumed to represent only the vertical component of the 3D borehole seismic data, the integrated imaging approach of different seismic measurements, presented in this thesis, provides us also with an opportunity to simultaneously image multi-component 3D borehole and OBN datasets. It is expected that some conventional preprocessing steps, like the PZ summation in the case of OBN data, will become unnecessary and obsolete mainly because they will be handled automatically during the JMI inversion process.

8.1.4 Time-lapse imaging and continuous reservoir monitoring

The capability of the FWM algorithm to retrieve time-lapse image using 3D BSD is successfully demonstrated. Within the FWM framework, it is relatively straightforward to simultaneously invert the full wavefield including all high-order scattering from both up- and downgoing wavefields available in the 3D BSD measurements. In spite of the sparse acquisition geometry, the 3D FWM algorithm is able to provide reliable estimates of the reflectivity image and the time-lapse image. This is mainly because the multiple scattering is improving the subsurface illumination and reinforcing the primary energy during the inversion process. The 3D data example presented in this chapter shows that 3D BSD in combination with the FWM inversion-imaging algorithm can indeed provide reliable solutions and extend over quite an offset range, from the well trajectory, to provide high-resolution information that will be of great added value for reservoir characterization and monitoring. Moreover, it is expected to produce even more enhanced time-lapse results if all datasets from the different surveys are simultaneously deployed in imaging algorithms with a closed-loop architecture like FWM and JMI (Qu and Verschuur, 2021). This allows the baseline and the monitoring surveys to communicate and complement each other during the inversion process. Consequently, the non-repeatability uncertainties and the noise level in the final results will be reduced.

8.1.5 Angle-dependency and elastic effects

The capability of the FWM process to be executed in an angle-dependent mode to produce CIP gathers clearly demonstrates the added value of utilizing the full wavefield in the 3D borehole data in providing additional reflection angles in areas beyond the coverage of the primary reflections. It is expected that these CIP gathers are suitable input for conventional prestack elastic inversion algorithms to produce estimates of the subsurface properties and lithology.

Moreover, despite the sparse acquisition geometry and the non-uniform fold distribution of the 3D borehole seismic data, the JMI algorithm is able to update the velocity model even far away from the well location, mainly because of the contribution from the multiple scattering and the downgoing wavefield. However, in areas with strong converted waves the acoustic implementation of the JMI algorithm might pick up the converted waves during updating the P-wave velocity model, resulting in wrong gradient direction. It is expected that this issue can be resolved by taking the converted waves into account in the the FWMod engine and utilizing them as well in the JMI algorithm. This might even improve the resolution of the obtained estimates of the reflectivity image and the migration velocity model.

8.1.6 Outlook of 3D FWM and JMI for 3D seismic land data

Unlike the marine environment, where the surface-related multiples are strong, in the case of land seismic data the complex topography and the unconsolidated near surface, like what we encounter in the Middle East, will diffuse the total downgoing wavefield at the surface. This will result in weak and incoherent energy for the surface-related multiples. However, usually strong reflectors at the shallow part of the subsurface will cause internal multiples, which will create artifacts in the deep subsurface at the reservoir area. In other words, in the land seismic situation strong near-surface reflectors could act like the free surface in the case of marine data. This could offer an excellent opportunity for the FWM and JMI algorithm to utilize those internal multiples in the inversion-imaging process and map them into the right location in the subsurface. Even though the land data environment is very challenging, it is expected that adequate data preprocessing and the right strategies will ensure the success of the FWM and JMI algorithm to retrieve the right migration velocity model and consequently the right reflectivity image.

8.2 Recommendations for further research

Within the JMI algorithm, the modelled data is continuously compared to the measured data, after having updated the reflectivity and velocity model. By closing the loop in the inversion-imaging process and feeding back the residue to the JMI engine, an optimized reflectivity and migration velocity model will be obtained. This residue-driven process depends on the underlying assumption that some physical wave-phenomena, like the reflection coefficient angle-dependency, refracted and also mode-converted waves, are already removed in the preprocessing phase. Especially the JMI algorithm, where the migration velocities are being updated, is more sensitive to those wave-phenomena because they are not properly modelled and consequently not explained by the FWMod algorithm. Therefore, it is recommended to focus mainly on the kinematic effects when updating the migration velocities, especially at the early stage of the JMI inversion. This can be achieved by considering an objective function that does not look at the residue but rather maximises the cross-correlation between the modelled and observed data. In this way the emphasis will be on matching the phase of the seismic data and we can avoid the possibility that the JMI inversion process will be blocked by the complicated seismic amplitude effects. This process in schematically explained by the block diagram in Figure 8.1. It is expected that this will make the JMI inversion algorithm even more robust and steers it towards better estimates of the migration velocities, especially in the case of poor starting velocity model. As for the reflectivity update part, the residue should remain the driving force in suppressing the multiples and enhancing the resolution of the reflectivity image. Note that the reflectivity image can be updated in an angle-dependent mode, when the velocity model update is completed, to explain the angle-dependency effects (Davydenko and Verschuur, 2017).

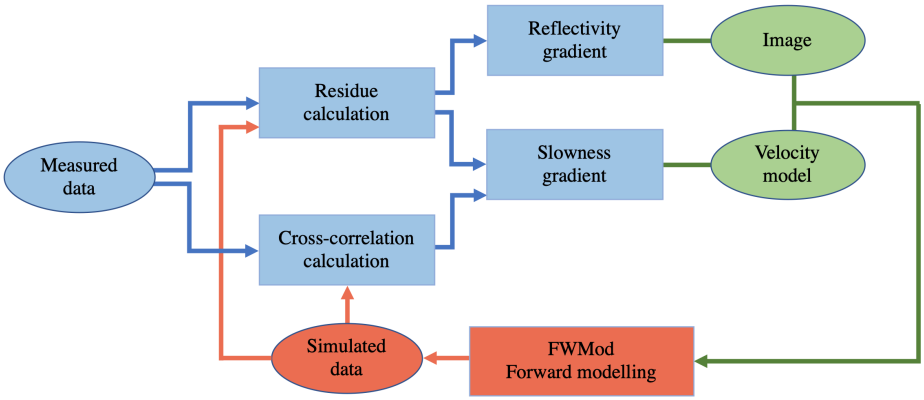

Figure 8.1: Block diagram explaining the extended inversion process of joint migration inversion. The modelled data is continuously compared to the input data after updating the model parameters, being the reflectivity image and the migration velocity model, in order to minimize the residue and/or maximize the cross-correlation between the modelled and observed data.

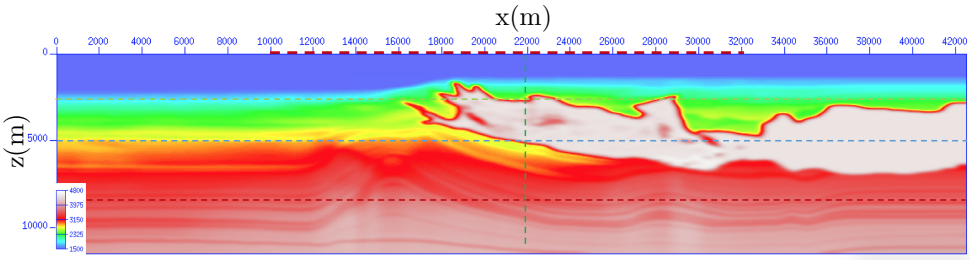

Figure 8.2: The Atlantis velocity model. Note the 'salt fingers' in the velocity model between lateral location 16000m and 22000m, they will cause a complicated diffraction pattern in the seismic data. The red dashed line indicates the source locations.

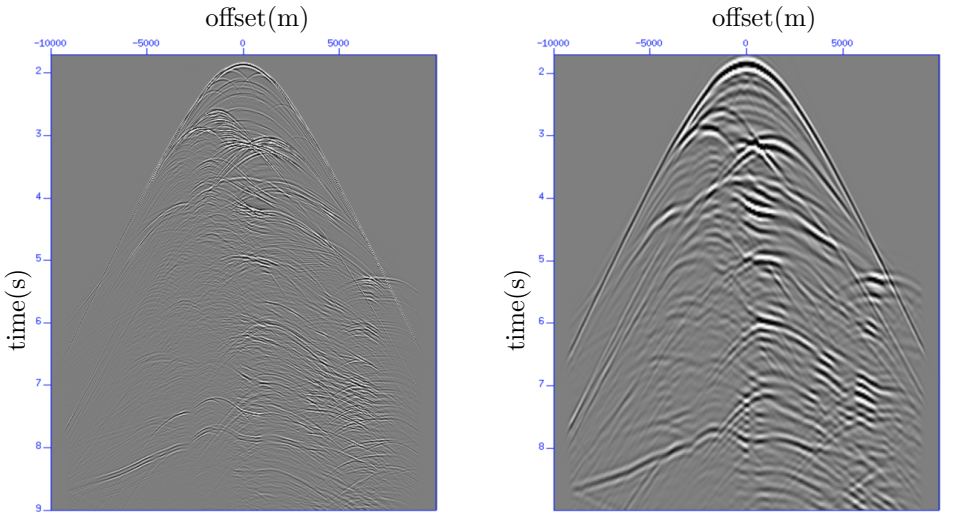

Figure 8.3: An example of a shot gather with the source location around the salt fingers. a) The shot gather with a maximum frequency of $60Hz$*. b) The shot gather with max frequency of* $10Hz$*. Note that the receivers are uniformly and densely distributed over the surface.*

8.2.1 Exploration of different objective functions

The combination of a residue-driven and cross-correlation based objective functions in one JMI algorithm seems to be an effective solution in handling datasets with deviant amplitude anomalies. This will be demonstrated for the Atlantis salt model as depicted in Figure 8.2, provided by BP. The model contains a complex salt structure with several 'salt fingers' embedded in a smooth sediment environment and is based on the actual Atlantis field in the Gulf of Mexico. $2D$ surface seismic data with split-spread geometry is simulated using the FWMod algorithm based on the true velocity and reflectivity models. The maximum offset in the data is $10km$ and the maximum frequency that is used in the JMI process is $10Hz$. Figure 8.3 shows an example of a shot record, located around the area of the salt structure, with complicated amplitude anomalies caused by the interference patterns from diffraction energy of the 'salt fingers'.

In order to compare the performance of the residue-driven versus the cross-correlation based JMI algorithm we have conducted four JMI experiments using the following frequency bandwidths $0-3Hz$ and $0-5Hz$ and based on the two different objective functions, as demonstrated in Figure 8.1. Note that the starting velocity model, in all four cases, is just a smooth $1D$ model

without any salt information (see Figure 8.7c), which is a challenging task for any inversion algorithm and requires the presence of low frequencies in order to be able to retrieve the salt structure. Figure 8.4a shows the difference between the true and initial velocity model.

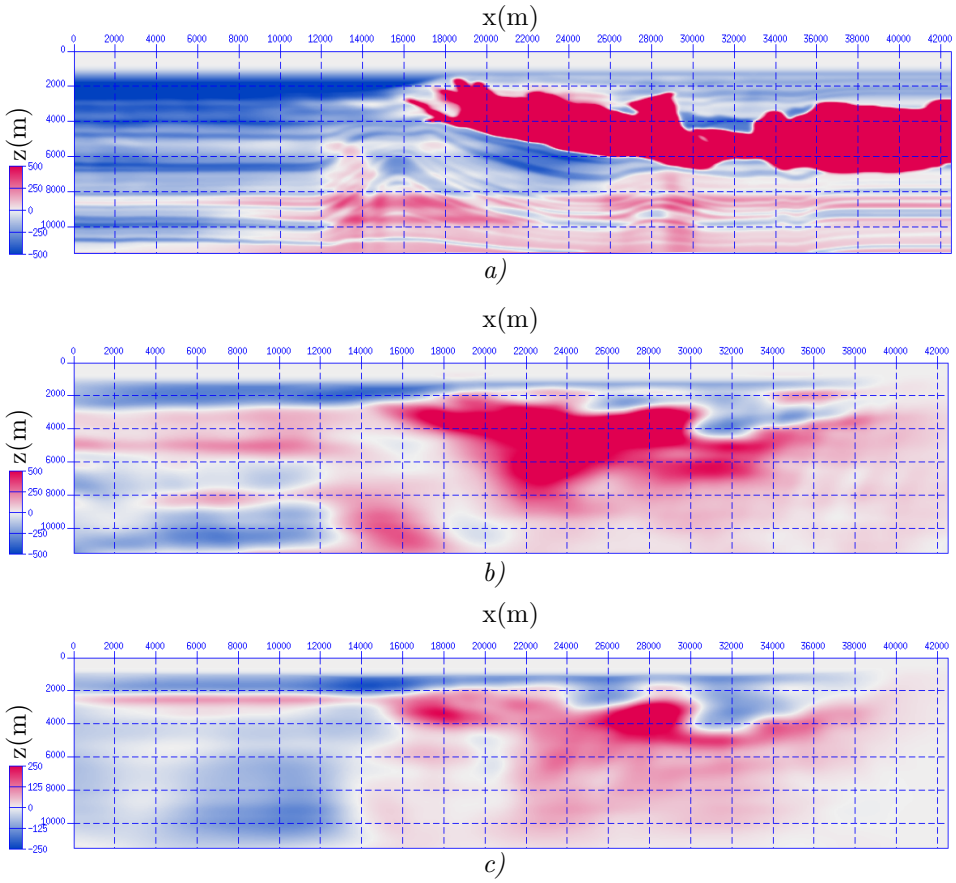

Figure 8.4: JMI results for the Atlantis velocity model with the complex salt structure and dataset with a maximum frequency of $3Hz$. a) The difference between the true and starting velocity model. b) JMI update using the cross-correlation based objective function, as explained in Figure 8.1. c) JMI update using the residue-driven objective function.

In Figure 8.4b,c JMI inversion results are depicted for the frequency bandwidth $0-3Hz$ after 10 iterations and using the same inversion parameters, for both objective functions, like the length of the smoothing operator and the illumination compensation, which are applied to the velocity gradient at every iteration. Note that, in general, both objective functions are recognis-

ing the water column (indicated with the blue color in Figure 8.4b,c) and also the salt structure (indicated with the red color in Figure 8.4b,c). However, the cross-correlation based objective function (8.4b) shows a more complete update of the migration velocities within and around the salt structure, where the complex diffractions will have a dominant and strong effect on the velocity gradient. This is also visible from the amplitude range of the migration velocities update as indicated by the color bars in Figure 8.4.

The effect of this update can also be seen in Figure 8.5, where a comparison between the modelled and residual data of both objective functions is displayed. In Figure 8.5a we see primary reflections with strong diffractions from the 'salt fingers' and Figure 8.5b shows the total wavefield including all higher-order of scatterings, which make the shot record even more complicated. The red arrow indicates a primary reflection, belonging to a the deepest reflector in the model, which is totally obscured by the higher-order scatterings in Figure 8.5b. The green arrow shows a primary diffraction in Figure 8.5a and on top of it a surface-related multiple in Figure 8.5b. The yellow arrows show surface related-multiples of diffracted energy on top of primary reflections. Figure 8.5c,d and Figure 8.5e,f display the JMI modelled and residual data for the cross-correlation-based and residue-driven objective functions respectively. Note the better fit of the events in the case of the cross-correlation objective function as indicated by the arrows. It can clearly be seen that the deep primary reflection indicated by the red arrow is better explained in Figure 8.5c,e than in Figure 8.5d,f. The same remarks are valid for the events of the green and yellow arrows. This is mainly because in the case of cross-correlation objective function the kinematics of the JMI modelled events are more consistent with the observed ones. We also observe overall lower residual amplitudes in Figure 8.5e compared to Figure 8.5f.

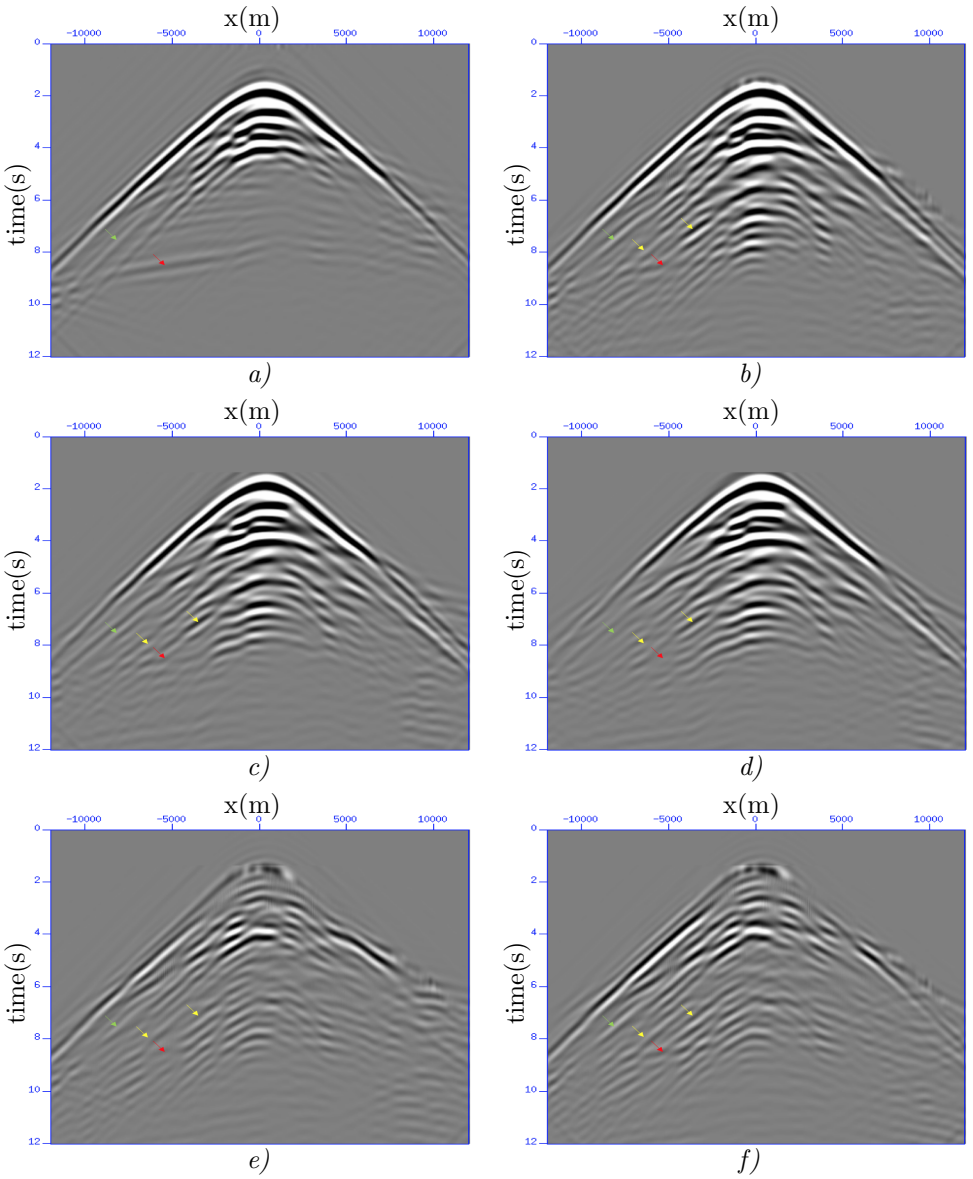

Figure 8.5: JMI results for the shot at lateral location $x = 18000m$. a) Primary reflections. b) The full wavefield. c) The JMI modelled data of the cross-correlation based objective function. d) The JMI modelled data of the residue-driven objective function. e) The residual data of the cross-correlation based objective function. f) The residual data of the residue-driven objective function.

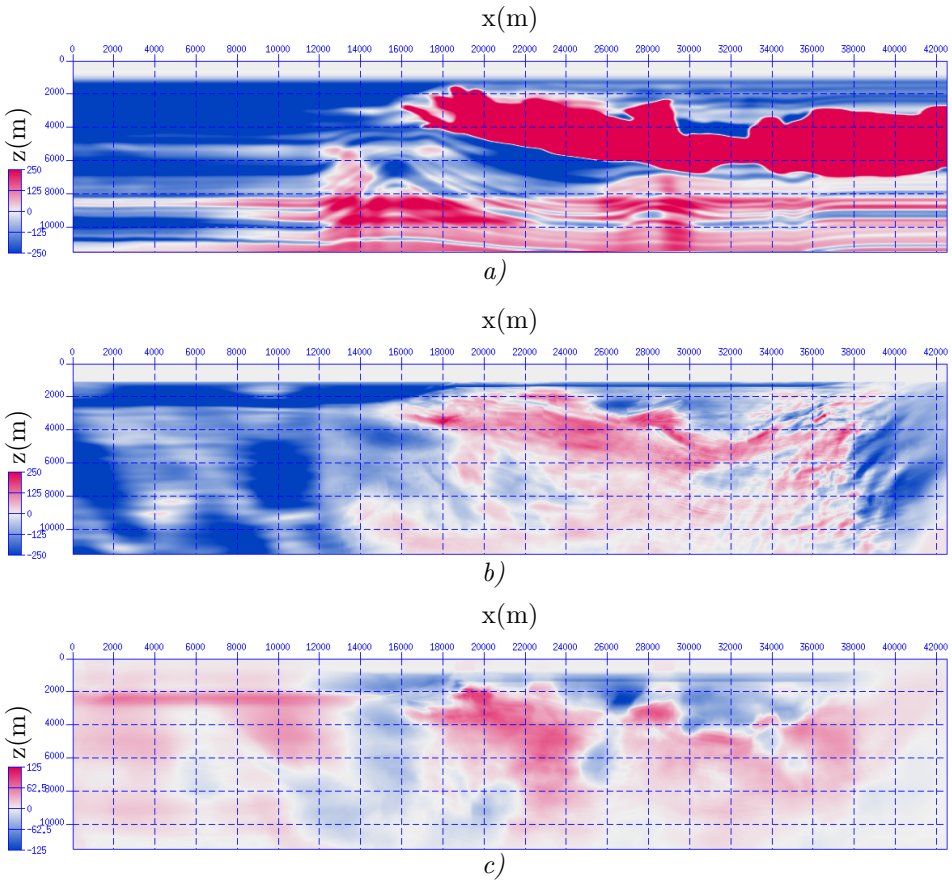

Figure 8.6: JMI results for the Atlantis velocity model with the complex salt structure and dataset with a maximum frequency of $5Hz$. a) The difference between the true and starting velocity model. b) JMI update using the cross-correlation based objective function, as explained in Figure 8.1. c) JMI update using the residue-driven objective function.

In the second case we have repeated the same JMI experiment with the same starting velocity model and the same inversion parameters as mentioned before. However, this time we have executed the JMI inversion process based on a broader frequency bandwidth of $0 - 5Hz$. This can provide us with better understanding of the robustness of the two objective functions, in producing the right velocity update, with respect to the effect of cycle skipping. In Figure 8.6 we can see the results of this experiment. It can now clearly be noticed that the cross-correlation based objective function is outperforming the residue-driven one and has successfully isolated the salt structure in the velocity model update within a limited number of iterations.

This is mainly because a better balance is obtained between all frequencies in this particular frequency bandwidth despite the complexity of the seismic data. The residue-driven objective function would in principle be able to produce correct migration velocities update if the output of the velocity update from the $0-3Hz$ experiment is deployed as starting model for the JMI inversion of the frequency bandwidth $0-5Hz$. In addition, it is expected that filtering diffraction energy from the seismic data, at least for the first few iterations, and focusing mainly on the reflected energy will help the JMI inversion scheme to produce the right velocity gradient.

On the other hand, it should be mentioned that in some areas the residue-driven objective function shows a more consistent update like what we see in Figure 8.4c around the lateral location $x = 34000m$. Therefore, it is expected to obtain a better solution, for the migration velocity model, by alternating between the two objective functions during the same JMI inversion process for the same and/or consequential frequency bandwidths. Note that in order to investigate how the two objective functions react on the effect of missing low frequencies we should totally remove the low frequency range from the data and, for instance, execute the JMI inversion process only for the frequency bandwidth $5-10Hz$. This will be then similar to what we usually encounter with field data situations.

Finally, in Figure 8.7 we see the results of a full JMI inversion process where we have deployed a combination of the cross-correlation based and residue-driven objective functions and we have also utilized the following consequential frequency bandwidths; $0-3Hz$, $0-5Hz$, $0-10Hz$. This means that the output from a lower frequency bandwidth is utilized as a starting velocity model for the next frequency bandwidth. The dashed brown line in Figure 8.7b,c indicates the source configuration that was utilized in the JMI process. Furthermore, for the sake of comparison we have also executed a FWM process using the true velocity model from Figure 8.7a and slightly limited sources configuration as indicated by the brown dashed line in Figure 8.7a. Note that we have deliberately limited the sources coverage area, in the right part of model, in order to comprehend the consequences of edge-effects on the velocity update and also the added value of the illumination from surface-related multiples at that part of the model. The obtained velocity update in Figure 8.7b compared to the starting velocity model (Figure 8.7c) shows consistent trends with the true velocity model (Figure 8.7a) and follows nicely the overall salt structure and sediment velocities. However, the area around the 'salt fingers' remains very challenging and still has significant inconsistency in the migration velocities. Also the subsalt area, where we

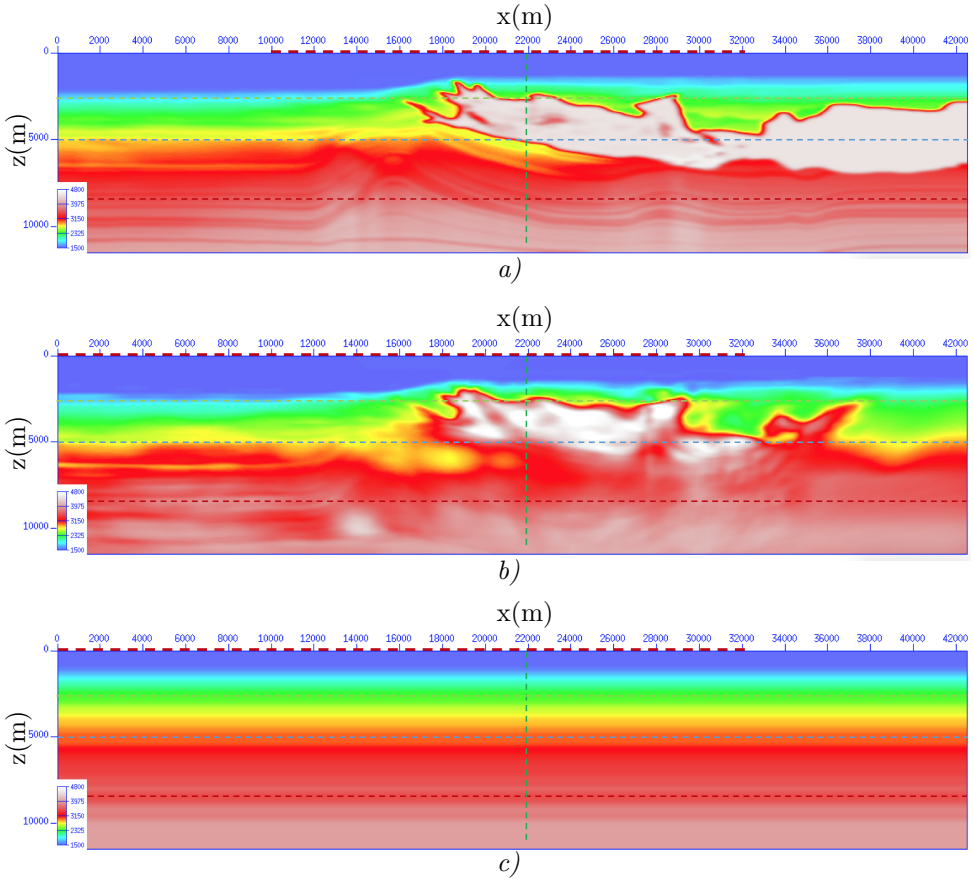

Figure 8.7: JMI results for the Atlantis velocity model using a dataset with a maximum frequency of $10Hz$*. a) The true velocity model. b) JMI updated model based on combined objective functions, as explained in Figure 8.1. c) The starting velocity model.*

have low sediment migration velocities in the true model, is very challenging to retrieve. This is because of the weak reflectivity of the subsalt reflectors as can be seen in Figure 8.8a, where we see the FWM reflectivity image using the true model from Figure 8.7a. One possible solution to even further fine tune the migration velocities is repeating the whole JMI inversion process with the current solution as a starting velocity model. Even though the current JMI updated velocity model is still slightly inaccurate around the salt structure area, its corresponding FWM reflectivity image, as can be seen in Figure 8.8b, exhibits adequate focusing and positioning of the subsurface reflectors even in the sub-salt area. Especially when compared with the FWM reflectivity image, as depicted in Figure 8.8c, based on the starting

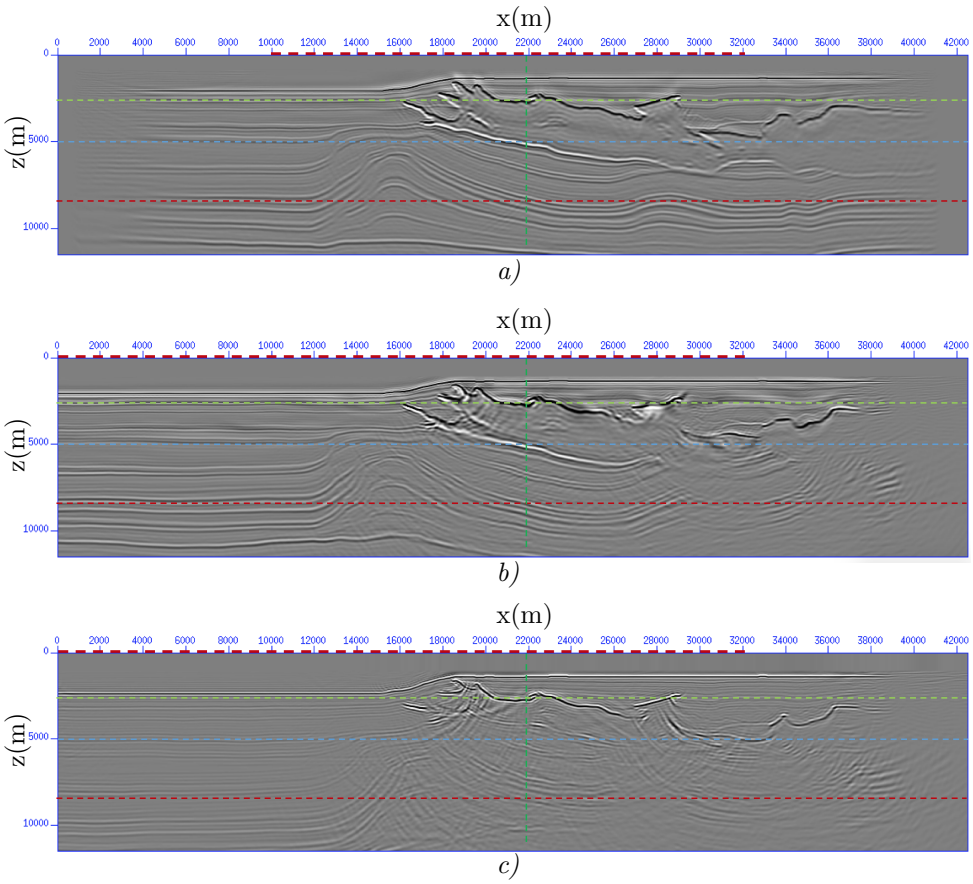

Figure 8.8: FWM results for the Atlantis velocity model using a dataset with a maximum frequency of $10Hz$*. a) FWM based on the true velocity model. b) FWM image based on the JMI updated model (Figure 8.7b). c) FWM image based on the starting velocity model (Figure 8.7c).*

velocity model from Figure 8.7c. This is visible from the consistency with the FWM image based on the true velocity model, which can be checked by the reference dashed lines. Moreover, the cross-talk from the higher-order scatterings cannot be explained in areas that are rich with diffraction energy in the case of wrong velocity model. This is visible in Figure 8.8c in the lateral interval [14000 22000] and also [26000 32000]. On the other hand the left part of the image in Figure 8.8c is cross-talk free up to lateral location $x = 12000m$ despite the wrong migration velocities, which makes the update of the migration velocities much easier for the JMI algorithm in that particular area.

8.2.2 Further assessment of the objective function based on finite difference modelled and field data

The challenges demonstrated in the previous section in the case of the Atlantis model, with complicated diffraction patterns, will become even more severe when dealing with finite difference modelled and field data where other complex wave-phenomena like the angle-dependent reflection coefficient, refracted and converted waves will come into play. Therefore, having a better understanding of all aspects of the JMI inversion algorithm, with their strengths and limitations, together with comprehending the complex wave-phenomena effects of the seismic data, will allow us to enhance the inversion process and consequently produce more accurate solutions for the migration velocities and reflectivity models of the subsurface. The objective function is a crucial component of every inversion algorithm, thus it can be expected that defining a suitable and consistent objective function with the presumed theory and honouring the algorithm assumptions, will result in more physically reliable estimates of the subsurface parameters.

8.2.3 Enhancement of subsurface illumination via wavefield synthesis

The adequate illumination of every grid point in the subsurface and specifically in the reservoir area is an essential aspect in seismic imaging and inversion processes in order to ensure satisfactory results. Conventionally the measured seismic data is fed into the imaging/inversion algorithms shot by shot to produce the desired subsurface parameters. However, it is expected that enhanced illumination of certain areas and structure in the subsurface can be obtained by abandoning the original point sources at the surface and transforming the measured seismic data into synthesised wavefields with predefined characteristics and parameters. This follows ideas already presented by Rietveld and Berkhout (1994).

There are two main examples of synthesised wavefields that can be investigated. The first one being plane waves decomposition, where the original point source wavefields and their corresponding response shot gathers are transformed into plane wave source wavefields with a specific illumination angle. This operation allows us to focus mainly on a certain range of illumination angles in order to reduce the emerging artifacts and thereby produce better imaging/inversion results.

The second potential example of synthesised wavefields, which can be used to enhance the subsurface illumination, is areal sources. In this case virtual

buried sources are created in the subsurface at strategically chosen positions. According to the Huygens' principle every grid point in the subsurface acts as a secondary source and scatters the incident wavefield in all directions. Therefore, an areal source can be seen as a superposition of time-delayed versions of all original sources at the surface toward the position of the areal source (Rietveld et al., 1992). Note that this operation is based on Green's functions, which are not required to be accurate because the same operation is applied to the response shot gathers. It is expected that areal sources can improve the effectiveness of the JMI inversion algorithm in areas with poor illumination or weak reflection energy like in the case of subsalt imaging.

8.2.4 Complementing the one-way with the two-way wave equation modelling algorithm

The FWMod engine, which is the backbone of the FWM and JMI algorithms, uses the phase shift operator to propagate the pressure wavefield between depth levels in the subsurface. This results in a computationally efficient mechanise especially when utilized in an iterative process like the FWM and JMI algorithms. However, the phase shift operator is based on the solution of the one-way wave equation, where the underlying assumption is the lateral homogeneity of the propagation velocities in the subsurface. As mentioned in Chapter 2, gentle lateral velocity variations can be handled by the PSPI algorithm. However, in the case of media with high lateral heterogeneity, the phase shift operator will produce erroneous propagation operators. This could be resolved by the deployment of a modelling algorithm based on the two-way wave equation but still utilizes the reflectivity and a background propagation velocity model as input parameters. Moreover, the angle limitation in the one-way wave equation engine of FWM/JMI can be circumvented, which will allow us to image extreme steep events and structures more adequately. Note that in order to reduce computational costs a hybrid algorithm -where the two-way wave equation modelling is deployed only in complex areas of the model- would be a more appropriate solution. There are already some successful first attempts in this direction (Davydenko and Verschuur (2020); Whitmore et al. (2020)), however more research is required to optimize this process.

8.2.5 Augmentation of full wavefield inversion algorithms

Like the integration of different types of seismic data, or even no-seismic measurements like electromagnetic data, the integration of different inversion

algorithms like JMI and FWI is expected to provide an even more accurate solution of the subsurface parameters. Since both algorithms are aiming at minimizing the residual between the observed measurements and the modelled data, by following different approaches and also dealing with different parts of the seismic data, combining them in one inversion scheme will ensure that they can complement each other to overcome their flaws and maybe even enhance their supremacies. This is mainly because of the fact that being able to explain the seismic data does not necessarily guarantee that we do have the right solution. This means that an estimate that is constrained by both methodologies is a more reliable and robust one. There are already some first successful attempts made in this direction where the process of combining the inversion of diving waves using FWI with reflection energy modes by deploying the JMI algorithm is demonstrated (Davydenko and Verschuur (2019); Eisenberg et al. (2019)).

Acknowledgement

The author would like to thank BP research center Houston for providing the Atlantis model and the insightful discussions together with their continuously support.

Appendices

A

The differential formulation of the pressure wavefield

A.1 The two-way acoustic wave equation

The wave processes associated with the propagation of sound waves in the subsurface are mainly described by the wave equation, which is the backbone of the study of wave phenomena and is widely used in the simulation of seismic data. In this section, we derive the acoustic wave equation in inhomogeneous media, starting from Newton's and Hooke's Laws. Newton's Law in inhomogeneous acoustic media states (see e.g. Gisolf and Verschuur, 2010):

$$\vec{f}(\vec{r},t) - \nabla p(\vec{r},t) = \rho(\vec{r})\frac{\partial \vec{v}(\vec{r},t)}{\partial t}, \tag{A.1}$$

where $\vec{f}(\vec{r},t)$ is the external force per unit volume, $p(\vec{r},t)$ is the pressure variation relative to the static pressure p_0, $\vec{v}(\vec{r},t)$ is the particle velocity variation and $\rho(\vec{r})$ is the space variant static density. Hooke's Law in inhomogeneous acoustic media states:

$$\nabla \cdot \vec{u}(\vec{r},t) = -\frac{p(\vec{r},t)}{\kappa(\vec{r})} + Q(\vec{r},t), \tag{A.2}$$

where $Q(\vec{r},t)$ is the source injected volume per unit volume, $\vec{u}(\vec{r},t))$ is the particle displacement vector and $\kappa(\vec{r})$ is the space variant static compression modulus (Elmore and Heald, 1985). For the rate of change of Hooke's law we get:

$$\nabla \cdot \vec{v}(\vec{r},t) + \frac{1}{\kappa(\vec{r})}\frac{\partial p(\vec{r},t)}{\partial t} = q(\vec{r},t), \tag{A.3}$$

where $q(\vec{r},t) = \dfrac{\partial Q(\vec{r},t)}{\partial t}$ is the source volume injection rate per unit volume. Combining Newton's Law and Hooke's Law for the rate of change, produces the acoustic wave equation in inhomogeneous acoustic media:

$$\rho(\vec{r})\nabla \cdot \{\frac{1}{\rho(\vec{r})}\nabla p(\vec{r},t)\} - \frac{1}{c^2(\vec{r})}\frac{\partial^2 p(\vec{r},t)}{\partial t^2} = -s(\vec{r},t), \tag{A.4}$$

with $c(\vec{r}) = \sqrt{\frac{\kappa(\vec{r})}{\rho(\vec{r})}}$ and $s(\vec{r},t) = \rho(\vec{r})\{\dfrac{\partial q(\vec{r},t)}{\partial t} - \nabla \cdot \{\frac{1}{\rho(\vec{r})}\vec{f}(\vec{r},t)\}\}$.
The acoustic wave equation in inhomogeneous media does not have an analytical solution and is usually solved via a finite difference method by discretizing the solution domain and taking linear approximations of the derivatives in the wave equation (Aoi and Fujiwara, 1999). In a homogeneous medium, which means that the density distribution function ρ is independent of $\vec{r}$, the acoustic wave equation becomes:

$$\nabla^2 p(\vec{r},t) - \frac{1}{c^2}\frac{\partial^2 p(\vec{r},t)}{\partial t^2} = -s(\vec{r},t), \tag{A.5}$$

with $c = \sqrt{\frac{\kappa}{\rho}}$ and $s(\vec{r},t) = \rho\dfrac{\partial q(\vec{r},t)}{\partial t} - \nabla \cdot \vec{f}(\vec{r},t)$.
We can transform the source-free wave equation in a homogeneous medium to the frequency domain:

$$\nabla^2 P(\vec{r},\omega) + \frac{\omega^2}{c^2}P(\vec{r},\omega) = 0, \tag{A.6}$$

where capitals now denote quantities that are Fourier transformed with respect to time. This second-order differential equation is known as the Helmholtz equation (see e.g. Erlangga et al., 2004) and is satisfied by the following analytical solution:

$$P(\vec{r},\omega) = W(\omega)e^{-i\omega\vec{s}\cdot\vec{r}}, \tag{A.7}$$

where $\vec{s}$ is the slowness vector with $s_x^2 + s_y^2 + s_z^2 = \dfrac{1}{c^2}$ and $W(\omega)$ is the frequency-dependent amplitude spectrum of the solution. These solutions

are called plane waves and in the time domain can be written as follows:

$$p(\vec{r},t) = w(t - \vec{s}\cdot\vec{r}), \tag{A.8}$$

where $w(t)$ is the temporal inverse Fourier transform of the function $W(\omega)$. A triple spatial Fourier transform of equation A.7 to the k_x, k_y, k_z domain will produce the following solution:

$$P(\vec{k},\omega) = (2\pi)^3 W(\omega)\delta(\vec{k} - \omega\vec{s}). \tag{A.9}$$

This means that for one frequency a 3D plane wave can be represented by one non-zero element in the triple spatial Fourier transform domain.

In the case of a physical experiment, where a point-source of the mass injection type is deployed at position $\vec{r}_{src}$, the source term from equation A.4 becomes:

$$s(\vec{r},t) = \rho\frac{\partial q(\vec{r},t)}{\partial t} = w(t)\delta(\vec{r} - \vec{r}_{src}), \tag{A.10}$$

where $w(t)$ is the source signature, or source wavelet, inserted at position $\vec{r}_{src}$. The two-way wave equation then becomes:

$$\nabla^2 p(\vec{r},t) - \frac{1}{c^2}\frac{\partial^2 p(\vec{r},t)}{\partial t^2} = -w(t)\delta(\vec{r} - \vec{r}_{src}). \tag{A.11}$$

Applying the temporal Fourier transform to this wave equation produces the Helmholtz equation with an additional source term:

$$\nabla^2 P(\vec{r},\omega) + \frac{\omega^2}{c^2}P(\vec{r},\omega) = -W(\omega)\delta(\vec{r} - \vec{r}_{src}). \tag{A.12}$$

This equation can be solved in the wave number domain by triple spatial Fourier transformation:

$$(-k_x^2 - k_y^2 - k_z^2)\vec{P}(\vec{k},\omega) + \frac{\omega^2}{c^2}\vec{P}(\vec{k},\omega) = -W(\omega)e^{i\vec{k}\cdot\vec{r}_{src}}, \tag{A.13}$$

This means that (see e.g. Gisolf and Verschuur, 2010):

$$\vec{P}(\vec{k},\omega) = -\frac{W(\omega)e^{i\vec{k}\cdot\vec{r}_{src}}}{\frac{\omega^2}{c^2} - k_x^2 - k_y^2 - k_z^2}. \tag{A.14}$$

By applying the triple spatial inverse Fourier transformation, we get:

$$\vec{P}(\vec{r},\omega) = W(\omega)\frac{e^{\pm i\frac{\omega}{c}\Delta r}}{4\pi\Delta r}, \tag{A.15}$$

where $\Delta r = |\vec{r} - \vec{r}_{src}|$. Considering only the causal solution in equation A.15 and assuming that the source is located at the origin $x = y = 0$, applying the double spatial Fourier transformation to the (k_x, k_y) domain gives:

$$\tilde{P}(k_x,k_y,z,\omega) = -\frac{1}{2}iW(\omega)\frac{e^{-i\Delta z\sqrt{\frac{\omega^2}{c^2}-k_x^2-k_y^2}}}{\sqrt{\frac{\omega^2}{c^2}-k_x^2-k_y^2}}. \tag{A.16}$$

where $\Delta z = |z - z_{src}|$. In the area where $k_z^2 = (\frac{\omega^2}{c^2} - k_x^2 - k_y^2) < 0$, the pressure wavefield $\vec{P}(k_x, k_y, z, \omega)$ exhibits exponential decay as function of Δz and it is therefore not possible to measure this field far away from the source location. This is called the evanescent part of the wavefield and is caused by the fact that we are considering measurements of a spherical wavefield along a flat cross-section in the x, y plane at constant z. The issue of the evanescent energy will disappear if we consider measurements along a spherical surface.

A.2 The one-way wave equation for plane waves

In order to calculate the particle velocity field that corresponds to the plane wave solution, we use the time Fourier transformed version of Newton's Law, equation A.1:

$$-\nabla P(\vec{r},\omega) = i\omega\rho\vec{V}(\vec{r},\omega). \tag{A.17}$$

Filling in the plane wave solution, equation A.7, for P results in:

$$\vec{V}(\vec{r},\omega) = (s_x, s_y, s_z)^T\frac{1}{\rho}P(\vec{r},\omega). \tag{A.18}$$

When we consider only the z-component of $\vec{V}(\vec{r},\omega)$, we obtain:

$$V_z^{\pm}(\vec{r},\omega) = \pm\frac{|s_z|}{\rho}P^{\pm}(\vec{r},\omega), \tag{A.19}$$

where $P^+(\vec{r},\omega)$ indicates a plane wave propagating in the positive z-direction and $P^-(\vec{r},\omega)$ is a plane wave propagating in the negative z-direction, both with the same slowness $|s_z| = \sqrt{\frac{1}{c^2} - s_x^2 - s_z^2}$. Combining this with the z-component of Newton's Law from equation A.17 in the (k_x, k_y, z, ω) domain ($\frac{\partial P}{\partial z} = -i\omega\rho V_z$), we obtain the one-way wave equations for plane waves:

$$\frac{\partial P^+}{\partial z} + i\omega s_z P^+ = 0 \quad , \quad \frac{\partial P^-}{\partial z} - i\omega s_z P^- = 0. \tag{A.20}$$

The solution of these one-way wave equations is as follows:

$$P^{\pm}(k_x, k_y, z, \omega) = P^{\pm}(k_x, k_y, 0, \omega) e^{\mp i\omega s_z z}. \tag{A.21}$$

With this derivation, the two-way wavefield $P(k_x, k_y, z, \omega)$ is decomposed into two one-way wavefields P^+ and P^-, obeying the one-way wave equations. The problem of solving one second-order differential equation is reduced to the problem of solving two first-order differential equations. This means that if the propagation direction of a wavefield is known, the appropriate one-way wave equation from equation A.20 can be used.

Bibliography

Aaron, P., O'Toole, R., Barnes, S., Hegge, R. F., and van Borselen, R. G. (2008). True-azimuth versus zero-azimuth 3-D multiple prediction in WATS processing. pages 2431–2435, Las Vegas. SEG, Soc. Expl. Geophys., Expanded abstracts.

Ahmad, J., El Marhfoul, B., and Owusu, J. (2012). Pre-stack VSP elastic inversion for lithology delineation in an offshore field of the arabian gulf, saudi arabia. Istanbul. EAGE, Eur. Ass. of Geosc. and Eng., Expanded abstracts.

Al Bannagi, M. S., El Marhfoul, B., and Verschuur, D. J. (2018). Joint velocity model building and high-resolution depth imaging of full wavefield 3D VSP data. Anaheim. Soc. Expl. Geophys., Expanded abstracts.

Al Dulaijan, K., Owusu, J. ., and Weber, D. . (2012). Azimuthal anisotropy analysis of walkaround vertical seismic profiling vertical seismic profiling: a case study from saudi arabia. *Geophysical Prospecting*, 60(6):1082–1094.

Alai, R. and Verschuur, D. J. (2006). Case study of surface related and internal multiple elimination on land data. pages 2727–2731. SEG, Soc. Expl. Geophys., Expanded abstracts.

Alkhalifah, T. (2000). An acoustic wave equation for anisotropic media. *Geophysics*, 65(4):1239–1250.

Alkhalifah, T. and Tsvankin, I. (1995). Velocity analysis for transversely isotropic media. *Geophysics*, 60(5):1550–1566.

Alshuhail, A. A. (2017). *Anisotropic Joint Migration Inversion: Automatic estimation of refelctivities and anisotropic velocities.* PhD thesis, Delft University of Technology.

Aoi, S. and Fujiwara, H. (1999). 3 D finite-difference method using discontinuos grids. *Bulletin of the Seismolocigal Society of America*, 89(4):918–930.

Araujo, F. V., Weglein, A. B., Carvalho, P. M., and Stolt, R. H. (1994). Inverse scattering series for multiple attenuation: an example with surface and internal multiples. pages 1039–1041, Los Angeles. SEG, Soc. Expl. Geophys., Expanded abstracts.

Banik, N. C. (1984). Velocity anisotropy of shales and depth estimation in the North Sea basin. *Geophysics*, 49(9):1411–1419.

Baysal, E., Kosloff, D. D., and Sherwood, J. W. C. (1983). Reverse timemigration. *Geophysics*, 48(11):1514–1524.

Behura, J., Wapenaar, K., and Snieder, R. (2012). Newton-marchenkorose imaging. pages 1–6, Las Vegas. SEG, Soc. Expl. Geophys., Expanded abstracts.

Berkhout, A. J. (1982). *Seismic migration, imaging of acoustic energy by wave field extrapolation, A: theoretical aspects.* Elsevier (second edition).

Berkhout, A. J. (2012). Combining full wavefield migration and full waveform inversion, a glance into the future of seismic imaging. *Geophysics*, 77:S43–S50.

Berkhout, A. J. (2014a). Review paper: An outlook on the future of seismic imaging, Part I: forward and reverse modelling. *Geoph. Prosp.*, 62(5):911–930.

Berkhout, A. J. (2014b). Review paper: An outlook on the future of seismic imaging, Part II: Full-wavefield migration. *Geoph. Prosp.*, 62(5):931–949.

Berkhout, A. J. (2014c). Review paper: An outlook on the future of seismic imaging, Part III: Joint migration inversion. *Geoph. Prosp.*, 62(5):950–971.

Berkhout, A. J. and Blacquière, G. (2014). Combining deblending with multi-level source deghosting. pages 41–45, Denver. SEG, Soc. Expl. Geophys., Expanded abstracts.

Berkhout, A. J. and Verschuur, D. J. (1994). Multiple technology, Part 2: Migration of multiple reflections. pages 1497–1500, Los Angeles. SEG, Soc. Expl. Geophys., Expanded abstracts.

Berkhout, A. J. and Verschuur, D. J. (1997). Estimation of multiple scattering by iterative inversion, part I: theoretical considerations. *Geophysics*, 62(5):1586–1595.

Berkhout, A. J. and Verschuur, D. J. (1999). Removal of internal multiples. pages 1334–1337, Houston. SEG, Soc. Expl. Geophys., Expanded abstracts.

Berkhout, A. J. and Verschuur, D. J. (2011). A scientific framework for active and passive seismic imaging, with applications to blended data and micro-earthquake responses. *Geophys. J. Int.*, 184(2):777–792.

Berkhout, A. J., Verschuur, D. J., and Staal, X. R. (2015). Integration of velocity estimation and nonlinear migration. pages 5233–5237, New Orleans. SEG, Soc. Expl. Geophys., Expanded abstracts.

Biondi, B. and Shan, G. (2002). Prestack imaging of overturned reflections by reverse time migration. pages 1284–1287. SEG, Soc. Expl. Geophys., Expanded abstracts.

Biondi, B. and Symes, W. (2004). Angle-domain common-image gathers for migration velocity analysis by wavefield continuation imaging. *Geophysics*, 69:1283–1298.

Blias, E. and Hughes, B. (2015). 3D VSP imaging: general problems. pages 5630–5635, New Orleans. SEG, Soc. Expl. Geophys., Expanded abstracts.

Born, M. and Wolf, E. (1980). *Principles of optics electromagnetic theory of propagation interference and diffraction of light.* Pergamon Press, Inc.

Bremmer, H. (1951). The W.K.B. approximation as the first term of a geometric-optical series. *Comm. Pure Appl. Math.*, 4(1):105–115.

Byun, B. S., Gorrigan, D., and Gaiser, J. E. (1989). Anisotropic velocity analysis for lithology discrimination. *Geophysics*, 54(12):1564–1574.

Claerbout, J. F. (1976). *Fundamentals of geophysical data processing.* McGraw-Hill.

Claerbout, J. F. (1985). *Imaging the earth's interior.* Blackwell Scientific Publications.

Davydenko, M. (2016). *Full wavefeild migration: Seismic imaging using multiple scattering effects.* PhD thesis, Delft University of Technology.

Davydenko, M. and Verschuur, D. J. (2013). Full wavefield migration, using internal multiples for undershooting. pages 3741–3745, Houston. SEG, Soc. Expl. Geophys., Expanded abstracts.

Davydenko, M. and Verschuur, D. J. (2015). Full wavefield migration for sparsely sampled 3D data. pages 4206–4210, New Orleans. SEG, Soc. Expl. Geophys., Expanded abstracts.

Davydenko, M. and Verschuur, D. J. (2017). Full-wavefield migration: using surface and internal multiples in imaging. *Geophysical Prospecting*, 65(1):7–21.

Davydenko, M. and Verschuur, D. J. (2019). Using the full wavefield both in FWI & wavefield tomography. pages 1239–1243, Houston. SEG, Soc. Expl. Geophys., Expanded abstracts.

Davydenko, M. and Verschuur, D. J. (2020). Including internal multiples from the estimated image in least-squares reverse-time migration. page 2928–2932. SEG, Soc. Expl. Geophys., Expanded abstracts.

Davydenko, M., Verschuur, D. J., and Berkhout, A. J. (2014). Omnidirectional extension of Full Wavefield Migration. pages 2447–2450, Amsterdam. EAGE, Eur. Ass. of Geosc. and Eng., Expanded abstracts.

de Bruin, C. G. M. (1992). *Linear AVO inversion by prestack depth migration.* PhD thesis, Delft University of Technology.

de Hoop, M. V. (1996). Generalization of the Bremmer coupling series. *J. Math. Phys.*, 37(7):3246–3282.

Eisenberg, G., Schuenemann, E., Gierse, G., Verschuur, D. J., and Qu, S. (2019). Robust velocity estimation via joint migration inversion and full waveform inversion. pages 1224–1228, Houston. SEG, Soc. Expl. Geophys., Expanded abstracts.

El Marhfoul, B. and Verschuur, D. J. (2014). 3D joint full wavefield migration of surface and VSP data. pages 5070–5074, Denver. SEG, Soc. Expl. Geophys., Expanded abstracts.

El Marhfoul, B. and Verschuur, D. J. (2015). 3D full wavefield imaging of up and down-going VSP data. pages Tu–N118–10, Madrid. EAGE, Eur. Ass. of Geosc. and Eng., Expanded abstracts.

El Marhfoul, B. and Verschuur, D. J. (2017). 3D reflectivity-guided joint migration inversion of multi-well borehole data. Abu Dhabi. EAGE, Eur. Ass. of Geosc. and Eng., Expanded abstracts.

El Marhfoul, B. and Verschuur, D. J. (2019). Potential and challenges of 3D joint migration inversion of 3D borehole and surface seismic data. pages 1–5, The Hague. EAGE, Eur. Ass. of Geosc. and Eng., Expanded abstracts.

Elmore, W. C. and Heald, M. A. (1985). *Physics of Waves*. Dover, Publications, Inc., New York.

Erlangga, Y. A., Vuik, C., and Oosterlee, C. W. (2004). On a class of preconditioners for solving the Helmholtz equation. *Applied Numerical Mathematics*, 50(3-4):409–425.

Fei, T. W. and Liner, C. L. (2008). Hybrid fourier finite-difference 3D depth migration for anisotropic media. *Geophysics*, 73(2):S27–S33.

Futterman, W. I. (1962). Dispersive body waves. *Journal of Geophysics Research*, 67(13):5279–5291.

Gao, K., Huang, L., and Cladouhos, T. (2021). Three-dimensional seismic characterization and imaging of the soda lake geothermal field. *Geothermics*, 90:101996.

Gazdag, J. and Sguazzero, P. (1984). Migration of seismic data by phase shift plus interpolation. *Geophysics*, 49(2):105–203.

Gerea, C., Pichon, P. L., Verliac, M., and Lesnikov, V. (2016). Proficient subsalt monitoring with 3D well seismic, deep-offshore west africa. pages 688–692, Dallas. SEG, Soc. Expl. Geophys., Expanded abstracts.

Gisolf, A. and Verschuur, D. J. (2010). *The principles of quantitative acoustical imaging*. EAGE publications bv.

Haase, A. . and Stewart, R. . (2003). Q-factor estimation from borehole seismic data: Ross Lake, Saskatchewan. *CREWES Research Report*, 15.

Hammad, H. I. and Verschuur, D. J. (2018). Generalized full wavefield modeling: Beyond neumann. EAGE, Eur. Ass. of Geosc. and Eng., Expanded abstracts.

Hardage, B. A. (1985). *Vertical seismic profiling, part A: prinicples*. Geophysical Press.

House, N. J., Fuller, B., Behrman, D., and Allen, K. P. (2008). Acquisition, processing and iterpretation of a very large 3D VSP using new technologies: Risks tradeoffs and rewards. pages 3360–3364, Las Vegas. SEG, Soc. Expl. Geophys., Expanded abstracts.

Irabor, K. and Warner, M. (2016). Reflection fwi. pages 1136–1140, Dallas. SEG, Soc. Expl. Geophys., Expanded abstracts.

Kalita, M., Kazei, V., Choi, Y., and Alkhalifah, T. (2019). Regularized full-waveform inversion with automated salt-flooding. *GEOPHYSICS*, 84:1–74.

Keys, R. G. and Weglein, A. B. (1983). Generalized linear inversion and the first born theory for acoustic media. *Journal of Mathematical Physics*, 246:1444–1449.

Kinneging, N. K., Budejicky, V., Wapenaar, C. P. A., and Berkhout, A. J. (1989). Efficient 2D and 3D shot record redatuming. *Geophys. Prosp.*, 37(5):493–530.

Kosloff, D., Sherwood, J., Koren, Z., MacHet, E., and Falkovitz, Y. (1996). Velocity and interface depth determination by tomography of depth migrated gathers. *Geophysics*, 61(5):1511–1523.

Leaney, W. S. (2015). Ava from prestack 3D VSP images. Calgary. GeoConvention.

Li, Y. and Hewett, B. (2016). Refelction salt proximity. *First Break*, 34:33–39.

Li, Y., Wong, W., Hewett, B., Liu, Z., Mateeva, A., and Lopez, J. (2015). Velocity analysis and update with 3D DAS VSP to improve borehole/surface seismic images. pages 5285–5289. SEG, Soc. Expl. Geophys., Expanded abstracts.

Lomask, J., Biondi, B., and Shragge, J. (2004). Image segmentation for tracking of salt boundaries. pages 2443–2342, Denver. SEG, Soc. Expl. Geophys., Expanded abstracts.

Lu, S., Whitmore, N. D., Valenciano, A. A., and Chemingui, N. (2011). Imaging of primaries and multiples with 3D SEAM synthetic. pages 3217–3221, San Antonio. SEG, Soc. Expl. Geophys., Expanded abstracts.

Lumley, D., Adams, D. C., Meadows, M., Cole, S., and Wright, R. (2003). 4D seismic data processing issues and examples. pages 1394–1397, Dallas. SEG, Soc. Expl. Geophys., Expanded abstracts.

Lynn, W., Gonzalez, A., and Mackay, S. (1991). Where are the fault-plane refelctions? pages 1151–1154, Dallas. Soc. Expl. Geophys., Expanded abstracts.

Malcolm, A. E., Ursin, B., and de Hoop, M. V. (2009). Seismic imaging and illumination with internal multiples. *Geophysical Journal International*, 176(3):847–864.

Martuganova, E., Stiller, M., Bauer, K., Henninges, J., and Krawczyk, C. M. (2021). Cable reverberations during wireline distributed acoustic sensing measurements: their nature and methods for elimination. *Geophysical Prospecting*, (69):1034 – 1054.

Masaya, S. and Verschuur, D. J. (2018). Iterative reflectivity-constrained velocity estimation for seismic imaging. *Geophysical Journal International*, 214.

Matsushima, J., Ali, M., and Bouchaala, F. (2015). Seismic attenuation estimation from zero-offset VSP data using seismic interferometry. *Geophysical Journal International*, 204(2):1288–1307.

Müller, K. W., Soroka, W. L., Paulsson, B. N. P., Marmash, S., Baloushi, M. A., and Jeelani, O. A. (2010). 3D VSP technology now a standard high-resolution reservoir-imaging technique: Part 2, interpretation and value. *The Leading Edge*, 29(6):698–704.

Nemeth, T., Wu, C., and Schuster, G. T. (1999). Least-squares migration of incomplete reflection data. *Geophysics*, 64:208–221.

O'Brien, M. J. and Gray, S. H. (1996). Can we image beneath the salt? *The Leading Edge*, 15(1):17–22.

Oristaglio, M. L. (1985). A guide to the current uses of vertical seismic profiles. *Geophysics*, 50(12):2473–2479.

Owusu, J. C., Podgornova, O., Charara, M., Leaney, S., Campbell, A., Ali, S., Borodin, I., Nutt, L., and Menkiti, H. (2016). Anisotropic elastic full-waveform inversion of walkaway vertical seismic profiling data from the arabian gulf. *Geophysical Prospecting*, 64(1):38–53.

Pavlis, G. L. (2003). Imaging the earth with passive seismic arrays. *The Leading Edge*, 22:224–231.

Petersen, K. B. and Pedersen, M. S. (2012). *The matrix cookbook*. Technical Universtiy of Denmark.

Qu, S. and Verschuur, D. J. (2017). Simultaneous joint migration inversion for accurate time-lapse analysis of sparse monitor surveys. EAGE, Eur. Ass. of Geosc. and Eng., Expanded abstracts.

Qu, S. and Verschuur, D. J. (2021). Simultaneous joint migration inversion with calendar-time constraints as a processing tool for semi-continuous surveys. *GEOPHYSICS*, 86:1–90.

Rietveld, W. E. A. and Berkhout, A. J. (1994). Prestack depth migration by means of controlled illumination. *Geophysics*, 59(5):801–809.

Rietveld, W. E. A., Berkhout, A. J., and Wapenaar, C. P. A. (1992). Optimum seismic illumination of hydrocarbon reservoirs. *Geophysics*, 57(10):1334–1345.

Ristow, D. and Ruhl, T. (1994). Fourier finite-difference migration. *Geophysics*, 59:1882–1893.

Robein, E. (2003). *Velocities, Time-imaging, and Depth-imaging in Reflection Seismics: Principles and Methods*. EAGE Publications.

Robein, E. (2010). *Velocities, time-imaging and depth-imaging: Principles and methods*. Earthdoc.

Ruigrok, E., Jagt, L., and van der Vleut, B. (2020). Exploiting wind-turbine noise for seismic imaging and monitoring. EGU, European. Geosciences. Union.

Sava, P. and Fomel, S. (2003). Angle-domain common-image gathers by wavefield continuation methods. *Geophysics*, 68(3):1065–1074.

Sava, P. and Vasconcelos, I. (2011). Extended imaging condition for wave-equation migration. *Geophysical Prospecting*, (59):35–55.

Schneider, W. A. (1978). Integral formulation for migration in two and three dimensions. *Geophysics*, 43(1):49–76.

Shafiq, M. and Apisampinvong, J. (2013). Advanced borehole seismic acquisition challenges and successes in large lng project. *ASEG Extended Abstracts*, 2013(1):1–5.

Slob, E., Wapenaar, K., Broggini, F., and Snieder, R. (2014). Seismic imaging using internal multiples with marchenko-type equations. *Geophysics*, 79(2):S63–S76.

Smidt, J. M., Conn, P., and Lappin, M. (1998). Interpretive processing of a walkaway VSP: Imaging a north sea pre-zechstein reservoir. *Journal of Petroleum Science and Engineering*, 19(3):241–252.

Smith, P., Szydlik, B., and Traylen, T. (2011). True-azimuth 3D srme in the norwegian sea. *The Leading Edge*, 30(8):928–931.

Soni, A. and Verschuur, D. J. (2014). Full-wavefield migration of vertical seismic profiling data: using all multiples to extend the illumination area. *Geoph. Prosp.*, 62(4):740–759.

Staal, X. R. and Verschuur, D. J. (2013). Joint migration inversion, imaging including all multiples with automatic velocity update. pages Tu–02–16, 4pp., London. EAGE, Eur. Ass. of Geosc. and Eng., Expanded abstracts.

Stolt, R. H. (1978). Migration by fourier transform. *Geophysics*, 43(1):23–48.

Stolt, R. H. and Weglein, A. B. (1985). Migration and inversion of seismic data. *Geophysics*, 50:2458–2469.

Sun, D., Jiao, K., Cheng, X., and Vigh, D. (2016). Reflection based waveform inversion. pages 1151–1156, Dallas. SEG, Soc. Expl. Geophys., Expanded abstracts.

Sun, D., Jiao, K., Cheng, X., Xu, Z., Zhang, L., and Vigh, D. (2017). Born modeling based adjustive reflection full waveform inversion. pages 1460–1465. SEG, Soc. Expl. Geophys., Expanded abstracts.

Sun, Y., Kim, Y. S., Shan, S., Verschuur, D. J., Almomin, A., and van Borselen, R. (2018). Joint Migration Inversion Versus FWI-RTM - A Comparison Study on a 2d Realistic Deep Water Model. EAGE, Eur. Ass. of Geosc. and Eng., Expanded abstracts.

Tak, H., Byun, J., Seol, S. J., and Yoo, D. G. (2013). Zero-offset vertical seismic profiling survey and estimation of gas hydrate concentration from borehole data from the ulleung basin, korea. *Marine and Petroleum Geology*, 47:204–213.

Taner, M. T. and Koehler, F. (1969). Velocity spectra - digital computer derivation applications of velocity functions. *Geophysics*, 34(6):859–881.

Tarantola, A. (1984). Inversion of seismic reflection data in the acoustic approximation. *Geophysics*, 44:1259–1266.

Tertyshnikov, K., AlNasser, H., Pevzner, R., Urosevic, M., and Greenwood, A. (2018). 3D VSP for minitoring of the injection of small quantities of CO2-CO2CRC Otway case study. Copenhagen. EAGE, Eur. Ass. of Geosc. and Eng., Expanded abstracts.

Thomsen, L. (1986). Weak elastic anisotropy. *Geophysics*, 51(10):1954–1966.

van Groenestijn, G. J. A. and Verschuur, D. J. (2008). Towards a new approach for primary estimation. pages 2487–2491, Las Vegas. SEG, Soc. Expl. Geophys., Expanded abstracts.

Vermeer, G. J. O. (2012). *3D seismic survey design, 2nd edition*. SEG.

Verschuur, D. J. (1991). *Surface-related multiple elimination: an inversion approach*. PhD thesis, Delft University of Technology.

Verschuur, D. J. and Berkhout, A. J. (2000). Overview of surface and internal multiple removal strategies. pages 1–7, Houston. OTC, Offshore Techn. Conf., Expanded abstracts 12051.

Verschuur, D. J. and Berkhout, A. J. (2011). Seismic migration of blended shot records with surface-related multiple scattering. *Geophysics*, 76(1):A7–A13.

Verschuur, D. J., Berkhout, A. J., and Wapenaar, C. P. A. (1992). Adaptive surface-related multiple elimination. *Geophysics*, 57(9):1166–1177.

Verschuur, D. J. and Hoogerbrugge, L. (2020). A modular wavefield inversion process, including internal multiples, transmission and converted waves. pages 1–4. EAGE, Eur. Ass. of Geosc. and Eng., Expanded abstracts.

Verschuur, D. J., Staal, X. R., and Berkhout, A. J. (2016). Joint migration inversion: Simultaneous determination of velocity fields and depth images using all orders of scattering. *The Leading Edge*, 35:1037–1046.

Virieux, J. (1986). P-sv wave propagation in heterogeneous media: Velocity-stress finitedifference method. *Geophysics*, 51(3):888–901.

Virieux, J. and Operto, S. (2009). An overview of full-waveform inversion in exploration geophysics. *Geophysics*, 74(6):WCC127 – WCC152.

Wapenaar, C. (1996). One-way representation of seismic data. *Geophysical Journal International*, 127(1):178–188.

Wapenaar, K., Thorbecke, J., van der Neut, J., Broggini, F., Slob, E., and Snieder, R. (2014). Marchenko imaging. *Geophysics*, 79(3):WA39–WA45.

Warner, M. and Guasch, L. (2016). Adaptive waveform inversion: Theory. *Geophysics*, 81(6):1ND–Z53.

Wason, W., Wilson, S., Raymer, D., Jaques, P., and Jones, R. (2004). Passive seismic makes sense for 4D reservoir monitoring. *First Break*, 22(10):59–66.

Weglein, A. B., Gasparotto, F. A., Carvalho, P. M., and Stolt, R. H. (1997). An inverse scattering series method for attenuating multiples in seismic reflection data. *Geophysics*, 62:1975–1989.

Whitmore, N. D., Ramos-Martinez, J., Yang, Y., and Valenciano, A. A. (2020). Seismic modeling with vector reflectivity. page 2709–2713. SEG, Soc. Expl. Geophys., Expanded abstracts.

Whitmore, N. D., Valenciano, A. A., and Sollner, W. (2010). Imaging of primaries and multiples using a dual-sensor towed streamer. pages 3187–3192, Denver. SEG, Soc. Expl. Geophys., Expanded abstracts.

Wieschollek, P., Hirsch, M., Schölkopf, B., and Lensch, H. (2017). Learning blind motion deblurring.

Zhang, D. and Schuster, G. T. (2014). Least-squares reverse time migration of multiples. *Geophysics*, 79(1):S11–S21.

Acknowledgements

It has been a real pleasure and great privilege to be part of the Delphi Consortium, therefore, I would like to acknowledge all Delphi members - supervisors and students - for their joint efforts and contributions to the success of our research. Moreover, I would like to acknowledge the Delphi sponsors for their continuous support and constructive feedback and discussions. Special thanks for Saudi Aramco in Dhahran for the successful collaboration on the 3D field BSD example, also many thanks to Total research center Pau and BP research center Houston for the challenging synthetic datasets.

I want to express my sincere gratitude to my promoter and teacher Dr. D.J. Verschuur for all his constant effort, indispensable reviewing and significant contribution in making this work possible. During the course of my PHD program, and even before that for so many years including the period of my master project, we have had a lot of educative and nice discussions, which we will definitely continue and hopefully pushing our research to new and exciting frontiers. Special thanks to Prof. A.J. Berkhout and Prof. A. Gisolf from whom I have gained and learned many theoretical insights. I want to thank my second promoter Prof. E.C. Slob for reviewing the thesis and his constructive feedback on the propositions. I would like to thank Prof. C.P.A. Wapenaar for the nice discussion, reviewing and clarifying some ambiguities in the theoretical part. Also many thanks to Prof. G.T. Schuster for his profound reviewing of the thesis, positive feedback and valuable suggestions. I would like to thank Dr. J. Owusu for his extensive reviewing and his, highly appreciated, participation in the committee. Last but not least, I would like to thank Dr. P.M. Zwartjes and Prof. G. Bertotti for reading my thesis and their valuable participation in the committee.

List of publications

Conference abstracts

- El Marhfoul, B. and D. J. Verschuur, 2019, Potential and Challenges of 3D Joint Migration Inversion of 3D Borehole and Surface Seismic Data. The Hague. EAGE Borehole Geophysics Workshop V, Eur. Ass. of Geosc. and Eng., Expanded abstracts.
- El Marhfoul, B. and D. J. Verschuur, 2017, 3D FReflectivity-guided Joint Migration Inversion of Multi-well Borehole Data. Abu Dhabi. EAGE Borehole Geophysics Workshop IV, Eur. Ass. of Geosc. and Eng., Expanded abstracts.
- El Marhfoul, B. and D. J. Verschuur, 2015, 3D Full Wavefield Imaging of Up and Down-Going VSP Data. pages Tu-N118-10, Madrid. EAGE, Eur. Ass. of Geosc. and Eng., Expanded abstracts.
- El Marhfoul, B. and D. J. Verschuur, 2014, 3D joint full wavefield migration of surface and VSP data. pages 5070-5074, Denver. SEG, Soc. Expl. Geophys., Expanded abstracts.
- El Marhfoul, B. and J. Owusu, 2013, 3D VSP pre-stack depth migration; In: Extended abstracts of the EAGE Borehole Geophysics Workshop II: 3D VSP: Benefits, Challenges and Potential, 21-24 April 2013, St Julian's, Malta, BG10,6p.
- El Marhfoul, B. and A, Dajani, 2011, Fracture mapping by diffraction imaging; In: Extended abstracts of the EAGE Workshop: Naturally & Hydraulically Induced Fractured Reservoirs - From Nanodarcies to Darcies, 10 April 2011, Nafplio.
- El Marhfoul, B., J. Owusu and R. Al Zayer, 2011, VSP Imaging by wavefield extrapolation technique; In: Extended abstracts of the EAGE Borehole Geophysics Workshop I: 3D VSP: Emphasis on 3D VSP, 16-19 January 2011 , Istanbul.

- El Marhfoul, B. and A. Al Momin and D. J. Verschuur, 2009, Practical application of CFP technology to resolve complex near surface problems and to estimate a velocity-depth model. EAGE, Eur. Ass. of Geosc. and Eng., Expanded abstracts.